MNIRSM 2026

1ST MALAYSIA NEAR INFRARED SPECTROSCOPY MEETING

14th & 15th September 2026

School of Physics, Universiti Sains Malaysia, Penang

"Spectroscopy and Photonics Research for Science, Technology, and Innovation"

EXTENDED ABSTRACT BOOK

ORGANIZED BY

SUPPORTED BY

MAIN SPONSOR

PARTNERS

mnirsm.usmphysics.org

MNIRSM 2026

EXTENDED ABSTRACT BOOK

Extended Abstract Proceedings

"Spectroscopy and Photonics Research for Science, Technology, and Innovation"

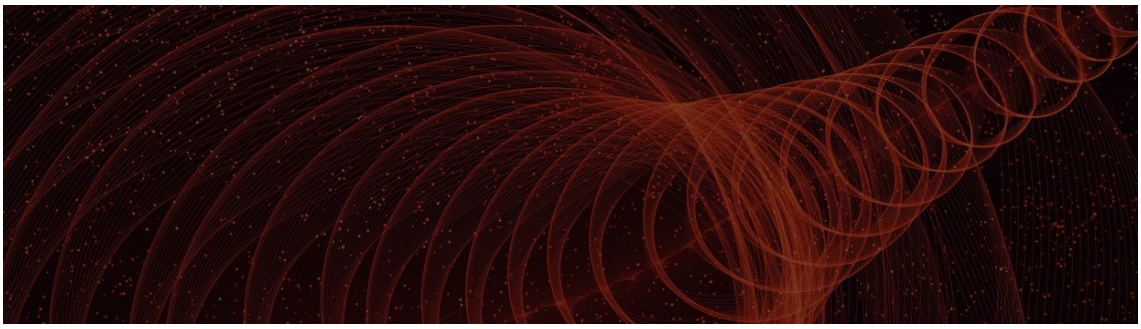

14-15 September 2026

Universiti Sains Malaysia, Penang, Malaysia

Organized by

School of Physics, Universiti Sains Malaysia

Published by
School of Physics, Universiti Sains Malaysia
11800 USM, Pulau Pinang, Malaysia
2026

EDITED BY

Dr. Beh Khi Poay & Dr. Mahayatun Dayana Johan Ooi

PUBLICATION INFORMATION

Copyright and Publication Details

MNIRSM 2026 Extended Abstract Book
Extended Abstract Proceedings (Digital Edition)
1st Malaysia Near-Infrared Spectroscopy Meeting
14-15 September 2026 | Universiti Sains Malaysia, Penang, Malaysia

E-ISBN

To be assigned by Perpustakaan Negara Malaysia.

Published by	School of Physics, Universiti Sains Malaysia
Address	11800 USM, Pulau Pinang, Malaysia
Telephone	+604-653 3200
Email	mnirsm@usm.my
Website	https://mnirsm.usmphysics.org/
Format	Digital edition (e-book), PDF; open-access publication; not available in print

Compiled by the Organizing Committee, MNIRSM 2026, School of Physics, Universiti Sains Malaysia.

Edited by: Dr. Beh Khi Poay and Dr. Mahayatun Dayana Johan Ooi, School of Physics, Universiti Sains Malaysia.

CONTENTS

Extended Abstract Book Contents

FRONT MATTER

Welcome Message from the Conference Chair

ASSOC. PROF. DR. AHMAD FAIRUZ OMAR

Chair, MNIRSM 2026

School of Physics, Universiti Sains Malaysia

Assalamualaikum Warahmatullahi Wabarakatuh and Salam Sejahtera.

On behalf of the Organizing Committee, it is my great pleasure to welcome all participants, presenters, and distinguished guests to the 1st Malaysia Near-Infrared Spectroscopy Meeting (MNIRSM 2026), held on 14-15 September 2026 at Universiti Sains Malaysia (USM), Penang.

As the inaugural edition of this meeting, MNIRSM 2026 marks an important milestone in bringing together the Malaysian near-infrared spectroscopy and photonics research community under a single platform. Organized by the School of Physics, Universiti Sains Malaysia, in collaboration with APEX, this meeting is guided by the theme "Spectroscopy and Photonics Research for Science, Technology, and Innovation." This theme reflects our shared aspiration to advance fundamental and applied research in spectroscopy and photonics, while fostering collaboration between academia, industry, and government agencies.

This program book brings together the schedule of talks, the profiles of our keynote and invited speakers, and the abstracts contributed by our researchers, postgraduate students, and industry partners. I am confident that the exchange of ideas over the course of these two days will spark new collaborations and inspire further innovation within the field.

I would like to express my sincere appreciation to the Organizing Committee for their tireless efforts in bringing this meeting to fruition, to the School of Physics and Universiti Sains Malaysia for their unwavering support, and to our sponsors and exhibitors for their generous contributions. My heartfelt thanks also go to all authors, speakers, and participants - your presence and contributions are what make this meeting possible.

It is my sincere hope that MNIRSM 2026 will serve as the foundation for a recurring and growing meeting in the years to come, and that all participants will leave with new knowledge, new connections, and a renewed enthusiasm for spectroscopy and photonics research.

Thank you, and I wish you all a fruitful and enjoyable MNIRSM 2026.

ASSOC. PROF. DR. AHMAD FAIRUZ OMAR

Message from the Dean / Head of School

ASSOC. PROF. DR. AZHAR ABDUL RAHMAN

Dean, School of Physics
Universiti Sains Malaysia

Assalamualaikum Warahmatullahi Wabarakatuh and Salam Sejahtera.

On behalf of the School of Physics, Universiti Sains Malaysia, it is my great pleasure to welcome all participants, presenters, and distinguished guests to the 1st Malaysia Near-Infrared Spectroscopy Meeting (MNIRSM 2026), held on 14-15 September 2026 here at USM, Penang — the inaugural edition of a meeting that brings the Malaysian near-infrared spectroscopy and photonics research community together for the first time.

Near-infrared spectroscopy sits at the intersection of fundamental physics and practical application, spanning agriculture, food science, pharmaceuticals, environmental monitoring, and materials characterisation. Under the theme "Spectroscopy and Photonics Research for Science, Technology, and Innovation," MNIRSM 2026 reflects the School's broader mission of fostering research that is both scientifically rigorous and socially relevant.

I am confident that the keynote lectures, oral and poster presentations, and informal exchanges over these two days will lay the groundwork for meaningful research collaborations, and I look forward to welcoming an even broader circle of researchers to future editions of this meeting.

My sincere appreciation goes to the Organizing Committee, led by Associate Professor Dr. Ahmad Fairuz Omar, for their dedication in bringing this inaugural meeting to fruition, and to our keynote and invited speakers, partners, sponsors, and exhibitors for their generous support.

It is my sincere hope that MNIRSM 2026 marks the beginning of a long and successful tradition that strengthens the ties between academia, industry, and government agencies in advancing spectroscopy and photonics research in Malaysia and the wider region. Thank you, and I wish everyone a productive, enjoyable, and memorable MNIRSM 2026.

ASSOC. PROF. DR. AZHAR ABDUL RAHMAN

Message from the Chair, Optical Society of Malaysia (OSM)

DR. AHMAD HAZIQ AIMAN BIN ROSOL

President, Optical Society of Malaysia (OSM)

Optical Society of Malaysia

Assalamualaikum warahmatullahi wabarakatuh and warm greetings to all.

On behalf of the Optical Society of Malaysia (OSM), it is my great pleasure to welcome all delegates to the 1st Malaysia Near Infrared Spectroscopy Meeting (MNIRSM 2026).

As a co-organizer of this inaugural event, OSM is honored to partner with the School of Physics, Universiti Sains Malaysia, in establishing Malaysia's first dedicated platform for Near Infrared (NIR) spectroscopy. This meeting brings together researchers, academics, and industry professionals to share the latest advances across NIR and related spectroscopies, including FTIR, Raman, UV-Vis, and fluorescence.

NIR spectroscopy continues to play an increasingly vital role in agriculture, food safety, biomedical diagnostics, environmental monitoring, and photonics. It is our sincere hope that MNIRSM 2026 will spark new ideas, strengthen collaborations, and nurture the growth of a vibrant spectroscopy community in Malaysia and beyond.

We extend our heartfelt appreciation to the School of Physics, USM, and to all our partners and sponsors for their invaluable support in making this meeting possible.

To all participants, we wish you a fruitful and inspiring conference.

Thank you.

DR. AHMAD HAZIQ AIMAN BIN ROSOL

Conference Information

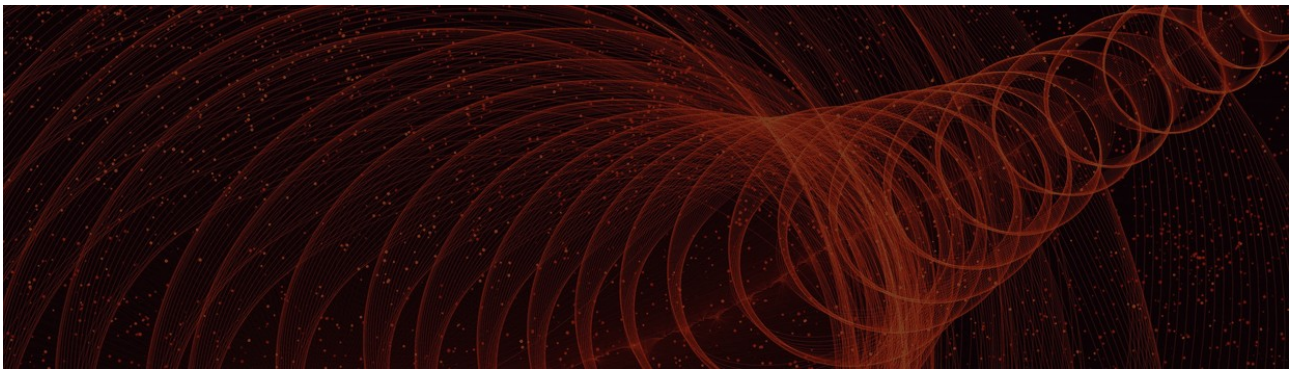

Purpose, theme, organization and venue information for MNIRSM 2026.

About the Conference

The 1st Malaysia Near-Infrared Spectroscopy Meeting (MNIRSM 2026) is an inaugural two-day scientific meeting organized by the School of Physics, Universiti Sains Malaysia. It brings together researchers, postgraduate students, instrument specialists and industry partners working across near-infrared spectroscopy, optical sensing, photonics and related analytical technologies.

Held on 14-15 September 2026 at Universiti Sains Malaysia, Penang, the meeting provides a focused platform for scientific exchange, technical discussion and the development of new collaborations across academia, industry and government agencies.

Conference Theme and Objectives

"Spectroscopy and Photonics Research for Science, Technology, and Innovation"

- Advance fundamental and applied research in spectroscopy and photonics.
- Strengthen collaboration among universities, industry and government agencies.
- Provide researchers and postgraduate students with a platform to present and discuss their work.
- Encourage practical applications of spectroscopy in agriculture, food, environment, health and advanced materials.

Scientific Scope

NIR spectroscopy; hyperspectral imaging; chemometrics and aquaphotomics; UV-visible-NIR, FTIR, Raman and photoluminescence spectroscopy; agricultural, food, environmental, biomedical and health applications; optical sensors and photonic devices; advanced optical materials and photonic technologies.

Organizing Committee

Advisor	Assoc. Prof. Dr. Azhar Abdul Rahman Dean, School of Physics, Universiti Sains Malaysia
Chairman	Assoc. Prof. Dr. Ahmad Fairuz Omar
Deputy Chairman I	Assoc. Prof. Dr. Mohd Mahadi Halim
Deputy Chairman II	Assoc. Prof. Dr. Iskandar Shahrim Mustafa
Secretary I	Dr. Siti Azrah Mohd Samsuri
Secretary II	Assoc. Prof. Dr. Suhana Arshad
Treasurer I	Dr. Siti Khadijah Mohd Bakhori
Treasurer II	Dr. Afiq Arif Aminuddin Jafry
Registration	Dr. Nurhafizah Md Disa Dr. Nur Nabihah Yusof Ms. Nur Awanis Sirat
Publicity	Dr. Edmund Loh Wai Ming Dr. Mohd Fareezuan Abdul Aziz Ms. Nor Izzati Hashim
Program and Abstract Book	Dr. Mahayatun Dayana Johan Ooi Dr. Beh Khi Poay Dr. Subramani Shanmugan
Technical, Multimedia and Certificates	En. Muhammad Syukri Sa'adon Dr. Ahmad Rujhan Mohd Rais Dr. Mohammed Ali Dheyab Dr. Abdul Hadi Sulaiman Dr. Mustaqim Rosli Mr. Mohd Noor Fakarruddin Abdullah Mr. Muhammad Anis Ibnu Hajar
Food and Beverages	Dr. Dian Alwani Zainuri Mrs. Norazlina Abd Malik Mrs. Diana Fariha Saad
Photo Session	Mr. Mustaqim Abu Bakar Mr. Azmi Abdullah Mr. Shahil Ahmad Khosaini

Venue Information and Map

Venue	School of Physics, Universiti Sains Malaysia
Address	11800 USM, Pulau Pinang, Malaysia
Conference dates	14-15 September 2026
Published event hours	09:00-18:00 (GMT+8); detailed timings pending
Conference website	https://mnirsm.usmphysics.org/

Campus Map

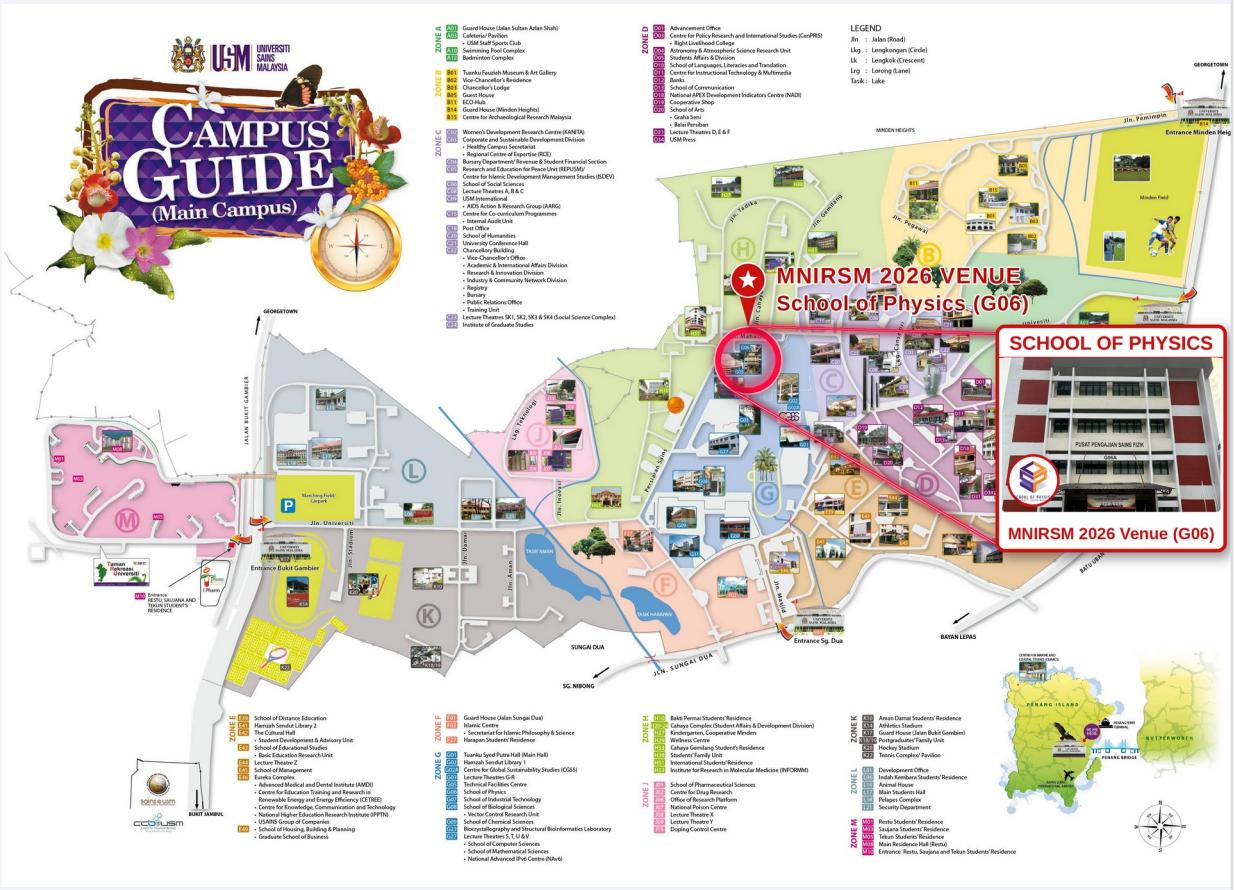

USM Main Campus — School of Physics (G06) marked as the MNIRSM 2026 venue

Speakers

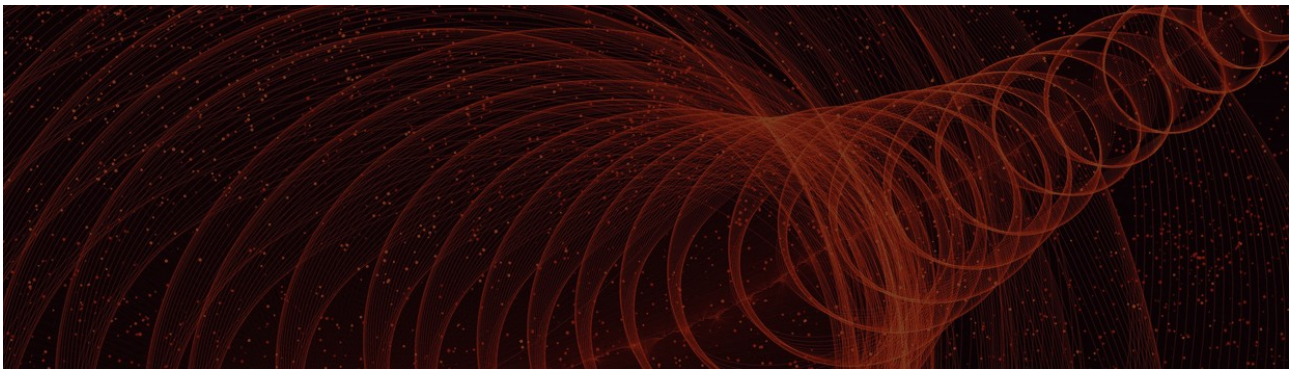

Keynote, plenary and invited speaker profiles presented in a consistent editorial format.

Keynote / Plenary Speaker Profiles

KEYNOTE SPEAKER 01

Prof. Dr. Hoeil Chung

Chairman, Asian NIR Consortium
Hanyang University, Korea

Presentation title	Hyperspectral Near-infrared Spectroscopy for High-throughput Analysis of Diverse Samples
Session	Keynote Speaker I, Day 1
Date and time	14 September 2026, 09:00 - 09:30
Venue	Conference Room

Speaker Profile

SPEAKER BIOGRAPHY

Professor Hoeil Chung is a Professor in the Department of Chemistry at Hanyang University, Seoul, Korea, and current Chairman of the Asian NIR Consortium. He earned his B.S. from Hanyang University in 1989 and his Ph.D. from the University of Iowa in 1994. He then joined SK Energy in Korea as a research scientist, working on the development of diverse NIR spectroscopic on-line monitoring systems. In 2002 he joined Hanyang University, where his academic research has focused on transmission and wide-area-coverage Raman spectroscopy for non-destructive analysis, reproducible and reusable SERS schemes for detecting disease biomarkers, electrochemical synthesis of metal-alloy nanostructures, and the development of advanced chemometric algorithms.

Prof. Dr. Roger Meder

Meder Consulting
Bracken Ridge, Queensland, Australia

Presentation title	Application of near infrared spectroscopy in industrial tree plantations and wood products development in Sabah, Malaysia
Session	Keynote Speaker II, Day 1
Date and time	14 September 2026, 09:40 - 10:10
Venue	Conference Room

Speaker Profile

SPEAKER BIOGRAPHY

Professor Roger Meder is Principal at Meder Consulting, where he leads analytical laboratory services for Ridley AgriProducts, Australia's leading animal feed supplier. He holds a BSc and MSc in chemistry from Otago University and a PhD in physics from Massey University. He has worked in NIR spectroscopy and chemometrics for over 30 years. He was formerly Group Leader of the Forest Genetics, Genomics and Phenomics group at Australia's CSIRO, and holds Adjunct Professor appointments at the University of the Sunshine Coast and Universiti Putra Malaysia. He is Editor-in-Chief of the Journal of Near Infrared Spectroscopy and Chair of the Australian NIR Spectroscopy Group, and received the 2023 Tomas Hirschfeld Award from ICNIRS. His current focus is expanding a distributed NIR network across Ridley's 20 manufacturing and processing plants.

Dr. Akifumi Ikehata

Chairman, Japan Council of Near Infrared Spectroscopy
National Agriculture and Food Research Organization, Japan

Presentation title	Connecting NIR Communities: The Near Infrared Forum (NIRF) and Research Activities in Japan
Session	Keynote Speaker III, Day 1
Date and time	14 September 2026, 10:10 - 10:50
Venue	Conference Room

Speaker Profile

SPEAKER BIOGRAPHY

Dr. Akifumi Ikehata is Manager of the Division of Food Quality Assessment and Control Research at Japan's National Agriculture and Food Research Organization (NARO). He earned his Ph.D. in physicochemical research on polymer gels from Tokyo University of Agriculture and Technology in 2001. He has worked in near-infrared (NIR) spectroscopy since 2002, under the mentorship of Professor Yukihiro Ozaki. Since 2008 he has led research on the nondestructive analysis of foods using near-infrared spectroscopy at NARO. In 2024 he became President of the Japan Council for Near Infrared Spectroscopy (JCNIRS). His current research explores far-ultraviolet spectroscopy and the integration of nondestructive spectroscopic techniques with metabolomics for food quality assessment and control.

Extended Abstract Proceedings

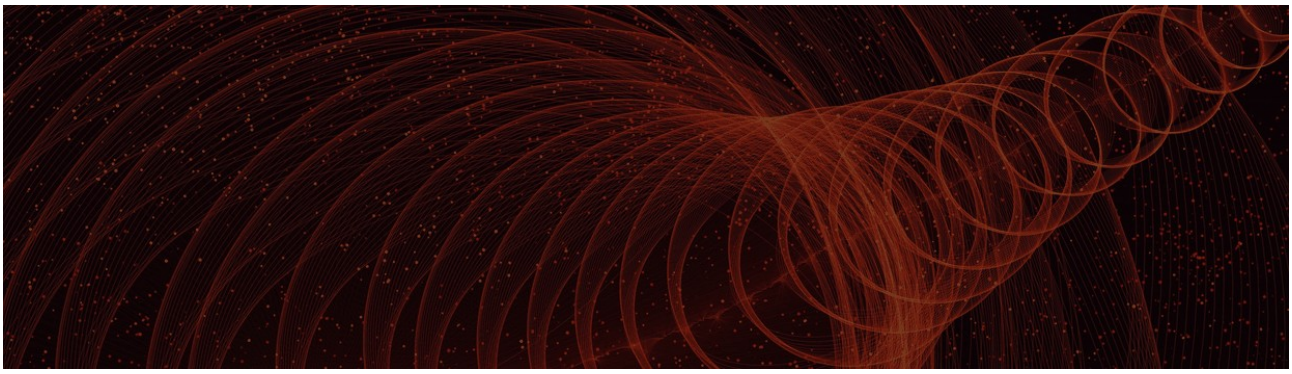

Complete extended abstracts submitted by presenters, formatted in a consistent editorial structure for the proceedings.

Visible and Near Infrared Spectroscopy in Sustaining Quality of Life

Ahmad Fairuz Omar

School of Physics, Universiti Sains Malaysia, 11800 USM, Penang, Malaysia

***Corresponding author:** fairuz_omar@usm.my

Abstract

Metrology is an essential branch of science that provides a reliable and traceable basis for measurement by identifying key variables in samples of interest, measurement devices, and units for standardization, among others. Reliable measurement provides a scientific basis for assessing quality, safety, and changes in systems that directly or indirectly affect quality of life. Optical spectroscopy has continuously emerged as an alternative measurement technology for various applications. The interaction between electromagnetic radiation within ultraviolet, visible, and near-infrared wavelengths with matter may provide characteristic spectral signatures related to the properties and conditions of the measured sample. Visible and near-infrared spectroscopy has continued to gain popularity in sustainable analytical science because it can perform measurements rapidly and non-destructively, requires little to no sample preparation, and uses few or no chemical reagents. The availability of simple and portable spectrometers further enables measurements to be performed closer to the point of interest. Our research explores the potential of visible and near-infrared spectroscopy for observing and monitoring changes in different sample systems associated with quality of life. A series of studies involving food, biological cell systems, and plants has demonstrated how changes in spectral responses can be related to food authenticity, cellular activity, and plant health. These include the detection and quantification of adulteration in stingless bee honey, monitoring spectral changes associated with cancer and normal cell growth, and identifying progressive water stress in oil palm seedlings. The results demonstrate that changes in the interaction between light and matter can provide meaningful spectral signatures of changing sample conditions, with promising accuracy for both quantitative assessment and classification. In this presentation, we will share our ongoing efforts in using visible and near-infrared spectroscopy to monitor changes in diverse systems and discuss its potential as a rapid, non-destructive, and sustainable measurement approach for applications related to food, agriculture, health, and quality of life.

Keywords: *Metrology, Visible and Near-Infrared Spectroscopy, Sustainability*

Introduction

Reliable measurement is fundamental to quality of life, particularly in food, agriculture and health. However, conventional analytical methods often require sample preparation, chemical reagents, laboratory facilities and considerable analysis time. Visible and near-infrared (Vis–NIR) spectroscopy offers a rapid and non-destructive alternative, as the interaction of light with matter produces spectral responses related to the physical and chemical characteristics of a sample. With minimal sample preparation and the increasing availability of portable instruments, Vis–NIR spectroscopy has considerable potential for real-time and field-based measurements.

Our research focuses on using Vis–NIR spectroscopy not only to measure sample properties, but also to monitor changes occurring under different conditions. A range of studies involving food, biological systems and plants was conducted to explore how spectral changes can provide information related to quality, biological activity and plant health.

Methodology

Our approach was to observe how the interaction between light and a sample changes as its condition changes. Controlled experiments were designed using food, biological and plant systems, in which selected conditions were progressively altered while their spectral responses were monitored. In food, stingless bee honey was examined with increasing levels of adulteration to determine whether changes in its spectral characteristics could reveal and quantify loss of authenticity [1]. In biological systems, changes associated with the growth of cancerous and normal cells were followed through the spectral response of their surrounding culture medium, including experiments involving different cell populations [2-3]. In plants, oil palm seedlings were exposed to increasing periods of water limitation, allowing changes in leaf spectra to be followed as plant water status changed [4]. In another experiment, Harumanis mangoes were analysed by Vis–NIR spectroscopy (500–1050 nm) using chemometric pre-processing, wavelength selection, PCA, data augmentation, and tuned machine-learning regressors, with front-side calibration and independent back-side validation across two dates for SSC and pH prediction [5].

Across these studies, the measured spectra were compared with the corresponding physical, chemical or biological conditions to identify spectral signatures and establish their relationships with sample quality or condition. The emphasis was therefore not only on predicting a particular parameter, but on understanding how spectral changes evolve with changes in the sample itself.

Results and Discussion

The studies demonstrated that Vis–NIR spectroscopy was sensitive to changes in diverse sample systems. In stingless bee honey, the 400–1100 nm spectral region successfully differentiated adulterated samples and enabled the adulteration level to be quantified, with the best model achieving $R^2 = 0.96$ and RMSECV = 5.88%. Changes associated with adulteration were also related to the water-related spectral characteristics of the honey [1].

In the biological studies, changes in the culture medium during cell growth produced distinctive spectral profiles for HeLa and DU145 cancer cells compared with normal L929 fibroblasts. When different cell concentrations were investigated, Vis–NIR spectroscopy achieved prediction accuracies of $R^2 \geq 0.93$, demonstrating its potential for monitoring cellular activity through changes in the surrounding medium [2-3].

For oil palm seedlings, progressive water stress produced measurable changes in leaf reflectance, particularly in the 900–1000 nm region associated with water-related characteristics. Different levels of water stress could be classified with average accuracies of approximately 92–94%, demonstrating the potential for non-destructive monitoring of plant water status [4]. In another application in agriculture, Vis–NIR reflectance spectroscopy combined with machine-learning pipelines was evaluated for non-destructive assessment of soluble solids content (SSC) and pH in Harumanis mangoes. The models demonstrated reliable performance across independent validation sets (R^2 of 0.67–0.71 for SSC and 0.63–0.81 for pH) [5].

Together, these studies reveal a common principle: changes in the condition of a sample are reflected in its interaction with light. This principle enables spectroscopy to be applied across very different systems, from food authenticity and biological activity to plant health.

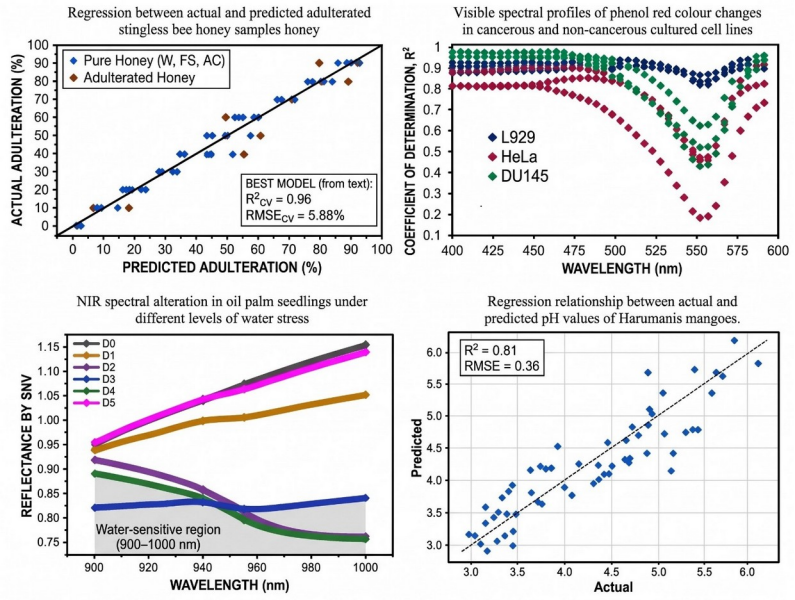

Figure 1. Overview of Visible and Near-Infrared (Vis-NIR) spectroscopy applications in multidisciplinary research at the School of Physics. The panels highlight the versatility of Vis-NIR spectroscopy across diverse research fields, including the prediction of adulteration levels in stingless bee honey (top left [1]), differentiation of cancerous (HeLa and DU145) and non-cancerous (L929) cell lines based on visible spectral profiles (top right [2]), classification of water-stress levels in oil palm seedlings using NIR reflectance spectra (bottom left [4]), and prediction of pH values in Harumanis mangoes (bottom right [5]).

Conclusion

Our research demonstrates the versatility of Vis–NIR spectroscopy as a non-destructive measurement approach for monitoring diverse systems associated with quality of life. Across food, biological and plant applications, spectral measurements were able to reveal changes related to authenticity, biological activity and plant water status, with promising results for both qualitative discrimination and quantitative assessment. More importantly, the studies illustrate the potential of spectroscopy to move beyond conventional point measurements towards dynamic monitoring of changes in samples and living systems.

The combination of rapid optical measurement, minimal sample preparation and reduced dependence on chemical reagents makes Vis–NIR spectroscopy attractive for more sustainable analytical practices. With continuing developments in portable instrumentation, data analysis and intelligent sensing, spectroscopy has the potential to support real-time monitoring in food quality, agriculture and health-related applications. Ultimately, the transition from measuring samples to understanding and monitoring change through light may provide a valuable pathway towards faster, more sustainable and accessible measurement technologies that contribute to quality of life.

References

[1] Raypah, M. E., Omar, A. F., Muncan, J., Zulkurnain, M., & Abdul Najib, A. R. (2022). Identification of stingless bee honey adulteration using visible-near infrared spectroscopy combined with aquaphotomics. Molecules, 27(7), 2324.

[2] Amran, E. N., Sudik, S., Omar, A. F., Mail, M. H., & Seeni, A. (2019). Potential colorimetric detection of cancer cells using Phenol Red. Photodiagnosis and photodynamic therapy, 27, 380-384.

[3] Raypah, M. E., Muncan, J., Sudik, S., Omar, A. F., Mail, M. H., Tsenkova, R., & Seeni, A. (2022). Implication of phenol red in quantification of cultured cancerous cells using near-infrared spectroscopy and aquaphotomics. Chemometrics and Intelligent Laboratory Systems, 230, 104669.

[4] Raypah, M. E., Nasru, M. I. M., Nazim, M. H. H., Omar, A. F., Zahir, S. A. D. M., Jamlos, M. F., & Muncan, J. (2023). Spectral response to early detection of stressed oil palm seedlings using near-infrared reflectance spectra at region 900-1000 nm. Infrared Physics & Technology, 135, 104984.

[5] Irshad, A., Muncan, J., & Omar, A. F. (2026). Principal component analysis (PCA)-integrated machine learning (ML) pipelines for spectral modelling of Harum Manis mangoes. European Food Research and Technology, 252(6), 224.

Application of near infrared spectroscopy in industrial tree plantations and wood products development in Sabah, Malaysia

Roger Meder[1,2,3*]

[1]Meder Consulting, Bracken Ridge, Queensland Australia

[2]Borneo Forestry Co-Operative, Kota Kinabalu, Sabah, Malaysia

[3]Forest Research Institute, University of the Sunshine Coast, Sippy Downs, Queensland, Australia

***Corresponding author:** roger@mederconsulting.com

Abstract

Near infrared spectroscopy has been calibrated to predict a number of properties of interest to tree breeders and tree plantation operators. Aspects of solid wood characterisation, soil characterisation and tree foliage assessment have been assessed in industrial tree plantations in Sabah, Malaysia.

Keywords: *Tree breeding, phenotyping, soil carbon, foliar nutrition*

Introduction

Industrial tree plantations are being developed across the Malaysian landscape, particularly the states of Sabah and Sarawak in Borneo, to provide sustainably managed wood supply for expanding pulp and paper, solid timber, engineered wood products and bioenergy industries [1-3].

To be economically and productively sustainable, these plantation developments are ideally 50,000 ha or more in area. Domestic species, while having desirable properties are not suited to such intensive management nor for short rotation cropping (generally in the range 7-20 years). For that reason, exotic species such as Eucalyptus or Acacia are deployed, with Eucalyptus pellita being particularly suited to the Borneo environment. However, the challenge is to characterise the wood properties of the resource, a task requiring measurement of a number of solid wood and fibre properties such as: density, stiffness, and Kraft pulp yield, across a large number of individual tree samples across age and geographic distribution. In addition, the planting environment should be characterised for soil properties.

This presentation will address wood property characterisation, soil characterisation and foliar characterisation of nitrogen and phosphorus as it pertains to fertiliser treatment. In doing so, key aspects of sampling, sample representation, sample preparation, and sample presentation to the instrument will be discussed.

Methodology

NIR Spectroscopy

Near infrared spectra were acquired using one of two separate systems, either a laboratory MPA FT-NIR (Bruker Optics, Ettlingen, Germany) or a handheld microNIR 1900 (Viavi Solutions, Milpitas, CA, USA).

Scenario 1. Wood Characterisation.

Initial destructive sampling was performed by felling individual trees within several designed tree breeding trials across Sabah. Fallen stems were sectioned to produce discs at heights within the stem and diametric strips taken from the discs. Thereby subsamples from different heights and different locations from pith to bark were obtained (Figure 1). Density was determined gravimetrically, while modulus of stiffness (MOE aka stiffness) and modulus of rupture (MOR, aka strength) were determined using 20 mm x 20 mm x 330 mm test specimens, by 3-point bending on a GoTech UTM (Taichung City, Taiwan) with a 300 mm span and loading rate of 5 mm min^{-1}.

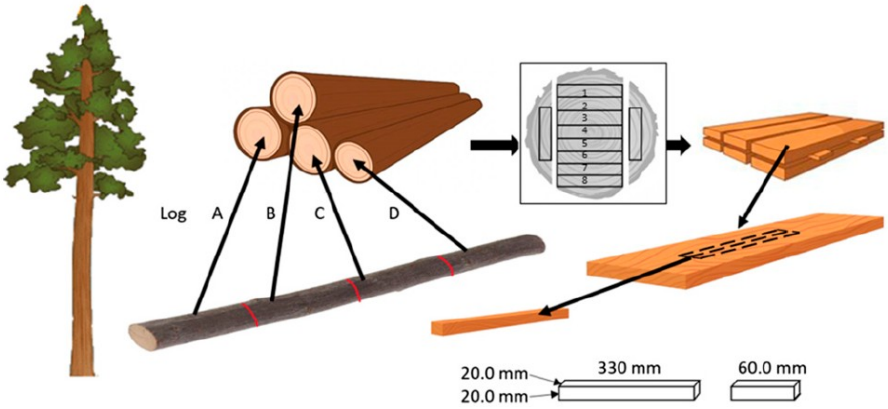

Figure 1. Schematic of sampling location for test specimens.

Scenario 2. Foliar Characterisation

A temporal study of fertiliser application (control + three levels of NPK application [50, 100, 150 g/tree]) was studied by measuring the N and P levels in foliage at periods post planting. The NIR was calibrated using spectra obtained at three time points and the calibration used to predict N and P at the subsequent time points.

Scenario 3. Soil Characterisation

Soil pits were dug at two locations of a trial site where differences in growth productivity were observed. Two horizons 0-10 cm and 20-50 cm were collected, dried and ground prior to NIR spectra being acquired. Reference testing for Bray-P and total nitrogen was performed according to standard methods.

Results and Discussion

The NIR spectra acquired on the MPA and microNIR cover two different ranges as shown in Figure 2 using spectra obtained from dried, ground wood.

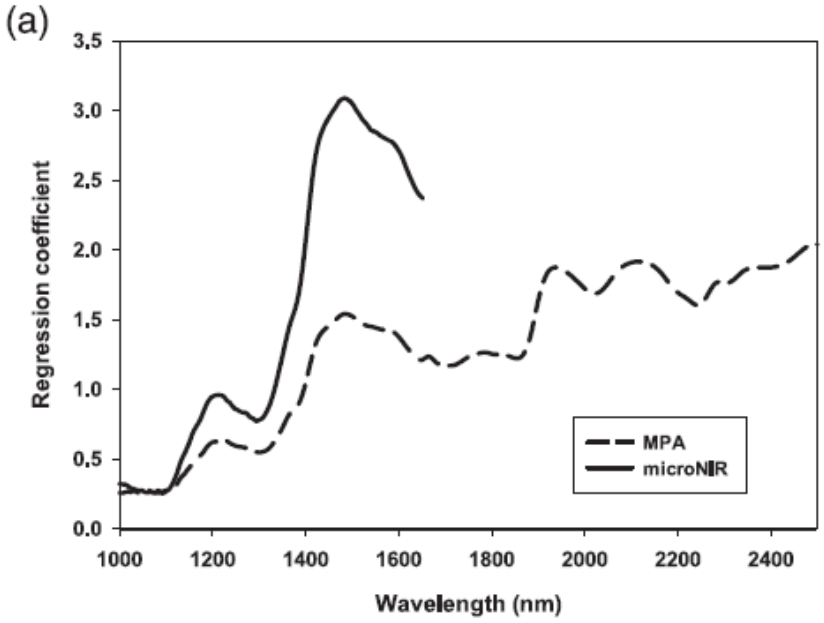

Figure 2. NIR spectra obtained on dried, ground E. pellita wood using a Viavi microNIR and Bruker MPA.

Table 1 presents the calibration, cross validation and test set statistics of PLS regression of NIR and both MOE and MOR for E. pellita grown in Sabah [4].

	LV	$R^2_{Cal.}$	RMSEC	r^2_{CV}	RMSECV	$r^2_{Pred.}$	RMSEP
MOE			GPa		GPa		GPa
microNIR – raw	7	0.75	1.4	0.71	1.6	0.32	2.6
microNIR – 2SG9	3	0.76	1.4	0.80	1.4	0.46	2.3
MPA – raw	9	0.95	0.7	0.85	1.2	0.51	2.0
MPA – 2SG15	4	0.98	0.5	0.70	1.5	0.70	1.5
MOR			MPa		MPa		MPa
microNIR – raw	5	0.81	9.6	0.77	10.6	0.46	22.8
microNIR – 2SG9	4	0.85	8.4	0.80	10.5	0.22	23.4
MPA – raw	9	0.92	7.3	0.62	14.0	0.74	11.2
MPA – 2SG15	4	0.97	4.4	0.62	13.9	0.63	13.9

2SG9 – Savitzky-Golay, second derivative, 9-point window.
2SG15 – Savitzky-Golay, second derivative, 15-point window.

Table 1. Calibration and test set prediction statistics for NIR prediction of MOE and MOR using the Viavi microNIR and Bruker MPA spectrometers (Ncal = 51, Nval =40)

Figure 2 shows the measured foliar N and P for the first three timepoints and the data used for calibration. The fourth and fifth timepoints are NIR predicted N and P values [5].

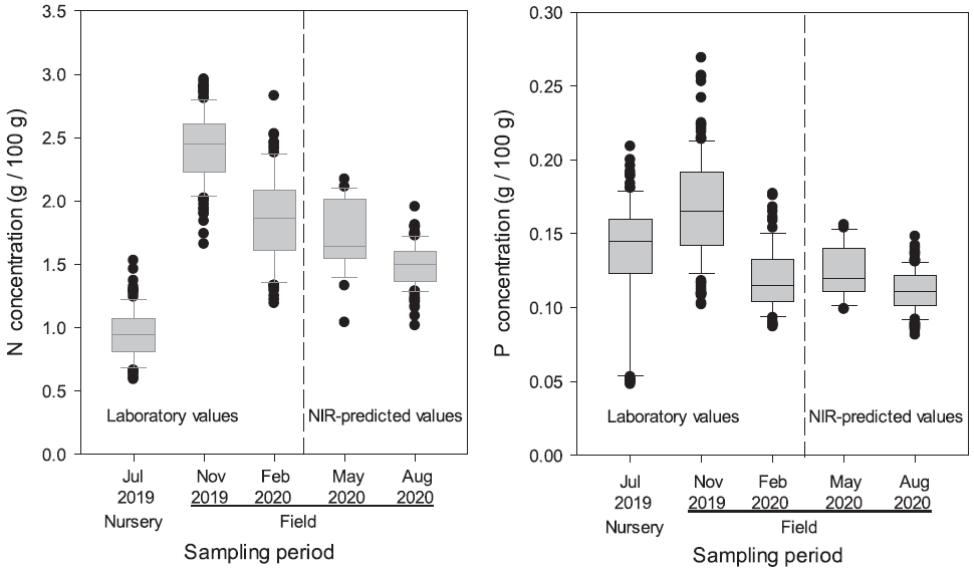

Figure 2. Box-whisker plots showing the distribution of N and P in foliage from E. pellita leaves in a NPK fertiliser trial.

Figure 3 shows the NIR-predicted values for Total N, total organic C and soil pH at two depth horizons at spatially separated locations within a tree breeding trial. On particular note is the spatial variation in total nitrogen in the A-horizon [6].

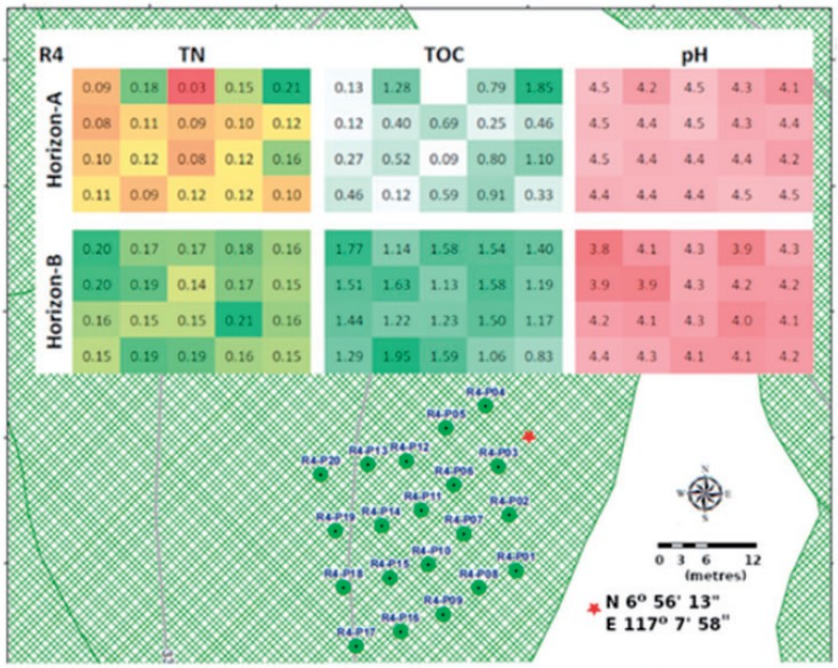

Figure 3. NIR-predicted total N, TOC and pH for the A- and B-horizons of soil pits spaced on a 5 x 5 m grid within a E. pellita breeding trial.

Additional results will be presented in the conference presentation.

Conclusion

Near infrared spectroscopy can aid several aspects of industrial tree plantation management and resource characterisation once suitably calibrated. Differences in in-field and in-laboratory acquisition of spectra can be particularly influencing on the reliability of prediction. However, this limitation may be considered minimal when temporal studies are considered.

Acknowledgement

The assistance of a number of colleagues from the Borneo Forestry Co-operative is acknowledged, particularly access to valuable breeding trials. I want to thank: Datuk Hattah Jafar, Dr Yani Japarudin, Mahadir Lapammu, Agustan Alwi, and Hamzad Jani.

References

[1] Japarudin Y, Lapammu M, Alwi A, Brown M, Meder R (2022) Non-destructive evaluation of strength and stiffness of plantation-grown Eucalyptus pellita, using acoustic velocity and near infrared spectroscopy. Journal of Near Infrared Spectroscopy, 30(5), 270-278.

[2] Nazir MNMM, Terhem R, Norhisam AR, Razali SM, Meder R (2021) Early monitoring of Eucalyptus pellita health status via hyperspectral imaging of canopy foliage using unmanned arial vehicle. Forests, (12), 1393-1412.

[3] Lu W, Arnold R, Wang C, Lin Y, Luo J, Meder R, Yang Y (2021) Defining Eucalyptus urophylla with its hybrid and the rules of genetic recombination using near infrared spectroscopy. Journal of Near Infrared Spectroscopy, 29(4), 236-244.

[4] Japarudin Y, Lapammu M, Alwi A, Brown M, Meder R (2022) Non-destructive evaluation of strength and stiffness of plantation-grown Eucalyptus pellita, using acoustic velocity and near infrared spectroscopy. Journal of Near Infrared Spectroscopy, 30(5), 270-278.

[5] Alwi A, Meder R, Japarudin Y, Hamid HA, Adibah R, Hafiz K (2021) Near infrared spectroscopy of Eucalyptus pellita foliage nutrients and the potential for real-time monitoring of trees in fertiliser trials. Journal of Near Infrared Spectroscopy, 29(3), 158-167.

[6] Abdul Jani HF, Meder R, Hamid HA, Razali SM, Yusoff KHM (2021) Near infrared spectroscopy of plantation forest soil nutrients in Sabah, Malaysia, and the potential for micro-site assessment. Journal of Near Infrared Spectroscopy, 29(3), 148-157.

Connecting NIR Communities: The Near Infrared Forum (NIRF) and Research Activities in Japan

Akifumi Ikehata[1*]
[1]National Agriculture and Food Research Organization (NARO), Japan
***Corresponding author:** ikehata.akifumi270@naro.go.jp

Abstract

This presentation introduces the NIR Forum, an annual symposium on near-infrared (NIR) spectroscopy held in Japan. Over its more than 40-year history, the NIR Forum has provided a platform for active discussion among researchers from a wide range of scientific and industrial fields. It is recognized not only within Japan but also internationally as an important venue where significant advances in NIR spectroscopy and its applications are presented and discussed. The presentation will review the history of the NIR Forum and the development of NIR spectroscopy research in Japan, highlight current research activities and achievements, and discuss future opportunities for international collaboration and cooperation within the global NIR community.

Keywords: *JCNIRS, NIR Forum*

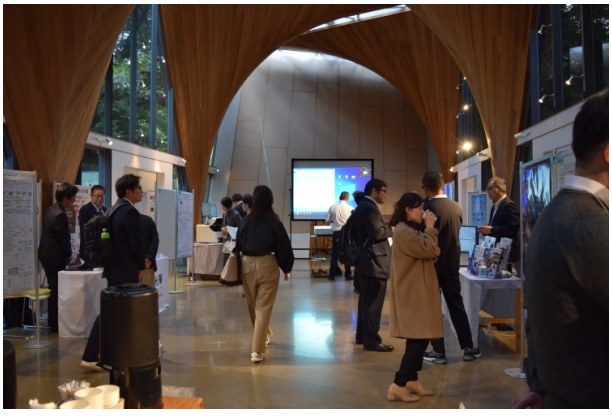

Figure 1. Highlights from the 40th Anniversary NIR Forum in 2024 at the University of Tokyo

The Near Infrared Forum (NIRF) is an annual research meeting on near-infrared (NIR) spectroscopy, typically held around November, and is one of the most important events organized by the Japan Council for Near Infrared Spectroscopy (JCNIRS) [1]. Prior to 2004, this meeting was held under the name "Symposium on Non-Destructive Measurement," but it was renamed NIRF in conjunction with the establishment of JCNIRS. The 40th anniversary meeting was held in 2024, and the

42nd NIRF is scheduled to be jointly organized with the Asian NIR Consortium (ANC) in November 2026.

NIRF attracts more than 200 participants each year from a wide range of disciplines, including natural science, engineering, environmental science, medicine, pharmacy, and agriculture, providing a platform for active and interdisciplinary discussions. The oral presentation program consists of short courses (basics), keynote lectures, the JCNIRS Award ceremony and award lectures, the NIR Advance Award ceremony and lectures, invited and contributed talks in each session, and short presentations by sponsor. In parallel, there are poster presentations and instrument exhibitions by more than 20 companies related to NIR technologies.

While NIR spectroscopy is widely applied in agriculture and food science, one of the distinguishing characteristics of the Japanese research community is its broad distribution across diverse application fields. For example, recipients of the NIR Advance Award - positioned as an encouragement prize- include researchers engaged in instrumentation development, such as pharmaceutical devices, clinical application instruments, process monitoring systems, and LED light sources. In addition, conventional applications in agriculture and food science are evolving beyond simple PLS regression; new approaches are increasingly proposed, including quantification based on light-scattering properties and advanced data analysis through integration with metabolomics.

In this presentation, several examples of recent research activities in NIR spectroscopy in Japan will be introduced, based on presentations from the NIRF.

References

[1] Akifumi Ikehata, "The 38th NIR Forum (Japan)", NIR news, 34 (1-2), 2023/02/20, https://doi.org/10.1177/0960336023115707

Application of Near-Infrared Spectroscopy for Soluble Solids Content Prediction and Classification of Gamma-Irradiated Sugarcane Stalks

Imran Arra'd Sofianto[1*], Siti Noorrohmah[1], Rudiyanto[1]

[1]Research Center for Applied Botani, National Research and Innovation Agency (BRIN), Bogor, Indonesia

***Corresponding author:** imra003@brin.go.id

Abstract

This study aimed to investigate the potential of near-infrared (NIR) spectroscopy for the quantitative prediction and qualitative classification of gamma-irradiated sugarcane stalks. A total of 300 NIR spectra were acquired from the transverse and rind surfaces of cylindrical gamma-irradiated sugarcane stalk samples over the wavelength range of 350–2500 nm. The spectral region of 1000–2400 nm region was selected for subsequent analysis. Spectral pre-processing techniques, including standard normal variate (SNV), multiplicative scatter correction (MSC), first derivative (1st der., 25 smoothing points), and second derivative (2nd der., 25 smoothing points), were applied prior to model development. Partial least squares regression (PLSR) was employed to predict soluble solids content (°Brix), while partial least squares discriminant analysis (PLS-DA) was used to classify the gamma irradiation treatments.

Keywords: *Chemometrics, Quantitative, Qualitative, Transverse, Rind*

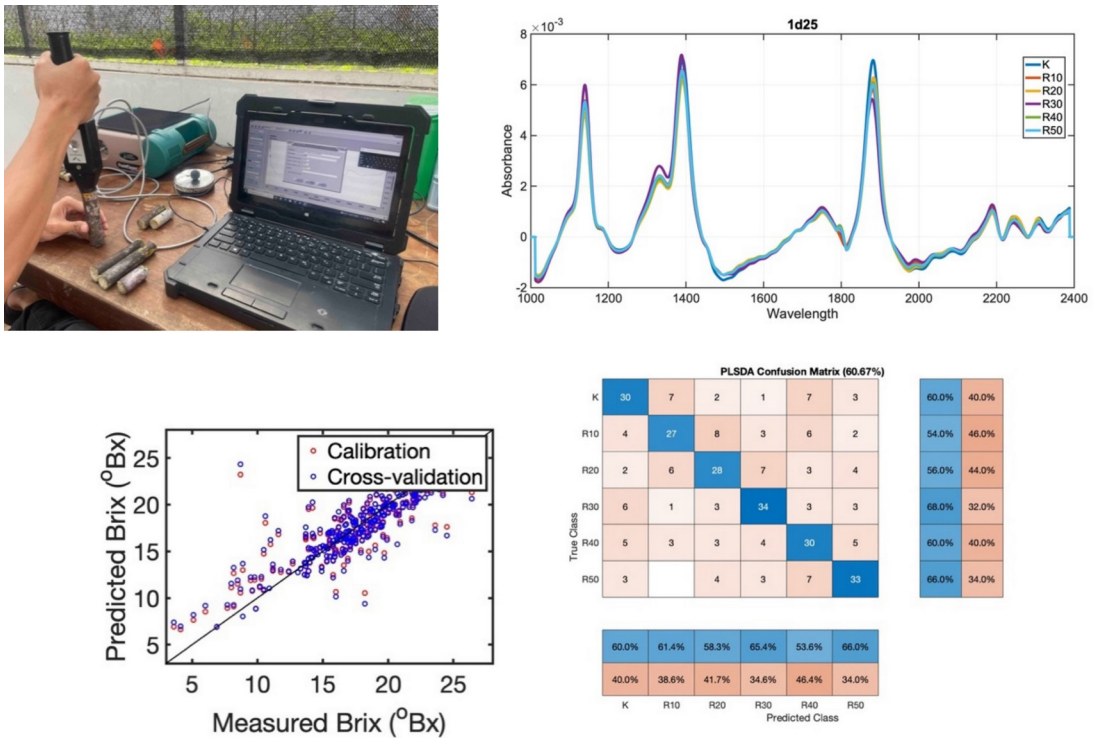

Figure 1. NIR spectral acquisition setup, representative first-derivative absorbance spectra (1000-2400 nm), PLSR-predicted versus measured soluble solids content (°Brix), and PLS-DA confusion matrix for the gamma-irradiation classes.

1. Introduction

Sugarcane (Saccharum officinarum L.) is one of the world's most important crops for sugar production. To meet the growing global demand for sugar, the development of superior sugarcane varieties with higher productivity and enhanced soluble solids content has become a major objective of breeding programs [1–6]. Gamma irradiation has been widely employed as an effective mutation

breeding technique to induce genetic variation and accelerate the development of improved sugarcane cultivars [7–10]. However, evaluating large populations of gamma-irradiated sugarcane using conventional laboratory methods is labor-intensive, time-consuming, and destructive, making it unsuitable for high-throughput screening in breeding programs. Near-infrared (NIR) spectroscopy has emerged as a rapid, non-destructive, and environmentally friendly analytical technique for assessing the chemical composition of agricultural products [11]. Coupled with chemometric methods, NIR spectroscopy enables the simultaneous prediction of quantitative traits and classification of samples based on their spectral characteristics. Nevertheless, studies investigating the application of NIR spectroscopy for both the prediction of soluble solids content (°Brix) and the classification of gamma-irradiated sugarcane stalks remain limited. Therefore, this study aimed to evaluate the potential of NIR spectroscopy combined with partial least squares regression (PLSR) and partial least squares discriminant analysis (PLS-DA) for the rapid prediction of soluble solids content and classification of gamma-irradiated sugarcane stalks.

2. Methodology

Three hundred cylindrical samples of gamma-irradiated sugarcane stalks were used in this study. The sugarcane plants were approximately one year old and comprised six irradiation treatments: Control, 10 Gy, 20 Gy, 30 Gy, 40 Gy, and 50 Gy, with 50 samples per treatment. NIR spectra were acquired immediately after harvesting using an ASD FieldSpec 4 Hi-Res NG Spectroradiometer (Malvern Panalytical, Boulder, CO, USA) from the transverse and rind surfaces of the sugarcane stalk samples. Spectra were acquired over the wavelength range of 350–2500 nm at 1 nm intervals, resulting in a total of 600 spectra (300 transverse and 300 rind spectra). Soluble solids content (°Brix) was measured immediately after spectral acquisition using a PAL-α digital refractometer (ATAGO Co., Ltd., Tokyo, Japan) while the samples remain fresh. Partial least squares regression (PLSR) was employed to predict soluble solids content, whereas partial least squares discriminant analysis (PLS-DA) was used to classify the gamma irradiation treatments. Model performance was evaluated using the coefficient of determination for cross-validation (R^2_{CV}), the root mean square error of cross-validation (RMSECV), and classification accuracy. All statistical analyses were performed using MATLAB R2023b (MathWorks, Natick, MA, USA).

3. Results and Discussion

The soluble solids content of the samples ranged from 3.6 to 27.2 °Brix, with a mean value of 17.65 °Brix, and exhibited an approximately normal distribution. The best quantitative prediction model was obtained using first-derivative spectra with 25 smoothing points for both measurement surfaces. For the transverse surface, the model achieved an R^2_{CV} of 0.6974 with an RMSECV of 2.2180 °Brix, whereas the rind surface yielded an R^2_{CV} of 0.5952 with an RMSECV of 2.5609 °Brix. For qualitative classification, the optimal PLS-DA model for the transverse surface was developed using 1st der. with 25 smoothing points, achieving a classification accuracy of 60.67% with 18 latent variables (LVs). In contrast, the best model for the rind surface was obtained using 2nd der. with 25 smoothing points, resulting in a classification accuracy of 57.00% with 18 LVs. The relatively high number of LV suggests that gamma irradiation induced subtle spectral variations distributed across multiple correlated wavelengths, while the inherent biological variability among sugarcane samples further increased spectral complexity.

4. Conclusion

This study demonstrated the feasibility of using near-infrared (NIR) spectroscopy for the rapid and non-destructive evaluation of gamma-irradiated sugarcane stalks. The developed PLSR models achieved satisfactory prediction performance, with R^2_{CV} values of 0.6974 and 0.5952 and RMSECV values of 2.2180 and 2.5609 °Brix for the transverse and rind surfaces, respectively. Meanwhile, the optimal PLS-DA models achieved classification accuracies of 60.67% and 57.00% for the transverse and rind surfaces, respectively. Although the classification performance was moderate, the results highlight the potential of NIR spectroscopy as a rapid and practical tool for screening gamma-irradiated sugarcane. This approach could support high-throughput mutation breeding programs by enabling

simultaneous prediction of soluble solids content (°Brix) and classification of gamma irradiation treatments.

References

[1] Cursi, D.E., Hoffmann, H.P., Barbosa, G.V.S. et al., "History and Current Status of Sugarcane Breeding, Germplasm Development and Molecular Genetics in Brazil," Sugar Tech, 24 112–133, 2022. https://doi.org/10.1007/s12355-021-00951-1

[2] Dumont, T., Barau, L., Thong-Chane, A. et al., "Sugarcane Breeding in Reunion: Challenges, Achievements and Future Prospects," Sugar Tech, 24 181–192 (2022). https://doi.org/10.1007/s12355-021-00998-0

[3] Widyasari, W.B., Putra, L.K., Ranomahera, M.R.R. et al., "Historical Notes, Germplasm Development, and Molecular Approaches to Support Sugarcane Breeding Program in Indonesia", Sugar Tech, 24 30–47 (2022). https://doi.org/10.1007/s12355-021-01069-0

[4] Windiyani, I. P., Mahfut, Purnomo, & Daryono, B. S., "Morphological variations of superior sugarcane cultivars (Saccharum officinarum) from Lampung, Indonesia," Biodiversitas Journal of Biological Diversity, 23(8), 4110-4117, 2022.

[5] Lu G, Liu P, Wu Q, Zhang S, Zhao P, Zhang Y and Que Y, "Sugarcane breeding: a fantastic past and promising future driven by technology and methods," Front. Plant Sci, 15:1375934, 2024. doi: 10.3389/fpls.2024.1375934

[6] Zhang X, Wang J, Noor-Ul-Áin, Que Y, Zhang J, Abid J, Zhao P, Zhang Y, Lin J, Chen LY, Bao Y, Herry R, Tangphatsornruang S, Wang Q, Huang D, Ye J, Zhang M, Luo M, Butterfield M, Wang R, Ming R., "International research initiative on genomics-guided sugarcane breeding," Mol Plant, 2025 Feb 3;18(2):171-174. doi: 10.1016/j.molp.2025.01.003.

[7] Nikam AA, Devarumath RM, Ahuja A, Babu H, Shitole MG, Suprasanna P, "Radiation-induced in vitro mutagenesis system for salt tolerance and other agronomic characters in sugarcane (Saccharum officinarum L)," Crop J, 3:46–56, 2014. https://doi.org/10.1016/j.cj.2014.09.002

[8] Sandhu SK, Singh R, Suprasanna P., "Radiation-induced mutants with increased cane number in sugarcane variety," CoJ 85, J Crop Improv, 33:2, 2019. https://doi.org/10.1080/15427528.2018.1554546

[9] Purankar MV, Nikam AA, Devarumath RM, Suprasanna P., "Radiation induced mutagenesis, physio-biochemical profiling and field evaluation of mutants in sugarcane cv," CoM 0265, Int J Radiat Biol, 98:7, 2022. https://doi.org/10.1080/09553002.2022.2024291

[10] Barrientos-Alfaro, F.C., Echeverría-Beirute, F., Hernández-Soto, A. et al., "Mutation breeding strategies and advances for sugarcane (Saccharum spp.) improvement," Plant Cell Tiss Organ Cult, 162, 66 (2025). https://doi.org/10.1007/s11240-025-03188-y

[11] Tsuchikawa, S., Kobori, H., "A review of recent application of near infrared spectroscopy to wood science and technology," J Wood Sci, 61, 213–220, 2015. https://doi.org/10.1007/s10086-015-1467-x

Development, Validation and Routine Implementation of Near-Infrared Spectroscopy for Quantitative Analysis of Oil Palm Leaf Nutrients

Petronella G. Ah Tung[1*], Nur Izzah Aimi binti Ramli[1], Tan Suet Yee[1]

[1]Advanced Agriecological Research Sdn. Bhd., Malaysia

***Corresponding author:** Petronella G. Ah Tung — petnella@aarsb.com.my

Abstract

Near-infrared spectroscopy (NIRS) was developed as a rapid, non-destructive and reagent-free secondary method for quantitative analysis of oil palm leaf nutrients. Calibration models for ash, nitrogen (N), phosphorus (P), potassium (K), magnesium (Mg), calcium (Ca) and boron (B) were developed from 7,340 to 10,981 routine samples using standard normal variate plus detrending and a 1-16-16-1 first-derivative treatment. Modified partial least squares was selected for ash, while artificial neural networks were selected for the nutrients. Models for ash, N, P, K, Mg and Ca passed validation and independent verification. During extended verification, these models achieved R^2 values of 0.90-0.96 and ratios of performance to deviation of 3.03-4.44. Agreement with agronomic nutrient-status classifications ranged from 79.0% to 87.2%. Post-implementation assessment of commercial samples found negligible mean bias. The B model did not meet the required R^2 and verification criteria and remains under development. The accepted models support routine screening, faster reporting and reduced reliance on reagent-intensive analysis.

Keywords: *artificial neural network, chemometrics, method validation, near-infrared spectroscopy, nutrient analysis, oil palm leaf*

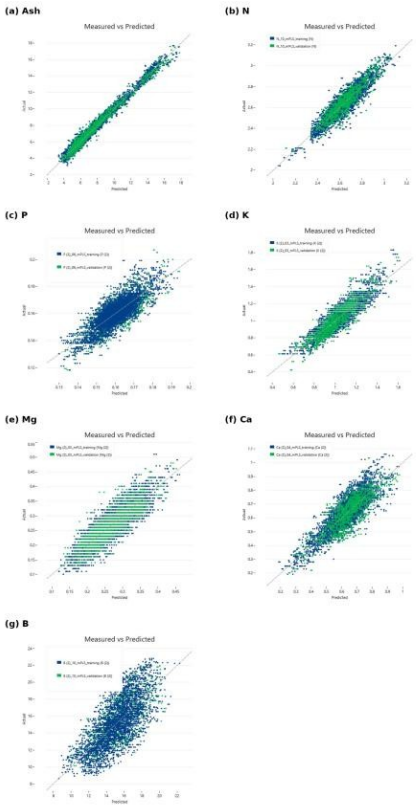

Figure 1. Calibration and validation plots for ash, N, P, K, Mg, Ca and B. Blue points represent calibration data and green points represent validation data.

1. Introduction

Leaf nutrient analysis supports fertiliser recommendations, but conventional determination of ash and mineral nutrients requires several preparation and instrumental procedures. NIRS offers a rapid, reagent-free alternative. Although minerals lack distinct NIR absorption bands, their concentrations can be estimated indirectly from relationships between spectra and reference values [1]-[3]. This study evaluated the complete NIRS method lifecycle for oil palm leaf analysis, from calibration development to routine monitoring.

2. Methodology

Routine samples covered diverse estates, soil conditions, palm ages and nutrient concentrations. Dried, 1 mm-ground samples were scanned twice with a FOSS NIRS DS2500 over 400-2500 nm. Reference values came from established laboratory methods. Data were divided into 80% calibration and 20% validation subsets, with spectral outliers screened by principal component analysis. All models used standard normal variate plus detrending and a 1-16-16-1 first derivative. mPLS and ANN regression were assessed with Venetian-blinds cross-validation.

Acceptance included $R^2 \geq 0.70$, stable prediction errors and acceptable relative measurement uncertainty. Preliminary verification used 100 independent samples per analyte. Extended verification used 671-894 samples and required $R^2 \geq 0.90$, RPD > 3, acceptable prediction error and controlled bias under ISO 12099 principles [4]. Nutrient-status agreement above 70% was considered satisfactory. Post-implementation agreement was assessed for 1,299-1,840 samples using Bland-Altman analysis [5].

3. Results and Discussion

The calibration sets contained 7,340-10,981 samples. mPLS gave the best ash model, while ANN was selected for all nutrients. Ash, N, P, K, Mg and Ca passed validation, with R^2 values of 0.719-0.984. B failed with $R^2 = 0.565$. Preliminary verification of the accepted models produced RPD values of 3.20-6.50 and R^2 values of 0.909-0.977. In extended verification, RPD remained above 3.0, R^2 remained at 0.90-0.95, and prediction error and bias stayed within control limits.

Classification agreement was 84.5% for N, 85.7% for P, 79.0% for K and 87.2% for Mg. Disagreement occurred mainly near class boundaries. Post-implementation mean relative bias was below 0.2%, with no significant mean bias at $p < 0.05$. Between 90.0% and 92.6% of results fell within the limits of agreement. Small concentration-dependent trends for N and K require continued monitoring.

The accepted models entered routine service. Ongoing control should track prediction statistics, classification agreement and spectral outliers. Calibration updates should target under-represented classes and concentration extremes. Critical borderline results should be confirmed by reference methods. B remains under development.

4. Conclusion

NIRS was successfully developed, validated and implemented as a secondary method for routine analysis of ash, N, P, K, Mg and Ca in oil palm leaves. Verification, classification agreement and post-implementation results support rapid routine screening and agronomic interpretation while reducing reliance on reagent-intensive analysis. Scheduled verification, targeted calibration expansion and reference confirmation of critical borderline results are required to maintain reliability. Boron remains a development model and should not be reported routinely.

Acknowledgement

The authors thank Kuala Lumpur Kepong Berhad and Boustead Plantations Berhad for granting permission to publish this study. The authors also acknowledge the chemistry laboratory staff for their assistance. This research was financially supported by Advanced Agriecological Research Sdn. Bhd.

References

[1] J. A. Prananto, B. Minasny, and T. Weaver, "Near infrared spectroscopy as a rapid and cost-effective method for nutrient analysis of plant leaf tissues," Advances in Agronomy, vol. 164, pp. 1-49, 2020, doi: 10.1016/bs.agron.2020.06.001.

[2] H. Jayaselan, N. Nawi, W. Ismail, A. Shariff, V. Rajah, and X. Arulandoo, "Application of spectroscopy for nutrient prediction of oil palm," Journal of Experimental Agriculture International, vol. 15, no. 3, pp. 1-9, 2017, doi: 10.9734/JEAI/2017/31502.

[3] Y. Y. Devianti, P. Satriyo, and A. A. Munawar, "Rapid prediction of soil quality indices using near infrared spectroscopy," IOP Conference Series: Earth and Environmental Science, vol. 365, p. 012043, 2019, doi: 10.1088/1755-1315/365/1/012043.

[4] International Organization for Standardization, ISO 12099:2017 Animal feeding stuffs, cereals and milled cereal products - Guidelines for the application of near infrared spectrometry, Geneva, Switzerland, 2017.

[5] J. M. Bland and D. G. Altman, "Statistical methods for assessing agreement between two methods of clinical measurement," The Lancet, vol. 327, no. 8476, pp. 307-310, 1986, doi: 10.1016/S0140-6736(86)90837-8.

Near Infrared Reflectance Spectroscopy: A Green Technology Analysis in Supporting Agriculture Sector of Sarawak

Margaret Abat[1*], Syazwani Bakar[1], Irna Syairina Sahari[1], Christine Jinang[1]

[1]Agriculture Research Centre Semenggok, Department of Agriculture Sarawak, KM20, Borneo Heights Road, 93250 Kuching, Sarawak, Malaysia

***Corresponding author:** margarea@sarawak.gov.my

Abstract

Near-infrared reflectance spectroscopy (NIRS) is rapidly emerging as a preferred analytical method for quantifying the physical, chemical, and nutritional properties of agricultural materials. Between 2020 and 2025, about 4,000 diverse samples comprising soil, crops, plants, fertilisers, and food products were scanned using NIRS to develop calibration and prediction models for multi-element and proximate composition. The resulting correlation coefficients (R^2) and predictive performance ranged from poor to excellent, depending on the specific element and matrix analysed. The findings suggested that NIRS has great potential and robustness in predicting nutrient compositions across selected agricultural products.

Keywords: *nutrient compositions, food crop, soil, fertiliser*

1. Introduction

Near-infrared reflectance spectroscopy (NIRS) is a non-destructive, chemical-free, and reagent-free secondary analytical method widely used in the pharmaceutical, chemical, agricultural, and food sectors (Towett et al., 2013). In Sarawak, the adoption of NIRS technology is relatively new, and limited information exists regarding its application in agriculture. Therefore, a feasibility study on the potential and efficiency of NIRS to deliver reliable, accurate data in support of precision agriculture in Sarawak is essential. Sustainable agriculture relies on accurate, timely information regarding soil properties, crop nutrient status, and fertiliser composition to enable precise fertiliser management. However, obtaining these measurements rapidly, reliably, and cost-effectively remains a challenge. The objectives of this study were to develop calibration models and evaluate the predictive capability of NIRS for determining the quality, properties, and composition of soil, plant, crop, and fertiliser materials.

2. Methodology

The NIRS technology is based on the absorption of energy by molecular functional groups such as C-H, C-C, C=C, C-N, and O-H, which are characteristic of organic matter within the near-infrared region of 700 to 2500 nm (Ludwig and Khanna, 2001). For spectral measurements, prepared samples were scanned across a full wavelength range of 400 to 2500 nm, with data recorded at 2-nm intervals. Standard normal variate transformation combined with detrending (SNV-D) was applied for scatter correction, along with various mathematical treatments for derivative order, gap, and smoothing using WinISI 4 software. Calibration equations were developed using modified partial least squares (mPLS) regression with cross-validation. The performance of the calibration models was evaluated using the coefficient of determination in calibration R^2, standard error of calibration (SEC), and standard error of cross-validation (SECV). Model selection was based on maximizing R^2 while minimizing SEC and SECV. The predictive capability of the models was evaluated using statistical parameters including the root mean square error of prediction (RMSEP) and the ratio of performance to deviation (RPD). For reference, target elements and analytes were measured using conventional laboratory reference methods. Soil, plant, crop, and fertiliser samples were obtained from ongoing research and development activities as well as agricultural projects managed by the Department of Agriculture Sarawak and its stakeholders.

3. Results and Discussion

The R^2_{Calib} values for total N, P_2O_5, K_2O and MgO of the selected fertiliser formulations were ranged from 0.501 to 0.992, indicating a fair to excellent correlations between the laboratory-analysed and NIRS-predicted values (*Table 1*). For crop and plant samples, R^2_{Calib} values for N, P, K, Ca, acidity, ash, total fat and ascorbic acid were between 0.850 and 0.960, showing a very good to excellent correlation, and highly reliable for precise quantification (*Table 1*). The R^2_{Calib} values for Zn, B, carbohydrate, crude fibre, and pencycuron were ranged from 0.690 to 0.820, indicating a good correlation and suitable for approximate quantitative prediction (*Table 1*). The R^2_{Calib} values for Fe, crude protein, and emamectin benzoate were fair, at 0.580, 0.550, and 0.578 respectively, perhaps reliable for rough discrimination or screening (*Table 1*). The R^2_{Calib} values for Mn, and Cu were poor, (< 0.500), which is unreliable for quantification. In soil samples, the R^2_{Calib} values, except for hot water B, were between 0.890 to 1.00, indicating a very good to excellent correlation (*Table 1*).

For the validation on the independent datasets, the R^2_{valid} values for total P_2O_5, K_2O and MgO were between 0.680 to 0.880 (*Table 1*), indicating that the models are good, acceptable and reliable for most routine agricultural application, with a good and excellent performance tier (RPD values > 2). For total N in the tested fertiliser samples, the R^2_{valid} value was 0.447 which is considered poor and non-reliable although the RPD value indicating an excellent performance (*Table 1*). In this study, RPD thresholds were defined as acceptable for values between 1.4 and 2 ($1.4 < \text{RPD} < 2$). The models were deemed as good and excellent if the RPD is more than 2 (RPD >2), following Saeys et al. (2005). The R^2_{valid} values for total N, P, K, Ca, Mn, Zn, ash, carbohydrate, total fat, crude fibre and ascorbic acid in crop and plant samples were between 0.650 and 0.970, signifying that the models are good and excellent for these nutrient and proximate compositions prediction (*Table 1*). The calculated RPD values for these compositions also supported the validation models (*Table 1*). The models with R^2_{valid} values > 0.90 were considered highly accurate and suitable for strict quality control, regulatory reporting and precise quantitative analysis. Although the R^2_{calib} for acidity and pencycuron were ranging from good to excellent, the R^2_{valid} and RPD values were poor and non-acceptable, indicating that the model is not reliable and lack of predictive capability (*Table 1*). For elements such as Mg, Fe, Cu and B, the validation models also poor and non-acceptable, in agreement with the poor and/or fair R^2_{calib} values. The validation models for all selected parameters in soil samples, except for hot water B and fine sand, were very good and excellent with R^2_{valid} values ranging from 0.86 to 1.00 with calculated RPD values between 2.64 and 15.39 (*Table 1*). Although the R^2_{Calib} value for fine sand appeared very good, its RMSEP is relatively high and RPD value was low (*Table 1*), indicating that the calibration model could not accurately predict this parameter in the selected samples.

The main factor limiting the predictive performance of NIRS across certain matrix-nutrient combinations is likely due to the sample size restriction. Sample size constraints have similarly been cited as a main factor of low R^2 values when predicting digestible energy and metabolisable energy in corn (Li et al., 2016). In addition, the model's performance may have been compromised by non-optimised mathematical treatments, incompatible spectral preprocessing methods, or non-representative sample sets. For sample without prior drying such as fertiliser, the residual moisture variation and particle size heterogeneity will likely introduce further noise into the calibration. Model robustness could be enhanced by expanding sample diversity, optimising spectral preprocessing routines, and refining data extraction protocols.

Table 1. The calibration and prediction results for soil, crop, fertiliser and analytes of interests

Matrix	Constituent	Calibration model		Validation model		
		RMSEC	R^2_{calib}	RMSEP	R^2_{valid}	RPD
Fertiliser (n ~ 1800 to 1900 of various fertiliser formulations such as urea, NPK compounds, mixture etc.)	Nitrogen, N	1.109	0.501	1.116	0.447	3.566
	Phosphorus, P_2O_5	1.981	0.790	2.421	0.680	2.216
	Potassium, K_2O	2.339	0.844	2.788	0.780	2.125
	Magnesium, MgO	0.258	0.882	0.230	0.880	3.190
Food Crops (n = ~1500 - 1600) Consisted of different varieties of fruits and vegetables	Nitrogen, N	0.291	0.960	7.365	0.650	1.705
	Phosphorus, P	0.114	0.890	0.446	0.870	2.870
	Potassium, K	0.897	0.850	0.743	0.900	3.230
	Calcium, Ca	0.810	0.810	0.370	0.840	2.324
	Magnesium, Mg	5.858	0.180	3.778	0.130	0.032
	Iron, Fe	319.29	0.580	1326	0.000	0.096
	Manganese, Mn	13.549	0.390	7.365	0.650	1.705
	Copper, Cu	6.761	0.100	3.863	0.440	1.305
	Zinc, Zn	13.97	0.690	11.007	0.850	2.017
	Boron, B	3.00	0.700	3.557	0.63	1.294
	Acidity	4.277	0.990	34.685	0.601	1.069
	Ash	1.251	0.890	1.606	0.82	2.276
	Carbohydrate	10.408	0.712	8.901	0.766	2.060
	Total fat	1.158	0.990	1.884	0.96	5.005
	Crude fibre	4.342	0.800	4.031	0.65	1.644
	Crude protein	38.55	0.550	36.232	0.08	0.217
	Ascorbic acid (Vitamin C)	14.154	0.950	15.183	0.97	5.405
	Pesticide residues (organophosphorus)					
	Emamectin benzoate	0.007	0.578	0.006	0.254	1.667
	Pencycuron	1.379	0.820	1.306	0.474	1.374

Matrix	Constituent	Calibration model		Validation model		
		RMSEC	R^2_{calib}	RMSEP	R^2_{valid}	RPD
Soil (n ~ 500 - 600) Different soil types obtained from the proficiency testing programmes organised by Agriculture Laboratory Association Malaysia (AgLAM) and Wageningen Evaluation Program for Analytical Laboratory (WEPAL)	pH	0.137	0.980	0.078	1.00	14.67
	Total nitrogen, N	0.015	0.980	0.015	0.985	12.00
	Total organic carbon, TOC	0.050	1.000	0.089	1.00	16.44
	Exchangeable calcium, Ca	0.884	1.000	4.821	0.88	2.773
	Exchangeable potassium, K	0.011	1.000	0.020	0.990	9.500
	Exchangeable magnesium, Mg	0.070	0.990	0.062	0.996	15.48
	Exchangeable sodium, Na	0.033	0.980	0.021	0.990	11.00
	Cation exchange capacity, CEC	0.598	0.990	0.771	0.99	10.18
	Available phosphorus, P	27.289	0.950	28.552	0.95	4.377
	Hot water boron, B	0.320	0.680	0.375	0.55	1.417
	Loss of ignition, LOI	0.122	1.000	0.225	1.00	14.56
	Moisture	0.088	1.000	0.091	1.00	15.39
	Particle size					
	Clay	4.174	0.950	4.002	0.95	4.370
	Silt	3.561	0.910	4.454	0.86	2.643
	Fine sand	3.053	0.890	8.839	0.35	0.813
	Coarse sand	4.297	0.950	4.352	0.95	4.683

4. Conclusion

Near-infrared reflectance spectroscopy (NIRS) is a promising technology for rapidly determining the quality, properties, and nutrient compositions of agricultural produce and inputs with an acceptable degree of accuracy. However, variations across sample matrices and attributes highlight the need for more robust and generalised models. Future work should incorporate larger datasets and external validation to enhance model reliability and practical applicability under real-time and *in-situ* agricultural conditions. One of the primary limitations associated with NIRS in this study was the challenge of obtaining an adequate calibration dataset and having a sufficient number of samples with accurate data. Predictions for samples outside the calibrated range may be unreliable; therefore, calibration datasets must span both the low and high concentration ranges for each parameter. Furthermore, while the precision of NIRS can equal or surpass conventional laboratory methods due to its higher repeatability, its predictive accuracy depends on continuous refinement and may improve over time as the calibration dataset expands.

Acknowledgements

The authors thank the Department of Agriculture Sarawak and the Government of Sarawak for their financial support and assistance throughout this study. The technical support provided by the laboratory staff is highly appreciated

References

Li, J., Li, D., Chen, Y., Wang, X., Yang, W., and Zhang, L. (2016). Use of near infrared reflectance spectroscopy for the rapid determination of digestible energy and metabolizable energy content of corn fed to growing pigs. Journal of Animal Science and Biotechnology 7, 1 - 9

Ludwig, B., and Khanna, P. (2001). Use of near infrared spectroscopy to determine inorganic and organic carbon fractions in soil and litter. Assessment Methods Soil Carbon, 360-370.

Saeys, W., Mouazen, A. M., and ramon, H. (2005). Potential for onsite and online analysis of pig manure using visisble and near infrared spectroscopy. Biosystem Engineering 91, 393-402.

Towett, E. K., Alex, M., Sheperd, K. D., Polreich, S., Aynekulu, E., and Maass, B. L. (2013). Applicability of near-infrared reflectance spectroscopy (NIRS) for determination of crude protein content in cowpea (*Vigna unguiculata*) leaves. Food Science and Nutrition 1, 45-53.

Preliminary Quantification of Palm Oil Adulteration in Virgin Coconut Oil Using MicroNIR Spectroscopy and Chemometrics

Mohd Fared Abdul Khir[1*], Mohd Norzaliman Mohd Zain[2]

[1]Faculty of Science and Technology, Universiti Sains Islam Malaysia, Bandar Baru Nilai, 71800 Nilai, Negeri Sembilan, Malaysia

[2]MIMOS Quantum Intelligence, MIMOS Berhad, 57000, Kuala Lumpur, Federal Territory of Kuala Lumpur, Malaysia

***Corresponding author:** fared.khir@usim.edu.my

Abstract

Virgin coconut oil (VCO) is a high-value edible oil that may be adulterated with lower-cost oils such as palm oil. This preliminary study evaluated the feasibility of portable MicroNIR spectroscopy combined with chemometrics for rapid quantification of palm oil in VCO. Five concentration levels (0, 10, 20, 30, and 50% palm oil) were prepared independently in triplicate, and each preparation was scanned three times, yielding 45 spectra and 15 independent preparation means over 908-1676 nm. Spectral preprocessing included Savitzky-Golay smoothing, standard normal variate (SNV), multiplicative scatter correction (MSC), first derivative, and their combinations. Principal component analysis (PCA) was used to examine spectral variation, while partial least squares (PLS) regression was evaluated using three-fold cross-validation based on independent sample preparations. The best model combined SNV with a Savitzky-Golay first derivative and three PLS components, achieving R^2_{CV} = 0.9969, RMSECV = 0.959% palm oil, MAECV = 0.758%, and bias = -0.092%. These preliminary findings support the potential of Shortwave NIR spectroscopy and chemometrics for rapid estimation of palm oil adulteration in VCO across the investigated 0-50% range. Further studies with larger independent sample sets and external validation are required to establish model robustness.

Keywords: *adulteration, chemometrics, MicroNIR, palm oil, partial least squares regression, virgin coconut oil*

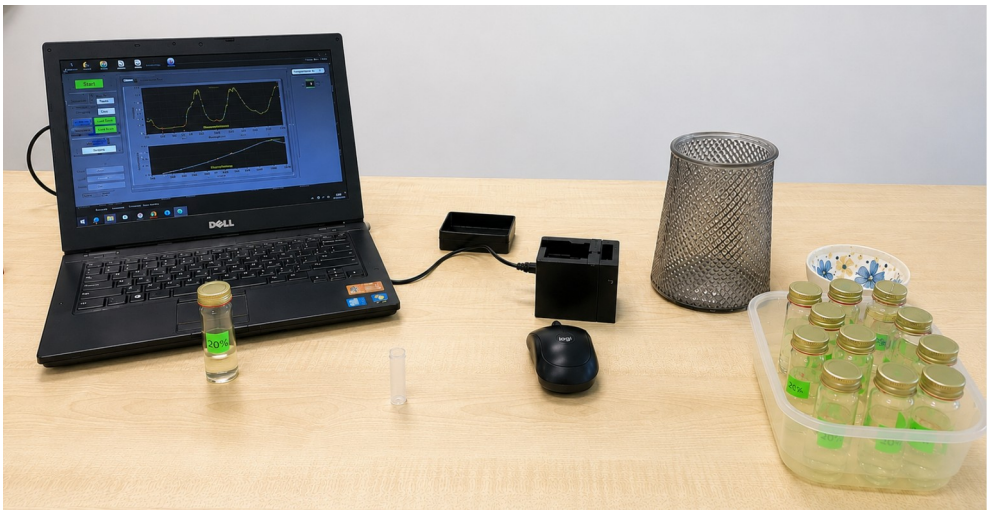

Figure 1. Experimental setup for MicroNIR spectral data acquisition.

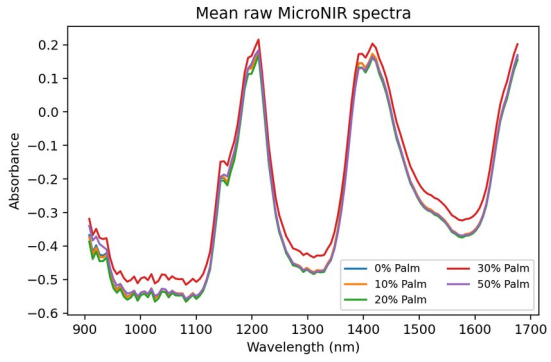

(a) mean raw MicroNIR spectra

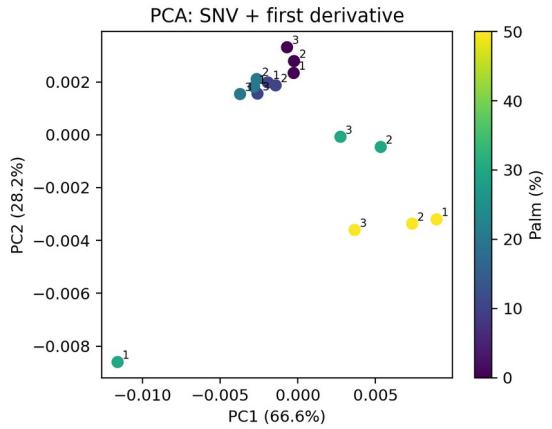

(b) PCA scores after SNV and first-derivative preprocessing

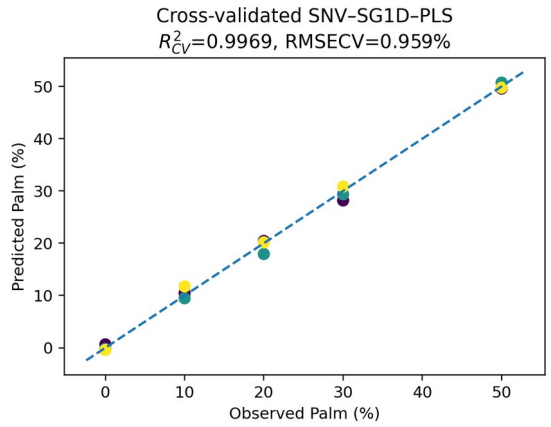

(c) cross-validated observed versus predicted palm oil concentration

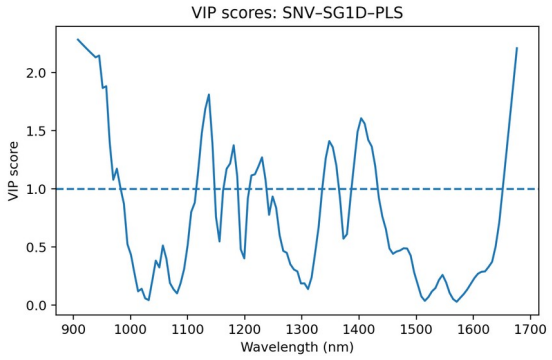

(d) VIP scores of the final PLS model

Figure 2. Preliminary spectral and chemometric results for the selected 0-50% palm oil concentration series: (a) mean raw MicroNIR spectra; (b) PCA scores after SNV and first-derivative preprocessing; (c) cross-validated observed versus predicted palm oil concentration; and (d) VIP scores of the final PLS model.

1. Introduction

Virgin coconut oil is valued for its nutritional, sensory, and commercial attributes, making authentication important for quality assurance. Palm oil is a plausible lower-cost adulterant, and previous work has demonstrated that vibrational spectroscopy coupled with chemometrics can quantify oil adulteration. FTIR-PLS has been applied directly to palm oil adulteration in VCO [1], while NIR spectroscopy has shown strong potential for quantitative analysis of edible-oil blends [2]. Near-infrared hyperspectral imaging has also been used to quantify palm kernel oil adulteration in VCO, further demonstrating the potential of NIR-based techniques for edible-oil authentication [3]. Because spectral preprocessing can strongly affect multivariate models [4], a compact comparison of scatter-correction and derivative methods is needed when using portable NIR instruments. This preliminary study therefore investigates whether Shortwave NIR spectra can support quantitative estimation of palm oil in VCO over a selected 0-50% concentration series and identifies a suitable preprocessing-PLS workflow for subsequent full-scale study.

2. Methodology

Five palm oil concentrations in VCO (0, 10, 20, 30, and 50%) were selected for the conference-stage analysis. Three independent sample preparations were available at each concentration. Each preparation had three technical MicroNIR scans, giving 45 spectra. The experimental arrangement used for data collection, comprising the MicroNIR measurement system, acquisition laptop, and prepared

sample vials, is shown in Figure 1. Spectra covered 908.1-1676.2 nm with 125 wavelength variables. The three technical scans from each physical preparation were averaged before PCA and regression, yielding 15 independent preparation means. The evaluated preprocessing methods were raw spectra, Savitzky-Golay smoothing, SNV, MSC, SNV followed by a Savitzky-Golay first derivative, and MSC followed by a Savitzky-Golay first derivative. PCA was performed after mean centering to examine dominant spectral variation. PLS regression models were tested with one to five latent variables. Model performance was assessed using three-fold cross-validation based on independent sample preparations: in each fold, one preparation replicate across all five concentrations was held out for validation, while the remaining two replicates were used for calibration. Performance was summarized using RMSECV, MAECV, R^2_{CV}, and bias. Variable importance in projection (VIP) scores were calculated for the selected model, with VIP >= 1 used as an interpretive screening threshold [5].

3. Results and Discussion

The mean raw spectra displayed similar overall spectral profiles across the five concentration levels, with concentration-dependent differences in absorbance superimposed on baseline and intensity variation (Figure 2a). After SNV and first-derivative preprocessing, the PCA score plot showed clearer concentration-related separation, indicating that preprocessing reduced non-chemical variation and enhanced spectral differences associated with palm oil content (Figure 2b). Across the tested PLS models, derivative-based preprocessing gave the lowest cross-validated prediction error (*Table 1*).

Table 1. Cross-validated PLS performance for the MNIRSM subset.

Preprocessing	LV	RMSECV	MAECV	R²CV	Bias
SNV + 1st derivative	3	0.959	0.758	0.9969	-0.092
MSC + 1st derivative	3	1.002	0.774	0.9966	-0.115
MSC	5	1.074	0.876	0.9961	-0.319
SNV	5	1.078	0.878	0.9961	-0.32
Raw	5	1.761	1.489	0.9895	-0.053
SG smoothing	5	2.236	1.901	0.9831	-0.097

The best model used SNV followed by a Savitzky-Golay first derivative with three PLS components. It achieved R^2_{CV} = 0.9969, RMSECV = 0.959% palm oil, MAECV = 0.758%, and bias = -0.092%. The cross-validated observed-versus-predicted plot showed close agreement with the 1:1 relationship across the investigated concentration range (Figure 2c), while the small bias indicates little overall systematic over- or under-prediction across the three validation folds. The corresponding MSC-derivative model performed similarly but with slightly higher RMSECV (1.002%). In contrast, raw and smoothing-only models produced larger errors, indicating that correction of spectral scatter/baseline effects and enhancement of local spectral changes were beneficial for this subset. VIP analysis identified 43 wavelengths with VIP >= 1 (Figure 2d). These variables should be interpreted as model-important wavelengths rather than direct proof of chemical specificity, particularly because VIP can be sensitive to model structure and sample size [5]. The strong cross-validation statistics are encouraging, but the present analysis contains only 15 independent preparations. Consequently, the results should be regarded as preliminary and should not be interpreted as external validation.

4. Conclusion

Portable Shortwave NIR spectroscopy in particular MicroNIR spectrometer combined with chemometrics showed strong preliminary potential for quantifying palm oil in VCO over the selected 0-50% concentration range. Among the tested approaches, SNV followed by a Savitzky-Golay first derivative and a three-component PLS model provided the best cross-validated performance. The preparation-based cross-validation design avoided treating technical replicate scans as independent

samples and therefore provided a more defensible estimate of internal predictive performance. The next stage of the study will extend the analysis to the complete concentration series and evaluate model robustness using larger independent sample sets and external validation.

References

[1] A. Rohman and Y. B. Che Man, "Monitoring of virgin coconut oil (VCO) adulteration with palm oil using Fourier transform infrared spectroscopy," Journal of Food Lipids, vol. 16, no. 4, pp. 618-628, 2009.

[2] H. Zhang, X. Hu, L. Liu, J. Wei, and X. Bian, "Near infrared spectroscopy combined with chemometrics for quantitative analysis of corn oil in edible blend oil," Spectrochimica Acta Part A: Molecular and Biomolecular Spectroscopy, vol. 270, art. 120841, 2022.

[3] P. Jermwongruttanachai, S. Pathaveerat, and S. Noypitak, "Quantification of the adulteration concentration of palm kernel oil in virgin coconut oil using near-infrared hyperspectral imaging," Journal of Integrative Agriculture, vol. 23, no. 1, pp. 298-309, 2024.

[4] Å. Rinnan, F. van den Berg, and S. B. Engelsen, "Review of the most common pre-processing techniques for near-infrared spectra," TrAC Trends in Analytical Chemistry, vol. 28, no. 10, pp. 1201-1222, 2009.

[5] B. Mahieu, E. M. Qannari, and B. Jaillais, "Extension and significance testing of Variable Importance in Projection (VIP) indices in Partial Least Squares regression and Principal Components Analysis," Chemometrics and Intelligent Laboratory Systems, vol. 242, art. 104986, 2023.

Defect Emission from $BaSi_2$ Thin Films Prepared by co-Sputtering Technique

Abdul Rahman Mohmad[1*], Kazuki Kido[2], Takashi Suemasu[2,3]

[1]Institute of Microengineering and Nanoelectronics, Universiti Kebangsaan Malaysia, 43600 UKM Bangi, Selangor, Malaysia

[2]Graduate School of Pure and Applied Sciences, University of Tsukuba, Tsukuba, Ibaraki 305-8573, Japan

[3]Department of Applied Physics, Faculty of Pure and Applied Sciences, University of Tsukuba, Tsukuba, Ibaraki 305-8573, Japan

***Corresponding author:** armohmad@ukm.edu.my

Abstract

In this work, we investigate the surface morphology and optical quality of $BaSi_2$ samples prepared via the co-sputtering technique. The samples were investigated using atomic force microscopy (AFM) and low-temperature, power-dependent photoluminescence (PL). To produce a high-quality, stoichiometric $BaSi_2$ film, both $BaSi_2$ and Ba targets were used. A series of samples with varying Ba-to-$BaSi_2$ growth rate ratios ($GRBa/GRBaSi_2$) from 0 to 0.36 were fabricated. AFM images indicated a significant decrease in root mean square (rms) roughness as $GRBa/GRBaSi_2$ increased. At 10 K, sample A ($GRBa/GRBaSi_2 = 0$) showed strong PL emission at ~0.92 eV (P1). In contrast, samples with $GRBa/GRBaSi_2 > 0.18$ exhibited weak, nearly absent PL, implying a lower defect density than sample A. With higher excitation power, the P1 peak saturated, and a new peak at ~1.27 eV (P2) appeared. Power-dependent PL measurements yielded a power-law exponent of 1/2 for P1, characteristic of a deep donor-to-deep acceptor transition. The 1.27 eV peak (P2) may correspond to a deep donor-to-free hole transition. Our results demonstrate that employing both $BaSi_2$ and Ba targets effectively reduces defect density in sputtered $BaSi_2$ films.

Keywords: *barium disilicide; photoluminescence; sputtering; defects;*

1. Introduction

Increasing interest has been shown towards barium disilicide ($BaSi_2$) as a promising material for light absorption in solar cell applications. This is primarily due to its large absorption coefficient of approximately 3×10^4 cm^{-1} at 1.5 eV, which is ~30 times greater than that of Si [1]. $BaSi_2$ also exhibits a significant minority carrier diffusion length of ~11 μm and a long minority carrier lifetime of ~10 μs [2-4]. Additionally, $BaSi_2$ has a room temperature band gap of ~1.3 eV, which is closer to the ideal band gap of a single-junction solar cell (1.4 eV), whereas Si has a smaller band gap of 1.1 eV [5]. Furthermore, the lattice mismatch between $BaSi_2$(100) and Si(111) substrates is only 1.1%, allowing for the growth of a relatively thick epitaxial layer without the formation of dislocations [6]. Solar cells based on $BaSi_2$ homojunction and p-$BaSi_2$/n-Si heterojunction configurations have been demonstrated, achieving efficiencies of ~10% [7, 8].

The growth of $BaSi_2$ films can be achieved through various techniques such as molecular beam epitaxy (MBE), sputtering, and thermal evaporation. In the case of MBE grown $BaSi_2$, the crystal quality and device characteristics have been found to be highly dependent on the Ba-to-Si deposition rate ratio [9]. Recently, the deposition of $BaSi_2$ films using cost effective techniques like sputtering has been reported [10-12]. However, controlling the Ba-to-Si atomic ratio using a single $BaSi_2$ target is challenging, often resulting in a Ba-deficient film or a non-stoichiometric $BaSi_2$ [13]. Therefore, co-sputtering using dual source targets, specifically $BaSi_2$ and Ba, may be necessary to obtain a stoichiometric and high-quality $BaSi_2$ film. In this work, we aim to assess the morphology and optical quality of $BaSi_2$ films grown using $BaSi_2$ and Ba targets. Photoluminescence (PL) analysis will also be performed to investigate defect emissions and their likely origin.

2. Methodology

The $BaSi_2$ samples reported in this work were prepared using a plasma sputtering system equipped with $BaSi_2$, Ba, and Si targets. Initially, the sputtering chamber was evacuated to a base pressure of 10^{-3} Pa. Subsequently, a Si(111) substrate was heated to 600 °C for the deposition of the $BaSi_2$ film. The RF power of the $BaSi_2$ target, $PBaSi_2$, was set at either 30 or 70 W, while the power of the Ba target, PBa, was varied from 0 to 40 W. The $BaSi_2$ layer was grown with a thickness ranging between 314 and 476 nm. Finally, a 3 nm thick layer of amorphous Si was deposited as a cap on the $BaSi_2$ layer. The growth conditions of the samples are summarized in Table 1. Further details regarding the determination of the sputtering ratio of the Ba target to the $BaSi_2$ growth rate ($GRBa/GRBaSi_2$) can be found in Ref. [14].

For PL measurements, the sample was placed inside a closed-loop liquid helium cryostat and cooled to 10 K. Subsequently, the sample was excited by a continuous-wave laser emitting at 532 nm. The emitted PL was dispersed into different wavelengths using a monochromator (Horiba iHR320) and detected by an electrically cooled InGaAs detector with a detection range between 800 and 1650 nm. The surface morphology of the samples was examined using tapping mode atomic force microscopy (AFM).

Table 1. Summary of sputtering conditions used for the deposition of BaSi2 films

Sample name	PBaSi2 [W]	PBa [W]	GRBa/GRBaSi2
A	30	0	0
B	30	20	0.18
C	70	30	0.26
D	70	40	0.36

3. Results and Discussion

First, the relationship between $GRBa/GRBaSi_2$ and surface morphology was investigated. Figure 1 displays the AFM images of samples A, B, and C. The rms roughness of samples A, B, and C is 107 nm, 31 nm, and 19 nm, respectively. Sample A exhibits the highest rms roughness due to the presence of a high density of 3D features with lateral dimensions of ~0.5 to 1 μm and heights up to 600 nm. These 3D features were not observed in samples B and C, resulting in a significant reduction in rms roughness as the $GRBa/GRBaSi_2$ ratio increased.

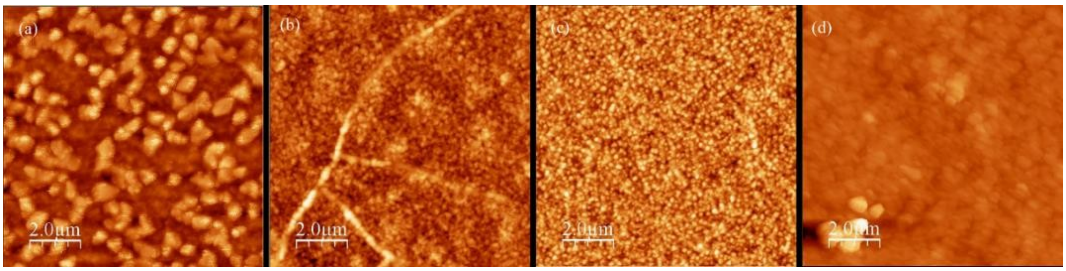

Fig. 1. AFM images of sample (a) A, (b) B, (c) C and (d) D. The scan size for each image is 10 × 10 μm.

Figure 2(a) shows the PL spectra of samples A-D measured at 10 K. Sample A exhibits a broad PL emission with a peak energy of ~0.92 eV, whereas the other samples display weak and negligible PL emissions. It is important to note that $BaSi_2$ is an indirect bandgap material with a calculated bandgap energy of 1.4 eV at 0 K [15]. Considering that the observed PL emission is significantly smaller than the expected bandgap energy, it is likely that the observed PL emission originates from mid-gap or defect states located below the bandgap. This suggests that sample A, which was grown without the Ba target (PBa = 0 W), is the most defective sample. However, due to the weak PL spectra observed for samples B-D, the relationship between $GRBa/GRBaSi_2$ and the density of defects remains unknown.

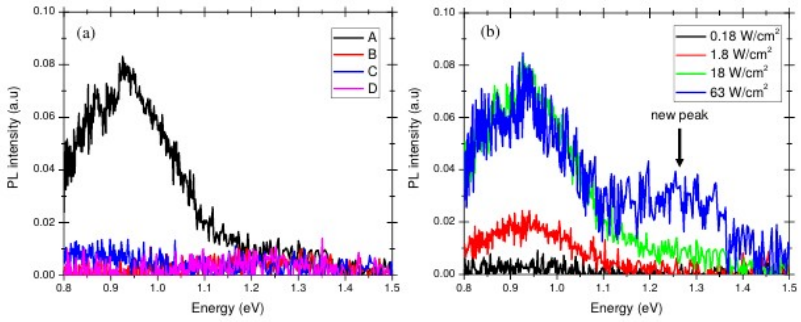

Fig. 2. (a) PL spectra of $BaSi_2$ samples measured at 10 K with excitation power of 18 W/cm² (b) Power dependent PL of sample A with excitation power between 0.18 and 63 W/cm².

To further investigate the PL emission, power dependent PL measurements were conducted on sample A, as depicted in Figure 2(b). Initially, the intensity of the PL peak at ~0.92 eV increases with higher excitation power, but it saturates at >18 W/cm². Simultaneously, a new peak at ~1.27 eV emerges at high excitation. This observation can be attributed to the saturation of defect states. As the excitation power increases, the defect states become fully occupied, resulting in the saturation of PL intensity. Further increase in excitation power leads to the occupation of another defect states or transitions at higher energies. This implies that the peak at ~1.27 eV may originate from another defect-to-defect state or defect-to-free exciton transition.

Since the PL spectra at >18 W/cm² comprise of two peaks, it is necessary to perform deconvolution. An example of peak deconvolution is presented in Figure 3(a). The PL peaks at ~0.92 eV and 1.27 eV are labeled as P1 and P2, respectively. Subsequently, the integrated PL intensity versus excitation power was plotted on a log-log scale, as shown in Figure 3(b). The dependence of PL intensity on excitation can be described by a simple power law, IPL ∝ Pex$k$, where IPL, Pex and k denote PL intensity, excitation power density, and the power law exponent, respectively. According to this power law, a value of $k < 1$ indicates defect-related transitions such as donor-to-acceptor, while values between 1 and 2 correspond to free excitonic transitions. For P1, the data at low and medium excitations fit well with a k value of 1/2, indicating a donor-to-acceptor transition as its origin. At high excitation levels, the k value shifts from 1 to 0 as the PL intensity saturates. As for P2, the available data points are insufficient to reliably determine the k value. However, based on the dashed line, the power exponent is ~1.

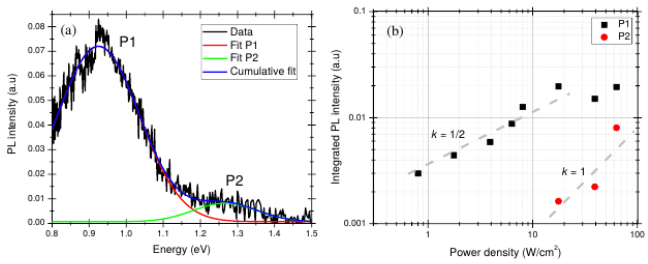

Fig. 3. (a) Deconvolution of PL spectra for sample A using two Gaussian curves (b) Integrated PL intensity versus excitation power. The dashed lines represent power law exponents.

Based on our PL results, we propose the origin of the PL emission, as illustrated in Figure 4. Previous studies have reported a deep donor level located ~0.2 eV below the conduction band minimum, attributed to Si vacancy defects [16]. Additionally, a deep acceptor level situated ~0.36 eV above the valence band maximum has been associated with the formation of Ba antisite defects [17]. Therefore, the PL emission denoted as P1 with a peak energy of 0.92 eV is likely to originate from the transition between deep donor and deep acceptor levels. The energy difference between the deep donor level and the valence band maximum is 0.92 + 0.36 = 1.28 eV. This value is close to the PL peak energy

of the P2 emission, which was measured at 1.27 eV. Thus, the P2 emission can be attributed to the deep donor-to-free hole transition.

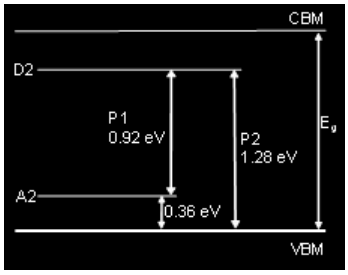

Fig. 4. Illustration of $BaSi_2$ band structure with defect levels and optical transitions. The D2 and A2 refer to deep donor and deep acceptor levels.

4. Conclusion

AFM and PL studies were conducted to evaluate the morphology and optical quality of $BaSi_2$ samples prepared using a co-sputtering technique. Samples grown with both $BaSi_2$ and Ba targets exhibited smaller rms roughness compared to sample A, which was grown using the $BaSi_2$ target alone. Additionally, PL emissions resulting from defect transitions were observed in sample A. Based on power dependent PL measurements, these PL emissions were attributed to transitions between deep donor-to-deep acceptor levels, as well as between deep donor-to-free hole. This work demonstrates the effectiveness of incorporating an additional Ba target during the deposition of $BaSi_2$ films in reducing the rms roughness and density of defects.

Acknowledgement

This work was funded by the Geran Universiti Penyelidikan, Universiti Kebangsaan Malaysia (GUP-2024-046), Malaysia Ministry of Higher Education through the Fundamental Research Grant Scheme (FRGS/1/2023/STG05/UKM/02/1) and by the Japan Society for the Promotion of Science (JSPS) KAKENHI (Grant Nos. 18H03767, 21H04548).

References

[1] K. Toh, T. Saito, and T. Suemasu, Optical absorption properties of $BaSi_2$ epitaxial films grown on a transparent silicon-on-insulator substrate using molecular beam epitaxy, Jpn. J. Appl. Phys. 50 (2011) 068001

[2] M. Baba, K. Toh, K. Toko, N. Saito, N. Yoshizawa, K. Jiptner, T. Sekiguchi, K.O. Hara, N. Usami, and T. Suemasu, Investigation of grain boundaries in $BaSi_2$ epitaxial films on Si(1 1 1) substrates using transmission electron microscopy and electron-beam-induced current technique, J. Cryst. Growth 348 (2012) 75

[3] K.O. Hara, N. Usami, K. Nakamura, R. Takabe, M. Baba, K. Toko, and T. Suemasu, Determination of Bulk Minority-Carrier Lifetime in $BaSi_2$ Earth-Abundant Absorber Films by Utilizing a Drastic Enhancement of Carrier Lifetime by Post-Growth Annealing, Appl. Phys. Express 6 (2013) 112302

[4] R. Takabe, K.O. Hara, M. Baba, W. Du, N. Shimada, K. Toko, N. Usami, and T. Suemasu, Influence of grain size and surface condition on minority-carrier lifetime in undoped n-$BaSi_2$ on Si(111), J. Appl. Phys. 115 (2014) 193510

[5] C.H. Henry, Limiting efficiencies of ideal single and multiple energy gap terrestrial solar cells, J. Appl. Phys. 51 (1980) 4494

[6] R.A. McKee, F.J. Walker, J.R. Conner, and R. Raj, $BaSi_2$ and thin film alkaline earth silicides on silicon, Appl. Phys. Lett. 63 (1993) 2818

[7] S. Yachi, R. Takabe, H. Takeuchi, K. Toko, and T. Suemasu, Effect of amorphous Si capping layer on the hole transport properties of $BaSi_2$ and improved conversion efficiency approaching 10% in p-$BaSi_2$/n-Si solar cells, Appl. Phys. Lett. 109 (2016) 072103

[8] K. Kodama, Y. Yamashita, K. Toko, and T. Suemasu, Operation of $BaSi_2$ homojunction solar cells on p+-Si(111) substrates and the effect of structure parameters on their performance, Appl. Phys. Express 12 (2019) 041005

[9] R. Takabe, T. Deng, K. Kodama, Y. Yamashita, T. Sato, K. Toko, and T. Suemasu, Impact of Ba to Si deposition rate ratios during molecular beam epitaxy on carrier concentration and spectral response of $BaSi_2$ epitaxial films, J. Appl. Phys. 123 (2018) 045703

[10] R. Koitabashi, T. Nemoto, M. Mesuda, K. Toko, and T. Suemasu, Fabrication of high-photoresponsivity $BaSi_2$ films formed on conductive layers by radio-frequency sputtering, Applied Physics Express 13 (2020) 075506

[11] R. Du, F. Li, K. Yang, Q. Li, W. Du, Y. Zhang, and T. Suemasu, Epitaxial growth of $BaSi_2$ thin films by co-sputtering of Ba and Si for solar cell applications, Applied Physics Express 14 (2021) 065501

[12] T. Nemoto, R. Koitabashi, M. Mesuda, K. Toko, and T. Suemasu, Impact of radio-frequency power on the photoresponsivity enhancement of $BaSi_2$ films formed by sputtering, Applied Physics Express 13 (2020) 085511

[13] S. Matsuno, R. Takabe, S. Yokoyama, K. Toko, M. Mesuda, H. Kuramochi, and T. Suemasu, Significant photoresponsivity enhancement of polycrystalline $BaSi_2$ films formed on heated Si(111) substrates by sputtering, Applied Physics Express 11 (2018) 071401

[14] K. Kido, R. Koitabashi, T. Ishiyama, H. Hasebe, M. Mesuda, K. Toko, and T. Suemasu, Co-sputtering deposition of high-photoresponsivity and high-mobility polycrystalline $BaSi_2$ films on Si substrates, Thin Solid Films 758 (2022) 139426

[15] T. Suemasu, K. Morita, and M. Kobayashi, Molecular beam epitaxy of band gap tunable ternary semiconducting silicides $Ba_{1-x}Sr_xSi_2$ for photovoltaic application, J. Cryst. Growth 301 (2007) 680

[16] H. Takeuchi, W. Du, M. Baba, R. Takabe, K. Toko, and T. Suemasu, Characterization of defect levels in undoped n-$BaSi_2$ epitaxial films on Si(111) by deep-level transient spectroscopy, Jpn. J. Appl. Phys. 54 (2015) 07JE01

[17] A.R. Mohmad, Z. Xu, Y. Yamashita, and T. Suemasu, Assessing defect-assisted emissions in indirect bandgap $BaSi_2$ by photoluminescence, Journal of Luminescence 252 (2022) 119312

Surface-Enhanced Raman Spectroscopy (SERS) for SARS-CoV-2 Protein Variants

Liyana Shatar[1], Fariza Hanim Suhailin[1,2*]

[1]Department of Physics, Faculty of Science, Universiti Teknologi Malaysia (UTM), 81310 Johor Bahru, Johor Darul Takzim, Malaysia

[2]Laser Center, Ibnu Sina Institute for Scientific & Industrial Research (ISI-SIR), Universiti Teknologi Malaysia (UTM), 81310 Johor Bahru, Johor Darul Takzim, Malaysia

***Corresponding author:** Fariza Hanim Suhailin — farizahanim@utm.my

Abstract

Surface enhanced Raman spectroscopy (SERS) is a promising technique for biomolecule detection. In this work, we analyzed and characterized the Raman vibrational modes from S- and N-proteins of SARS-CoV-2 Wuhan (original) and Omicron variants for advanced viral identification. The SERS substrates were based on gold nanoparticles (Au NPs) embedded on silicon chips. The Au NPs was synthesized via bottom-up method. The Au NPs surface was chemical modified via self-assembled monolayer (SAM) technique by adapting successive functionalization steps of hydroxylation, salinization and amination treating to achieve aptamers (biorecognition elements) immobilization on the substrate. The aptamers were designed to exhibit high affinity, selectivity and specificity towards recombinant S- and N-proteins of SARS-CoV-2 Wuhan and Omicron variants. The hybridization between aptamers to different concentrations of proteins (0.1 aM–20.0 μM) had resulted distinct Raman signatures. The SERS detection responses were characterized into 2 range of concentrations, i.e., low range (0.1 aM–0.1 nM), and high range (1.0 nm–20.0 μM). For low range concentrations, the analysis focused on the Raman spectral changes at 1580 cm−1 peak, of which associated to gold-thiolate (Au-S) interactions. For high range concentrations, the analysis focused into 3 different regions of broad wavenumbers, i.e., fingerprint region (disulfide bonds, glycosylation and aromatic residues), silence region (aromatic residues, amide III, and amide I), and high wavelength region (CH and NH stretching). Overall, across all concentrations, the detection response and sensitivity were correlated to the respective strength of aptamer binding affinity and the structural dynamics of the protein. The Omicrons proteins exhibit higher Raman intensities, sensitivity and dynamics in comparison to Wuhan proteins. These differences could indicate enhanced aptamer-Omicrons proteins interactions, potentially driven by structural mutations that alter its molecular dynamics that may increase the Raman accessibility of specific regions of the protein backbone or side chains. Particularly, these results provide valuable insights into the molecular differences between the proteins of the SARS-CoV-2 variants and their SERS-amplified Raman interactions, allowing detailed proteins characterization and specific detection through distinct spectral signatures. These highlight the potential of SERS in viral identification and COVID-19 disease management.

Keywords: *SERS, SARS-CoV-2, COVID-19, S- and N-proteins, Wuhan and Omicron variants*

Exploring Intra- and Inter-Sheet Variations of White Copies Papers using ATR-FTIR Spectroscopy using Chemometric Techniques for Forensic Investigations

Gurvinder Singh Bumbrah[1], Loong Chuen Lee[2*]

[1]Department of Forensic Science, Amity School of Applied Sciences, Amity University Rajasthan, Jaipur-303002, Rajasthan, India

[2]Forensic Science Program, CODITS, FSK, Universiti Kebangsaan Malaysia (UKM), 43600, Bangi, Selangor, Malaysia

***Corresponding author:** lc_lee@ukm.edu.my

Abstract

This study explores the intra- and inter-sheet variations of four different brands of Indian white copy papers using attenuated total reflectance-Fourier transform infrared (ATR-FTIR) spectroscopy assisted by chemometric methods. Results showed that the intra- and inter-sheet variations of the papers differed across the five brands.

Keywords: *ATR-FTIR spectroscopy, white copy paper, forensic investigations, principal component analysis, hierarchical clustering analysis,*

Introduction

White copy paper is often used for official documents, such as wills and commercial agreements. Hence, discriminating its source origin can contribute to the investigation of civil cases involving forged documents. White copy paper produced by different manufacturers potentially differs in its composition. Therefore, attenuated total reflectance-Fourier transform infrared (ATR-FTIR) spectroscopy can be applied to acquire the compositional fingerprints of the papers. A number of studies have attempted to discriminate paper samples for forensic investigations [1-5]. Recent works have demonstrated that organic profiles acquired via IR spectroscopy are particularly valuable in determining the source origin of white copy papers [3-5]. To build on this, the current work investigates the intra- and inter-sheet variations of five brands of Indian white copy papers ATR-FTIR spectroscopy assisted by principal component analysis (PCA) and hierarchical clustering analysis (HCA). The insights from this work further enhance the understanding of the potential of IR spectroscopy in the forensic examination of forged documents.

Methodology

Ten sheets of white copy paper originating from four different manufacturers were purchased from a local shop in India. Each sheet was divided into 20 distinct spots and analysed using ATR-FTIR spectroscopy (Bruker ALPHA II with a Platinum Diamond ATR). Consequently, a total of 200 IR spectra were collected from the ten sheets of paper. All spectra were recorded in the range of 4000-400 cm-1. Prior to multivariate exploratory analysis, the raw IR spectra were preprocessed using asymmetric least squares (AsLS) followed by normalization to sum (NS) to remove irrelevant variations. The variations of the sheets were assessed via PCA score plots and HCA dendrograms across different IR sub-regions. All statistical analyses were performed using R software.

Results and Discussion

Mean IR spectra (covering 1500-400 cm-1) of the white copy papers indicated relatively low inter-brand variations. Among the five samples, B3 showed a prominent peak at 1400 cm-1, which discriminated it from the remaining brands. With respect to inter-sheet variations, three of the five brands demonstrated a clear difference between their two sheets (namely B1, B2, and B5). Meanwhile,

the remaining brands showed visible overlap between the sheets. In addition, the brands associated with relatively low inter-sheet variation tended to exhibit slightly higher intra-sheet variation. It is worth mentioning that B1 and B3 are from the same manufacturer but have different grammage (GSM). These results indicate that GSM potentially contributes to significant differences in the IR spectrum. Moreover, the magnitude of inter-sheet variations does not seem to be governed by the manufacturer or GSM. Future work should include a larger number of sheets from each brand to further confirm the impacts of brand and GSM on the inter- and intra-sheet variations.

Conclusion

In conclusion, ATR-FTIR spectroscopy coupled with chemometric methods is useful for elucidating the inter-brand and inter-sheet variations of white copy paper. Both PCA score plots and HCA dendrograms can be applied to illustrate the inter- and intra-sheet variations of a brand of white copy paper. These findings highlight the potential of a non-destructive and efficient approach for discriminating white copy paper by individual sheets within a brand.

Acknowledgement

The second author acknowledges the financial support from CRIM, Universiti Kebangsaan Malaysia, through research grant GP-K016373.

References

[1] R. Kumar, V. Kumar, and V. Sharma, "Discrimination of various paper types using diffuse reflectance ultraviolet-visible near-infrared (UV-Vis-NIR) spectroscopy: forensic application to questioned documents," Applied Spectroscopy, vol. 69, no. 6, p. 714, 2015, doi: 10.1366/14-07663.

[2] R. Kumar, et al., "Analysis of writing/printing paper via Thermogravimetric analysis: application in forensic science" Australian Journal of Forensic Sciences, vol. 51, p. 22, 2019, doi: 10.1080/00450618.2017.1310921.

[3] R. Kumar, V. Kumar, and V. Sharma, "Fourier transform infrared spectroscopy and chemometrics for the characterization and discrimination of writing/photocopier paper types: Application in forensic document examinations," Spectrochimica Acta Part A. Molecular and Biomoleculr Spectroscopy, vol. 170, p. 19, 2025, doi: 10.11113/jurnalteknologi.v88.24770.

[4] W.N.S. Mat Desa, T.E. Kam, and D. Ismail, "Non-destructive analysis of white A4 office papers using ATR-FTIR spectrosocpy and chemometric procedures for forenisc application," Jurnal Teknologi, vol. 88, no. 3, p. 507, 2022/02/01/ 2026, doi: 10.11113/jurnalteknologi.v88.24770.

[5] L.C. Lee, "A study to explore discriminative power of attenuated total reflectance-Fourier transform infrarred spectroscpy for forensic paper analysis using decision tree method," Journal of Analytical Chemistry, vol. 76, p. 95, 2021, doi: 10.1134/S1061934821010068.

Porous Structure Development of Coconut Shell-Derived Activated Carbon through Phosphoric Acid Activation

Nurul Huda Abu Bakar[1*], Ahmad Salihin Samsudin[1]

[1]Faculty of Industrial Sciences and Technology, Universiti Malaysia Pahang Al-Sultan Abdullah, Gambang Campus, 26300, Kuantan, Pahang, Malaysia

***Corresponding author:** hudabakar@umpsa.edu.my

Abstract

The present study investigates phosphoric acid activation at carbon-to-acid ratios of 1:1 and 1:2. Coconut shell charcoal served as the inactivated reference. Fourier-transform infrared spectroscopy (FTIR) was used to probe changes in surface chemical characteristics associated with activation, while Brunauer–Emmett–Teller (BET) and t-plot analyses were used to determine how these spectroscopic characteristics corresponded with pore development. FTIR spectra of all samples retained the principal bands near 3450, 1640, 1378 and 561 cm-1, with activation mainly altering band intensity rather than producing major new features. In contrast, pronounced textural changes were observed after activation. BET surface area increased from 148.86 m2 g-1 for coconut charcoal to 720.46 m2 g-1 for 1:1 activated carbon and 962.13 m2 g-1 for 1:2 activated carbon. The corresponding micropore areas were 83.48, 495.80 and 539.93 m2 g-1, while micropore volumes increased from 0.0343 to 0.2286 and 0.2394 cm3 g-1, respectively. The results demonstrate that phosphoric acid activation substantially develops the porous network of coconut shell carbon, with the 1:2 ratio providing the highest overall surface area and a more developed combination of microporous and external surface regions.

Keywords: *FTIR spectroscopy, activated carbon, coconut shell, phosphoric acid activation, porous structure*

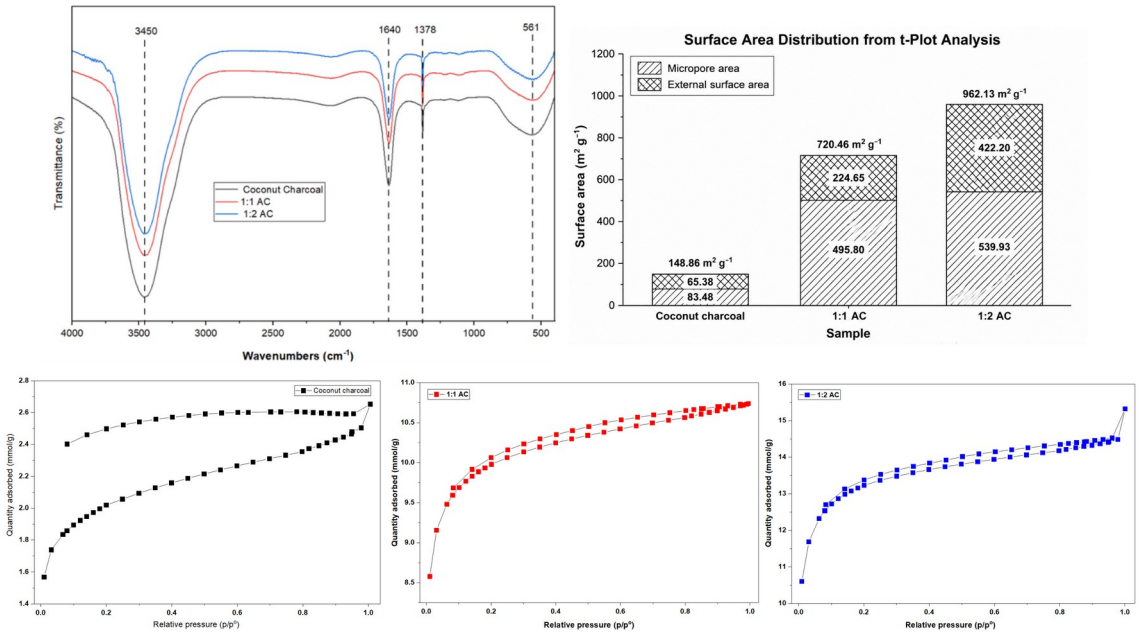

1. Introduction

Activated carbon is an important porous material for adsorption, separation, catalysis and electrochemical energy-storage applications because its performance is strongly governed by accessible surface area and pore architecture [1]. Biomass-derived carbons are particularly attractive because they convert agricultural residues into value-added functional materials. Coconut shell is a suitable carbon precursor owing to its rigid lignocellulosic structure and ability to generate a predominantly

microporous carbon framework after carbonization and activation [2,4]. Chemical activation with phosphoric acid promotes dehydration and structural rearrangement during heat treatment and can suppress excessive tar formation, thereby facilitating pore opening and widening. Previous studies on coconut shell and other lignocellulosic precursors show that impregnation ratio is an important parameter controlling surface area, micropore development and pore-size distribution [5]. The present study therefore compares inactivated coconut charcoal with activated carbons prepared at 1:1 and 1:2 carbon-to-phosphoric acid ratios. Particular emphasis was placed on relating FTIR-observed surface chemical characteristics to quantitative changes in porosity obtained from nitrogen adsorption, BET and t-plot analyses. This combined spectroscopic-textural approach was used to determine whether substantial pore development requires correspondingly large changes in the major FTIR-detectable functional groups.

2. Methodology

Coconut shells were collected from the local market in Kuantan, Pahang. Approximately 2 kg of the shells were cleaned, dried, ground and carbonized at 500 °C for 1 h to produce coconut charcoal. The carbonized material was sieved to ~100 μm before chemical activation. A 50% phosphoric acid solution (ACS reagent-grade 85%, Sigma-Aldrich) was mixed with the charcoal at carbon-to-acid mass ratios of 1:1 and 1:2. The impregnated samples were soaked, dried and thermally activated at 600 °C for 1 h using a heating rate of 5 °C min^{-1}. The products were repeatedly washed with deionized water until approximately neutral pH was reached and then dried. Coconut charcoal, 1:1 activated carbon (1:1 AC) and 1:2 activated carbon (1:2 AC) were characterized by FTIR spectroscopy (model PERKIN ALMER) through the (KBr) method in the frequency range of 400–4000 cm-1 with a resolution of 4 cm-1. Nitrogen adsorption-desorption measurements (Micromeritics Model: ASAP2020) were conducted subsequently to quantify textural development through BET specific surface area, while t-plot analysis provided micropore area, micropore volume and external surface area. The spectroscopic trends were then interpreted alongside these textural parameters rather than as standalone evidence of pore formation.

3. Results and Discussion

The FTIR spectra show broadly similar profiles for coconut charcoal and both activated carbons. A broad absorption region centered near 3450 cm^{-1} is assigned mainly to O–H stretching associated with surface hydroxyl groups and adsorbed moisture. The band near 1640 cm^{-1} can be associated with aromatic C=C vibrations and/or conjugated oxygen-containing structures, while the feature around 1378 cm^{-1} is consistent with C–H deformation and oxygen-containing surface functionalities. A low-wavenumber feature is observed near 561 cm^{-1} which associated to skeletal/deformation vibrations of the carbonaceous structure. No strong new bands emerge after activation where the principal differences are changes in the relative intensity. This spectral similarity is itself significant; despite the large increase in accessible surface area after activation, the major FTIR-detectable functional-group profile remains broadly preserved. Thus, FTIR and adsorption analyses together indicate that phosphoric acid treatment primarily restructures the carbon pore network under the present conditions rather than producing a wholesale change in the dominant detectable surface functionalities. Phosphoric acid-activated carbons have likewise been reported to retain oxygen- and phosphorus-associated surface species while undergoing strong pore development [6].

Meanwhile, nitrogen adsorption–desorption behavior changed markedly following activation. All samples show rapid adsorption at low relative pressure, consistent with an important micropore contribution. The activated samples adsorbed substantially more nitrogen than coconut charcoal over the measured pressure range. The 1:2 AC showed the greatest overall adsorption and a more pronounced rise near $p/p^{\circ} = 1$, indicating that increasing acid loading developed not only microporosity but also additional external surface and larger pore regions. This agrees with earlier reports that phosphoric acid activation can generate wider micropores and mesoporosity in coconut-shell carbons [6].

Quantitative textural parameters confirm progressive pore development where coconut charcoal had a BET surface area of 148.86 m2 g-1. Activation at 1:1 increased this value to 720.46 m2 g-1, approximately 384% higher than the charcoal, while 1:2 AC reached 962.13 m2 g-1, approximately 546% above the inactivated reference and 33.5% above 1:1 AC. The t-plot micropore area increased from 83.48 m2 g-1 to 495.80 and 539.93 m2 g-1 for 1:1 and 1:2 AC, respectively. Micropore volume similarly increased from 0.0343 cm3 g-1 to 0.2286 and 0.2394 cm3 g-1. The external surface area provides a particularly useful distinction between the two activation ratios. It increased from 65.38 m2 g-1 for coconut charcoal to 224.65 m2 g-1 at 1:1 and 422.20 $m^2\ g^{-1}$ at 1:2. In contrast, the micropore area increased more modestly between the activated samples, from 495.80 to 539.93 m2 g-1. Consequently, micropore area accounted for approximately 68.8% of the BET area of 1:1 AC but 56.1% of 1:2 AC. The higher acid ratio therefore appears to continue micropore formation while producing substantial pore opening or widening that increases external/non-microporous surface.

4. Conclusion

Phosphoric acid activation substantially enhanced the porous structure of coconut shell-derived carbon. BET surface area increases confirming effective micropore generation. The 1:2 ratio produced the highest BET area, micropore area and external surface area, indicating the most developed overall pore network. FTIR spectra showed only modest differences among samples even though BET and t-plot parameters changed markedly. The combined results therefore show that substantial pore-network development can occur while the major FTIR-detectable surface functionalities remain broadly similar. The 1:2 condition is therefore the more promising of the investigated ratios for producing high-surface-area coconut shell-derived activated carbon for subsequent adsorption or electrochemical evaluation.

Acknowledgement

The authors gratefully acknowledge the Faculty of Industrial Sciences and Technology, Universiti Malaysia Pahang Al-Sultan Abdullah (UMPSA) for providing the laboratory facilities and research support that facilitated the successful completion of this study.

References

[1] Heryanto, H., Tahir, D., Abdullah, B., Kavgaci, M., Rinovian, A., Masrour, R., ... & Sayyed, M. I. (2024). Carbon as a multifunctional material in supporting adsorption performance for water treatment: Science mapping and review. Desalination and Water Treatment, 320, 100758. https://doi.org/10.1016/j.dwt.2024.100758

[2] Purohit, S. K., Bandyopadhyay, S., Choi, H., & Nayak, A. K. (2026). Advances in Synthesis and Applications of Waste-Derived Activated Porous Carbon: A Review for Energy Storage and Environmental Remediation. ChemistrySelect, 11(18), e73398. https://doi.org/10.1002/slct.73398

[3] Achaw, O. W., & Afrane, G. (2008). The evolution of the pore structure of coconut shells during the preparation of coconut shell-based activated carbons. Microporous and mesoporous materials, 112(1-3), 284-290. 10.1016/j.micromeso.2007.10.001

[4] Cachola Maldito Lowden, V. M., Alexandre-Franco, M. F., Garrido-Zoido, J. M., Cuerda-Correa, E. M., & Gómez-Serrano, V. (2026). Coconut shell-derived activated carbons: preparation, physicochemical properties, and dye removal from water. Molecules, 31(2), 263. https://doi.org/10.3390/molecules31020263

[5] Sych, N. V., Trofymenko, S. I., Poddubnaya, O. I., Tsyba, M. M., Sapsay, V. I., Klymchuk, D. O., & Puziy, A. M. (2012). Porous structure and surface chemistry of phosphoric acid activated carbon from corncob. Applied surface science, 261, 75-82. 10.1016/j.apsusc.2012.07.084

[6] Sujiono, E. H., Zabrian, D., Zharvan, V., & Humairah, N. A. (2022). Fabrication and characterization of coconut shell activated carbon using variation chemical activation for wastewater treatment application. Results in Chemistry, 4, 100291. https://doi.org/10.1016/j.rechem.2022.100291

Influence of Reference pH Measurement and Spectral Region on VIS-NIR Spectroscopy Calibration for Non-Destructive pH Prediction of Harumanis Mango

Mas Ira Syafila Mohd Hilmi Tan[1], Ahmad Fairuz Omar[2*]

[1]School of Artificial Intelligence and Robotics, Xiamen University Malaysia, 43900 Sepang, Selangor, Malaysia

[2]School of Physics, Universiti Sains Malaysia, 11800 USM, Penang, Malaysia

***Corresponding author:** fairuz_omar@usm.my

Abstract

This study investigates the influence of reference pH measurement and spectral region selection on VIS-NIR spectroscopy calibration for non-destructive pH prediction of Harumanis mango (Mangifera indica L.). VIS-NIR spectra with wavelength range of 350–1131 nm were collected from 53 Harumanis mangoes. Reference pH values were obtained using a juice-based Atago pH meter for the front and back sections, while a probe-based SmartSensor pH meter was used to measure six locations (top, middle, and lower regions on both fruit surfaces). Correlation and Bland-Altman analyses were performed to characterise the relationship between the two reference measurements, while the Friedman test was used to evaluate pH variation across six fruit measurement locations. The Friedman test indicated no significant differences among the six SmartSensor measurement locations ($p = 0.9487$), supporting the use of averaged measurements for calibration development. The overall Atego and SmartSensor measurements showed a strong correlation ($r = 0.9563$), but paired analysis indicated a significant difference between the two reference measurements ($p = 7.328 \times 10^{-28}$), with a Bland-Altman bias of 0.7346 pH units. Several spectral preprocessing techniques, including raw spectra, standard normal variate (SNV), multiplicative scatter correction (MSC), Savitzky-Golay filtering, and first derivative transformation, were evaluated using PLSR as the baseline model. MSC was selected as the preprocessing approach for subsequent calibration model comparison. Several regression models were compared including partial least squares regression (PLSR), Ridge, support vector regression (SVR), Random Forest (RF), Extreme Gradient Boosting (XGBoost), and partial least squares–Gaussian process regression (PLS-GPR) using the selected preprocessing approach. PLS-GPR provided the optimal calibration performance using the Atego reference ($R^2 = 0.912$, RMSE = 0.242, MAE = 0.172, and RPD = 3.401), while calibration using the SmartSensor reference achieved its best performance with Ridge regression ($R^2 = 0.808$, RMSE = 0.324, MAE = 0.241, and RPD = 2.304). These results demonstrate that differences in reference pH measurement can influence VIS-NIR calibration performance, even when the reference measurements are strongly correlated. These findings can be used as practical guidance for developing more reliable VIS-NIR calibration models for non-destructive pH prediction of Harumanis mango.

Keywords: *Harumanis, Mango, VIS-NIR, pH prediction, Non-destructive quality assessment, Chemometrics*

Introduction

Harumanis Mango (Mangifera indica L.) is a local variety of mango that is widely cultivated in Perlis, Malaysia. pH is an important indicator of acidity and contributes to flavour, ripening behaviour, and postharvest quality of the mango. Conventional pH determination requires destructive sampling of fruit tissue or juice, which limits its use for rapid, non-destructive quality assessment. VIS-NIR spectroscopy provides a rapid and non-destructive means of acquiring spectral information from intact fruit and, when combined with chemometric calibration, can be used to estimate internal quality attributes . For calibration, the spectral data must be linked to a reference value. The reference measurement is an important part of the calibration process . Different measurement methods may not give the same pH value because they sample the fruit differently. A juice-based measurement

represents homogenised fruit material, whereas a probe measures pH at a local position. This study compares these two reference approaches and examines their effect on VIS-NIR calibration performance for non-destructive pH prediction of Harumanis mango.

Methodology

53 Harumanis mangoes were measured using a VIS-NIR spectrometer. Spectra were collected from each mangoes at six positions: top, middle, and lower positions on the front surface and the same three positions on the back surface. The acquired spectral range was 350–1131 nm. For the calibration analysis, wavelengths from 400–1100 nm were retained. The six spectral measurements were averaged to obtain one representative spectrum for each mango. Two reference pH measurement methods were used. For the Atago method, mango juice was measured from the front and back sections. For the SmartSensor method, the probe was used at the same six positions as the spectral measurements. The six SmartSensor locations were first evaluated using the Friedman test to determine whether the measured pH differed by position. The relationship between the Atago and SmartSensor reference values was then examined using Pearson correlation and Bland-Altman analysis. For spectral preprocessing, raw spectra, Savitzky-Golay smoothing, SNV, MSC, and first derivative were tested. PLSR was used as the baseline model for selecting the preprocessing method. MSC was selected and then fixed for the comparison of calibration models. The models evaluated were PLSR, Ridge, SVR, RF, XGBoost, and PLS-GPR. A 10-fold cross-validation with shuffling was used for model evaluation. Performance was assessed using R^2, RMSE, MAE, and RPD. PLS-GPR was selected as the best-performing regression approach based on its prediction performance. As an additional analysis, the selected PLS-GPR model was used to compare the prediction performance of VIS, NIR, and combined VIS–NIR spectra.

Results and Discussion

The SmartSensor pH measurements did not differ significantly among the six measurement positions (Friedman test, $p = 0.9487$). This result supports averaging the six probe measurements to obtain one SmartSensor reference value for each mango. The comparison between the two reference methods gave a Pearson correlation coefficient of 0.9563, showing that both methods followed a similar pH trend. However, the Bland-Altman analysis showed a positive bias of 0.7346 pH units. Thus, a strong correlation did not mean that the two methods produced the same reference values.

The preprocessing comparison was carried out using PLSR as the baseline model. MSC gave the highest R^2 and RPD and the lowest RMSE among the tested preprocessing methods, with $R^2 = 0.895$, RMSE = 0.265, and RPD = 3.113. MSC was therefore selected and used for all subsequent calibration models. Using the same MSC-preprocessed spectra, the best model for the Atego reference was PLS-GPR, which achieved $R^2 = 0.912$, RMSE = 0.242, MAE = 0.172, and RPD = 3.401. For the SmartSensor reference, Ridge gave the best result, with $R^2 = 0.808$, RMSE = 0.324, MAE = 0.241, and RPD = 2.304. The difference in model performance between the two reference methods suggests that the reference pH value affects the calibration target. The Atego method measures juice after the fruit material has been sampled and homogenised, whereas the SmartSensor measures pH at local positions. Even though the two reference measurements were strongly correlated, their systematic difference was large enough to produce different calibration results. Therefore, the reference measurement method needs to be considered when developing and comparing VIS-NIR pH calibration models.

As an additional analysis, the PLS-GPR model was applied using the Atego reference to the VIS (400–780 nm), NIR (780–1100 nm), and combined VIS–NIR (400–1100 nm) regions separately. The results showed R^2 values of 0.820, 0.843, and 0.912 for VIS, NIR, and VIS–NIR, respectively. The combined VIS–NIR region provided the best prediction performance, suggesting that information from both spectral regions contributes to pH prediction.

Conclusion

This study shows that the reference pH measurement method can affect VIS-NIR calibration performance for Harumanis mango. The six SmartSensor measurement positions did not show a significant difference in pH, allowing the measurements to be averaged. In contrast, the Atago and SmartSensor reference values showed a strong correlation but also a systematic difference. Using PLSR as the baseline, MSC was selected as the preprocessing method and was applied to all subsequent calibration models. PLS-GPR gave the best result for the Atago reference, while Ridge gave the best result for the SmartSensor reference. For the Atago reference, the combined VIS–NIR region also provided the best prediction performance (R^2 = 0.912) compared with the individual VIS and NIR regions when evaluated using PLS-GPR. These results show that the reference measurement is not only a source of target data but can also affect the calibration performance obtained from the same VIS-NIR spectra. The reference measurement method should therefore be defined clearly when developing VIS-NIR calibration models for non-destructive pH prediction.

Acknowledgement (Optional)

The authors gratefully acknowledge the financial support provided by Xiamen University Malaysia Research Fund (Grant No. XMUMRF/2026-C18/IECE/0084), which facilitated the successful completion of this research.

Deep Eutectic Solvent with Azo-Imine Additive for Dual Application Dye-Adsorbent and Polymer Electrolyte

Rafizah Rahamathullah[1,2*], Koshini A/P Sughendran, Siti Khalijah Mahmad Rozi[1,2]

[1]Faculty of Chemical Engineering & Technology, Universiti Malaysia Perlis, Kompleks Pusat Pengajian Jejawi, 02600 Arau, Perlis, Malaysia

[2]Centre of Excellence for Biomass Utilization, Universiti Malaysia Perlis (UniMAP), Perlis, Malaysia

***Corresponding author:** Rafizah Rahamathullah — fizah@unimap.edu.my

Abstract

This study investigates the effect of thymol–menthol deep eutectic solvents (T:M DES) with azo-imine (AI) additive featuring hybrid (-N=N-) and (-CH=N-) groups for dye-adsorbent and polymer electrolyte performance. Prior to incorporation into the polymer-based matrix, the physical and spectroscopic properties of the synthesized T:M DES and AI additives were investigated using density, surface tension analysis, FTIR, UV-Vis and NMR. FTIR analysis confirmed the successful incorporation of additive into the polymer matrix through broadening and shifting of the hydroxyl (–OH) stretching band, indicating strong hydrogen bonding interactions between additive and polymer-based matrix. From UV-Vis and optical energy gap (Egopt) obtained indicate nitrogen (N) and oxygen (O) atoms from azo and imine substituents tuning the energy level by reducing the HOMO-LUMO gap to 2.17eV. The ionic conductivity of electrolyte also increased two orders of magnitude from 1.66×10^{-9} S/cm to 1.46×10^{-7} S/cm. The adsorption study showed removal efficiencies of 96.3% for Rhodamine B (RB) under optimum conditions, such as contact time (15 minutes), temperature (45°C), and pH of 8.

Keywords: *Deep Eutectic Solvents; Azo-Imine; Additive; Conductivity; Dye Removal*

1. Introduction

Multifunctional materials are increasingly important in addressing today's environmental issues and energy demands. As the world faces rising levels of pollution, water contamination, and energy shortages, these materials offer integrated solutions that promote sustainability and efficiency [1]. Organic compounds have attracted significant attention as multifunctional materials due to their versatile chemical structures and tunable properties. Composed mainly of carbon along with elements such as nitrogen (N), oxygen (O), and sulfur (S), these compounds can be engineered with functional groups that introduce polarity, electron-rich sites [2], good porosity, and hydrogen bonding capabilities [3]. Such features not only enhance chemical reactivity but also enable strong interactions with other materials or pollutants. For instance, delocalized π-electron systems commonly found in conjugated organic structures facilitate efficient charge mobility, making them ideal for electrochemical devices.

Besides organic compounds, deep eutectic solvents (DES) are considered one of the most prominent examples of multifunctional materials [4], not only because of their favorable physical properties but also due to their unique structural characteristics. Their good ionic conductivity arises from efficient ion transport within a hydrogen-bonded network, while their low toxicity, low vapor pressure, and non-flammability make them environmentally friendly and safe for various applications [5]. In line with this study, the utilization of multifunctional materials, organic compounds and DES are aimed at enhancing the overall performance of both dye adsorption and electrochemical systems.

For both of these applications, polymer-based media are commonly used. In dye adsorption, melamine sponges have gained attention as practical adsorbent, while in polymer electrolytes, polyethylene oxide (PEO) is commonly used as the polymer matrix. However, both of these media possess limited functional groups and active sites, which can restrict their overall selectivity and conductivity, respectively. Therefore, this presence study utilizes the hybrid combination of AI and T:M DES (AI@T:M DES) as a new additive to modify the sponge for dye adsorption and the PEO matrix for dual applications.

2. Methodology

Prior to synthesized AI additive, precursors, namely 2-hydroxy-5-((4-nitrophenyl) diazenyl) benzaldehyde (1), N-4-hexyloxyphenyl acetamide (2), and N-4-hexyloxy aniline (3) has been synthesized as reported in previous studies [Menati et al., 2013)]. Then, precursor 1 was reacted with 3 to obtain the targeted AI additive. While, thymol and menthol based deep eutectic solvent (T:M DESs) were heated at 60 °C with constant stirring until a clear liquid formed. For dye adsorption application, polymer-based sponge is embedded with AI@T:M DES additive. Various parameters (contact time, temperature, and pH of solution) were investigated throughout Rhodamine B (RB) dye adsorption process. While, for polymer electrolyte, polyethylene oxide (PEO) was incorporated AI@T:M DES additive for the PEO-based solid polymer electrolyte (SPE) forming, AI@TM-PEO then the film characterized through FTIR, XRD, and Electrical Impedance Spectroscopy (EIS).

3. Results and Discussion

All the synthesized compounds were then successfully analysed via spectroscopic technique namely FTIR, UV-Vis, 1H and 13C Nuclear Magnetic Resonance (NMR) as well employed for the photophysical studies and band gap measurements. Based on the results obtained from structural elucidation, the findings revealed the confirmation of molecular structure of all precursors (1, 2, 3) and targeted AI additive.

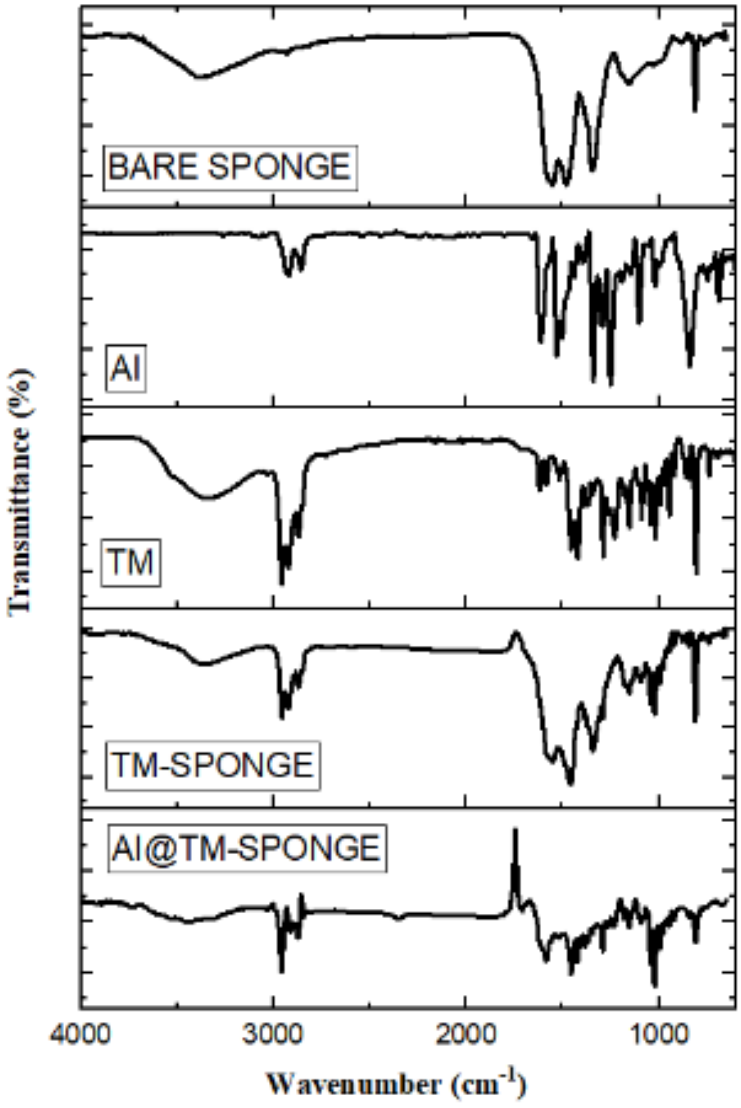

FTIR analysis confirmed the successful synthesis of the AI additive through the appearance of the characteristic imine ν(C=N) stretching band at 1612 cm^{-1} and the disappearance of the aldehyde ν(C=O) band at 1659 cm^{-1} and amine ν(N–H) band at 3258 cm^{-1}. The absorption bands at 1503 and 1440 cm^{-1} further confirmed the formation of the azo (N=N) functional group, verifying the proposed molecular structure of the synthesized AI additive. The UV–Vis spectrum of the azo-imine additive exhibited two characteristic absorption bands at 280 nm and 365 nm, corresponding to the π–π* and mixed n–π* and π–π* electronic transitions, respectively. The absorption band at 365 nm indicates the presence of an extended π-conjugated system involving the azo (N=N) and imine (C=N) functional groups. The ^{1}H NMR spectrum of the AI additive exhibited the characteristic imine proton (CH=N) signal at δH 8.06 ppm, together with the expected aliphatic, aromatic, and hydroxyl proton signals. The disappearance of the aldehyde proton and the appearance of the imine proton confirmed the successful formation of the Schiff base structure. The ^{13}C NMR spectrum of the AI additive exhibited the characteristic imine carbon (CH=N) resonance at δC 139.77 ppm, together with the expected aliphatic and aromatic carbon signals.

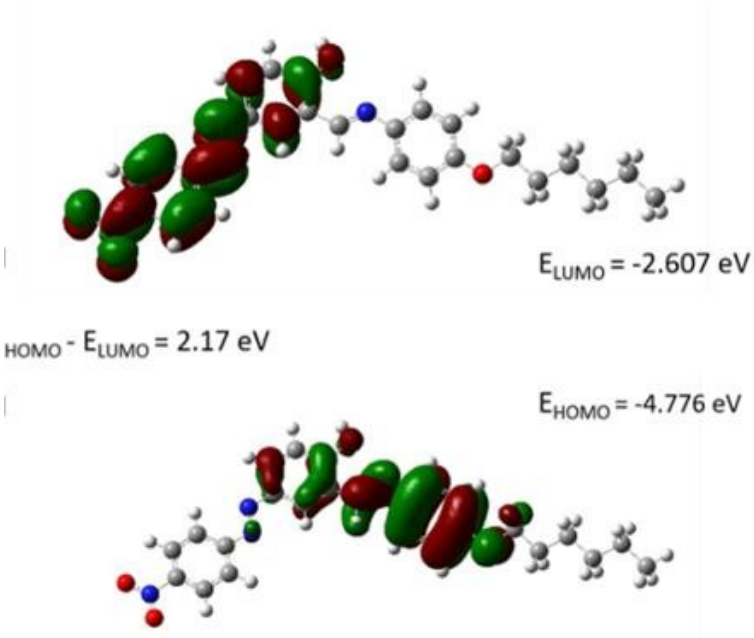

FTIR analysis of the thymol and menthol based deep eutectic solvent (T:M DESs) exhibited characteristic absorption bands at 3357 cm^{-1} (ν(O–H)), 2960 cm^{-1} (ν(C–H)), 1448 cm^{-1} (ν(C=C)), and 1289 cm^{-1} (ν(C–O)). The broadening and slight shift of the hydroxyl band confirmed hydrogen-bonding interactions between thymol and menthol, indicating the successful formation of the T:M DES. SEM analysis of the developed sponge confirmed significant morphological changes after incorporation of the additives, where the sponge surface became rougher and more irregular with visible aggregated deposits of the additives on the sponge skeleton. Despite these surface modifications, the interconnected porous structure of the melamine sponge remained intact, indicating successful loading of additives without structural collapse and suggesting improved active sites for dye adsorption. The developed sponge achieved Rhodamine B removal efficiency of 89.54%, indicating enhanced adsorption performance. This improvement is attributed to the increased availability of functional groups and active sites from both the additives, which promote stronger dye–adsorbent interactions through π–π interactions, hydrogen bonding, and hydrophobic effects. Additionally, the increased surface roughness and porosity of the modified sponge further facilitated dye diffusion and adsorption within the porous structure. The developed sponge exhibited optimal Rhodamine B adsorption performance under the following conditions: a contact time of 15 min, a temperature of 45 °C, and an initial solution pH of 8,

indicating that the adsorption process is largely pH-independent within this range. For polymer electrolyte application, the ionic conductivity of SPEs system has been successfully evaluated using Electrical Impedance Spectroscopy (EIS) and shows an increment in the order of 10-9 S/cm to 10-7 S/cm.

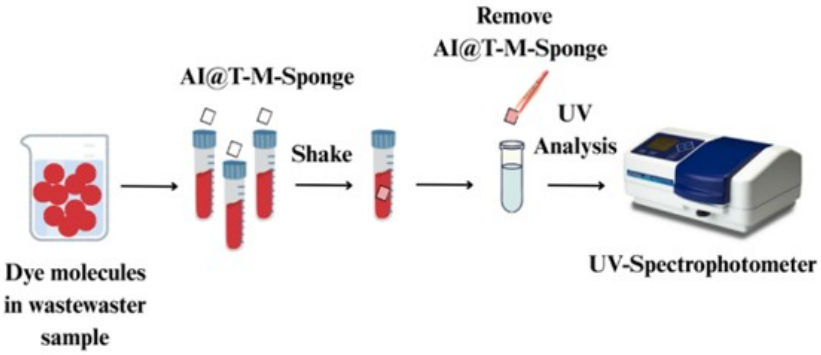

4. Conclusion

The role and performance of T:M DES with AI additive has been successfully evaluated in dual applications of dye adsorption and polymer electrolyte. The preliminary input from this work creates an alternative approach to initiate further investigation on new, efficient, good stability and can performed at an optimum level for future additives materials towards diverse application.

Acknowledgements

We would like to acknowledge the research grant support from Ministry of Higher Education, Malaysia for Fundamental Research Grant Scheme, FRGS/1/2021/STG05/UNIMAP/03/1 (9003-00914) and Faculty of Chemical engineering & Technology, Universiti Malaysia Perlis for facilities and research aids.

References

[1] Y. Zhang, Y. Wan, Y. Zheng, Y. Yang, and B. Gao, "Hydrochar Loaded with Nitrogen-Containing Functional Groups for Versatile Removal of Cationic and Anionic Dyes and Aqueous Heavy Metals," Water, vol. 16, no. 23, p. 3387, 2024, doi: https://doi.org/10.3390/w16233387

[2] Q. He, S. Huang, H. Li, and T. Li, "Electron-rich active sites created by fine-tuning the electronic structure of Co(II) porphyrin frameworks for high-performance CO_2 electroreduction," International Journal of Hydrogen Energy, vol. 51, pp. 1347–1356, 2024, doi: https://doi.org/10.1016/j.ijhydene.2023.11.096

[3] R. Lin and B. Chen, "Hydrogen-bonded organic frameworks: Chemistry and functions," Chem, vol. 8, no. 8, pp. 2114–2135, 2022, doi: https://doi.org/10.1016/j.chempr.2022.06.015

[4] X. Ge, C. Gu, X. Wang, and J. Tu, "Deep eutectic solvents (DESs)-derived advanced functional materials for energy and environmental applications: Challenges, opportunities, and future vision," Journal of Materials Chemistry A, vol. 5, no. 18, pp. 8209–8229, 2017, doi: https://doi.org/10.1039/C7TA01659J

[5] D. O. Abranches and J. A. Coutinho, "Everything You Wanted to Know about Deep Eutectic Solvents but Were Afraid to Be Told," Annual Review of Chemical and Biomolecular Engineering, vol. 14, no. 1, pp. 141–163, 2023, doi: https://doi.org/10.1146/annurev-chembioeng-101121-085323

[6] S. Menati, A. Azadbakht, R. Azadbakht, A. Taeb, and A. Kakanejadifard, "Synthesis, characterization, and electrochemical study of some novel, azo-containing Schiff bases and their Ni(II) complexes," Dye. Pigment., vol. 98, no. 3, pp. 499–506, 2013, doi: https://doi.org/10.1016/j.dyepig.2013.04.009

GaN Photonics for the Future of High-Performance Optical Devices

Mundzir Abdullah[1*], Sabah M. Mohammad[1*]

[1]Institute of Nano Optoelectronics Research and Technology (INOR), Universiti Sains Malaysia, 11800 USM, Penang, Malaysia

***Corresponding author:** mundzir@usm.my, sabah@usm.my

Abstract

Gallium Nitride (GaN) photonics offers a versatile, wide-bandgap material platform for high-performance photonic integrated circuits (PICs), enabling monolithic integration across the ultraviolet to visible spectrum. This work explores four key functional aspects of GaN photonics: (1) Active-passive integrated photonic components, including $Al_xGa_{1-x}N$ straight/curved waveguides, nanograting edge/vertical couplers, tunable multimode interference (MMI) power splitters, high-Q microring resonators (10^4–10^5), and low-voltage electro-optic Mach-Zehnder modulators utilizing the Pockels effect; (2) GaN light sources, featuring quasi-bound states in the continuum (quasi-BIC) asymmetric nanopillar arrays for UV chiral lasing, focused ion beam localized single-photon emitters, and high-reflectance nanoporous GaN distributed Bragg reflectors; (3) GaN third optical nonlinearity ($\chi^{(3)}$), demonstrating strong optical limiting and all-optical switching in pristine GaN films, GaN nanocrystals, and InGaN/GaN multiple quantum wells with ($\chi^{(3)}$) values reaching up to 5.8 x 10^{-5} esu; and (4) GaN photodetectors integrated with plasmonics to enable complete potential of on-chip detection. Together, these results highlight the potential of III-nitride photonic platforms to overcome traditional material limitations and drive advances in optical communication, sensing, and quantum technologies.

Keywords: *Gallium Nitride (GaN); Photonic Integrated Circuits (PICs); Micro-ring resonators; Electro-optic modulation; Quantum photonics*

Introduction

Gallium Nitride (GaN) photonics offers a promising wide-bandgap material platform for high-performance optical devices and photonic integrated circuits (PICs). Existing photonics platforms encounter limitations, such as lack of monolithic light sources in silicon photonics (SiPh), limited active-passive integration yields in indium phosphide (InP), or CMOS incompatibility in thin-film lithium niobate (TFLN). In contrast, GaN features a direct bandgap spanning the UV to visible range, strong electro-optic effects, and excellent CMOS compatibility as the second most manufactured semiconductor [1]. Despite these advantages, challenges such as material defect density, thermal fluctuations, and specialized fabrication remain areas of active research. While passive silicon nitride platforms cater to low-loss light routing, GaN allows monolithic integration of both active and passive photonic functions on a single platform. This creates a compelling need for robust designs across active-passive components, integrated light sources, nonlinear processes, and detection mechanisms to realize next-generation GaN photonic integrated circuits.

Methodology

Active-passive components, including straight/curved waveguides, nanograting couplers, symmetric and asymmetric multimode interference (MMI) splitters, microring resonators (MRRs), and Mach-Zehnder electro-optic (EO) modulators based on $Al_xGa_{1-x}N$, were modeled using Finite-Difference Time-Domain (FDTD) and finite element optical simulations to optimize coupling efficiency, splitting ratios, and Pockels-effect modulation. For GaN light sources, asymmetric nanopillar arrays on sapphire substrates were evaluated to form UV chiral lasers operating via quasi-bound states in the continuum (quasi-BIC), and Ga^+ focused ion beam (FIB) processes were utilized to localize single-

photon emitters alongside porous photo-electrochemical (PEC) etch processes for nanoporous GaN/GaN distributed Bragg reflectors (DBRs). Third-order optical nonlinearities ($\chi^{(3)}$) were investigated in pristine GaN films, GaN nanocrystals, and InGaN/GaN multiple quantum wells (MQWs) under continuous-wave (CW) and femtosecond laser excitation. Finally, fabrication of plasmonic GaN-based photodetectors was integrated to complete the photonic circuit architecture.

Results and Discussion

Edge coupling in $Al_xGa_{1-x}N$ straight and circular bended waveguides demonstrated low mode propagation loss, while nanograting couplers provided efficient vertical light-chip coupling at visible wavelengths. Asymmetric MMI power splitters successfully achieved configurable splitting ratios (including 80:20, 95:5, and 60:40). $Al_xGa_{1-x}N$ microring resonators achieved a Q factor 10^5 with a broad resonance tuning range of 73.59 nm (676 nm to 750 nm. Additionally, directional coupler Mach–Zehnder electro-optic modulators leveraging the $Al_xGa_{1-x}N$ Pockels effect exhibited precise intensity modulation depending on Al composition.

Asymmetric GaN nanopillar arrays on sapphire substrates operating via quasi-bound states in the continuum (quasi-BIC) enabled robust UV chiral lasing at 367.29 nm, attaining a high Q-factor and a degree of circular polarization (DOCP) exceeding 0.99 [2]. Ga^+ focused ion beam (FIB) irradiation and post-annealing successfully localized single-photon emitters in GaN across the 600–800 nm spectrum [3]. Furthermore, photo-electrochemical (PEC) porosification of GaN/n-GaN multilayers formed nanoporous GaN distributed Bragg reflectors (DBRs) with optimized pore-size distributions and doping profiles, achieving peak stopband reflectance exceeding 90–93% in the visible range.

Wavelength-dependent dispersion evaluations of pristine GaN revealed negative and positive nonlinear refractive index, n2 regimes suitable for all-optical switching [4]. Investigation of InGaN/GaN MQWs showed that increasing the quantum well count to 15 periods enhanced the under-femtosecond laser excitation and continuous-wave (CW) laser excitation [5]. Monolithically integrated GaN photodetectors completed the active sensing and readout chain within the photonic integrated circuit architecture. These detectors provided high-responsivity photodetection across the UV and visible bands, enabling full on-chip conversion of routed and modulated optical signals into electrical outputs.

4. Conclusion

We demonstrated the multifunctional capability of GaN photonics across active-passive components, integrated light sources, third-order optical nonlinearities, and photodetectors. The successful design of high-Q microring resonators, low-voltage MZI modulators, high-purity UV chiral lasers, single-photon emitters, and enhanced ($\chi^{(3)}$) quantum well structures confirm GaN as a versatile material platform for integrated optoelectronics. These findings highlight the potential of monolithic III-nitride photonic integrated circuits to overcome traditional limits in silicon and III-V platforms. However, fabrication tolerances and material defect management present ongoing challenges for scalable manufacturing. Future work should focus on complete on-chip co-integration of light sources, modulators, nonlinear nodes, and photodetectors alongside foundry-level process optimization to accelerate deployment in communication, optical computing, and quantum technologies.

Acknowledgement

This work was supported by the Ministry of Higher Education Malaysia through the Higher Institution Centre of Excellence, Institute of Nano Optoelectronics Research and Technology (HICoE-INOR) Program under account code: A305-KR-AKH002-0000000170-K134.

References

[1] M. Ramzan et al., "Recent advances in micro and nanostructured GaN based photonics technology," Optics & Laser Technology, Volume 192, Part B, 113589.

[2] MH Chen et al., "Ultraviolet Chiral Lasing in In-Plane Photonic Crystal via Quasi-Bound State in the Continuum," Nano Letters, Volume 25, 24, 9809-9816, https://doi.org/10.1021/acs.nanolett.5c02216.

[3] YC Tseng et al., "Spatial control of single-photon emitters in gallium nitride via dose-engineered focused ion beam processing," Applied Physics Letters, Volume 128, 26, https://doi.org/10.1063/5.0334735.

[4] MAA Bakar et al., "Correlation of quantum well periods on the 3rd order nonlinear optical responses of InGaN/GaN heterostructures," Journal of Alloys and Compounds, Volume 993, 174630.

[5] MAA Bakar et al., "Spatial control of single-photon emitters in gallium nitride via dose-engineered focused ion beam processing," Applied Physics Letters, Volume 128, 26.

Hybrid Plasmonic–Semiconductor Architectures for Enhanced Near-Infrared Photodetection

Sabah M. Mohammad[1*], Mundzir Abdullah[1]

[1]Institute of Nano Optoelectronics Research and Technology (INOR), Universiti Sains Malaysia, USM, Penang, 11800, Malaysia

***Corresponding author:** sabah@usm.my

Abstract

Broadband photodetectors operating across the ultraviolet–visible–near infrared (UV–Vis–NIR) regions have attracted significant interest for applications in spectroscopy, imaging, optical communication, sensing, and environmental monitoring. However, achieving broad spectral response, high sensitivity, and fast response remains challenging. Plasmonic–semiconductor hybrid architectures offer a promising strategy by enhancing light–matter interaction through localized surface plasmon resonance, near-field enhancement, light scattering, and light trapping. This work reviews hybrid photodetectors incorporating metallic plasmonic nanoparticles, such as gold (Au), silver (Ag), platinum (Pt), and their combinations, with semiconductor nanostructures, porous silicon, metal oxides, III-nitride materials, and conductive polymers such as PEDOT:PSS and PANI. The review emphasizes the role of plasmonic–semiconductor and organic–inorganic interactions in enhancing optical absorption and photocarrier generation. This study demonstrates improved photocurrent, responsivity, detectivity, and spectral response, highlighting the potential of these hybrid architectures for broadband UV–Vis–NIR photodetection and advanced spectroscopic applications.

Keywords: *Broadband photodetector, Plasmonic nanoparticles, hybrid architectures, UV–Vis–NIR/NIR*

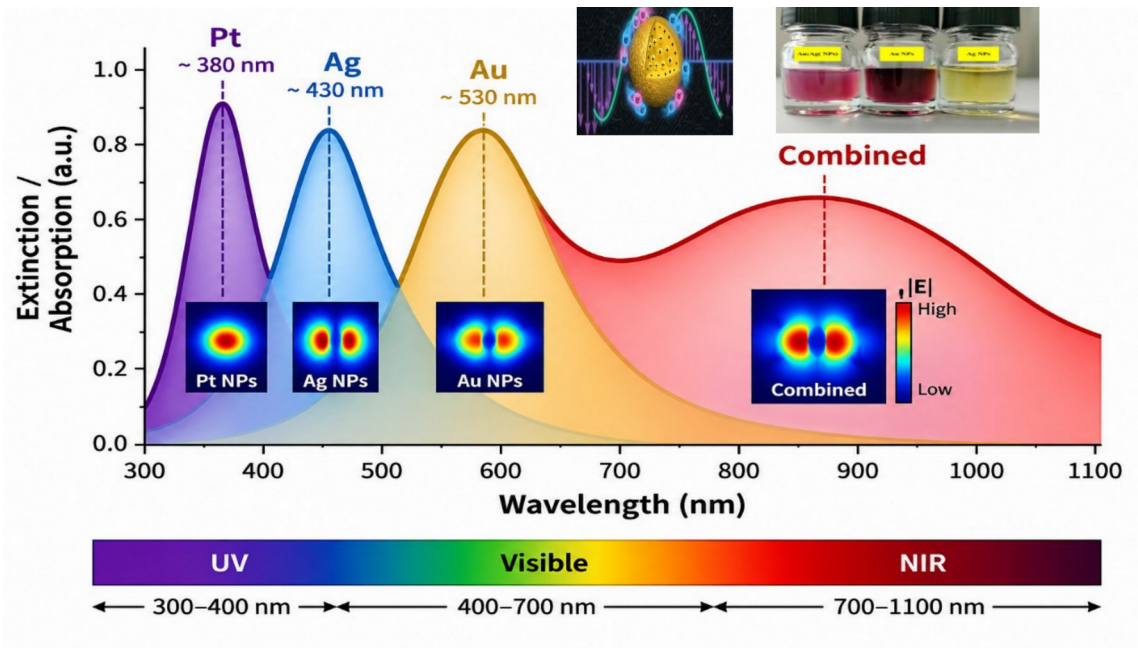

Figure 1. Extinction/absorption spectra of Pt, Ag, and Au nanoparticles and their combined plasmonic response spanning the UV-Vis-NIR range, with corresponding near-field |E| distribution maps and nanoparticle-solution photographs.

Introduction

Broadband photodetectors (PDs) that respond from the ultraviolet (UV) and visible (Vis) to the near-infrared (NIR) have attracted growing interest for applications in optical communication, imaging, spectroscopy, environmental monitoring, remote sensing, and biomedical detection. Compared with narrowband PDs, broadband devices can provide information across multiple spectral

regions, making them attractive for multifunctional sensing systems [1]. Spectroscopy is an important application of broadband photodetection and includes absorption, emission, scattering, reflection, and transmission techniques. Common methods such as UV–Vis–NIR, Fourier-transform infrared (FTIR), and Raman spectroscopy rely on sensitive optical detection to convert wavelength-dependent light–matter interactions into electrical signals. Therefore, detector spectral range, responsivity, detectivity, response speed, and noise directly affect spectroscopic performance. However, conventional semiconductor PDs are often optimized for limited wavelength ranges, making broad UV–Vis–NIR detection challenging. Plasmonic–semiconductor hybrid structures provide a promising approach by enhancing light–matter interaction through localized surface plasmon resonance (LSPR), near-field enhancement, light scattering, light trapping, and hot-carrier generation [2]. In particular, combining different metallic plasmonic nanoparticles, such as Au, Ag, and Pt, with nanostructured semiconductors and conductive Organic polymers like poly(3-hexylthiophene) (P3HT) and poly(3,4-ethylenedioxythiophene) poly(styrene sulfonate) (PEDOT: PSS) offers an opportunity to exploit their complementary optical properties and achieve a broader spectral response [3]. This study therefore discusses the materials, architectures, plasmonic mechanisms, and performance of such hybrid photodetectors, with particular emphasis on their potential for broadband UV–Vis–NIR and NIR photodetection for advanced spectroscopy and optoelectronic applications.

Methodology

This study considers reported approaches to fabricating and investigating plasmonic–semiconductor hybrid photodetectors based on nanostructured semiconductors, porous silicon, metallic nanoparticles, and organic–inorganic hybrid materials. The fabrication strategies include photoelectrochemical etching, hydrothermal growth, coating and deposition techniques, pulsed laser ablation in liquid, UV photo-deposition, and casting-based film deposition. Particular attention is given to the incorporation of Au, Ag, and mixed metallic nanoparticles into semiconductor and conductive-polymer architectures. The reviewed studies use structural, morphological, optical, and electrical characterization to examine interactions between plasmonic nanoparticles and photoactive materials. Photodetector performance is generally evaluated through spectral responsivity, photocurrent, detectivity, external quantum efficiency, and response/recovery characteristics under UV–Vis–NIR illumination. These fabrication and characterization approaches provide a basis for understanding how nanoparticle composition, semiconductor structure, plasmonic coupling, and device architecture influence broadband photodetection performance.

Results and Discussion

The fabricated plasmonic–semiconductor photodetectors demonstrated enhanced broadband UV–Vis–NIR performance. For ZnO NRs/PSi MSM devices, Au and Ag NPs synthesized by PLAL exhibited spherical morphologies with average sizes of 10.5 and 31.5 nm, respectively, and distinct LSPR bands at 528 and 429 nm. The mixed Au–Ag NPs showed both plasmonic bands, indicating complementary optical responses. Nanoparticle decoration reduced reflectance, enhanced optical absorption, and increased surface roughness, while FESEM/TEM/EDX and XRD confirmed successful integration of the NPs with ZnO NRs. The decorated devices showed higher photocurrent, responsivity, EQE, and sensitivity than the undecorated device. The Au–Ag/ZnO NRs/PSi device achieved the highest responsivity, demonstrating the benefit of mixed plasmonic nanoparticles for broadband detection. Similarly, PEDOT:PSS/metal-NP/n-PSi p–n heterojunction photodetectors exhibited broadband UV–NIR response. Incorporation of Au, Ag, and particularly mixed Au–Ag NPs reduced optical reflectance and enhanced light absorption through plasmonic effects. The metal-NP/PEDOT:PSS devices showed improved responsivity, EQE, and sensitivity over 425–940 nm compared with pristine PEDOT:PSS. The devices also demonstrated good stability, repeatability, and reversibility. Overall, these results demonstrate that combining plasmonic nanoparticles with semiconductor and organic–inorganic architectures is an effective strategy for improving broadband photodetection performance.

Conclusion

In conclusion, plasmonic–semiconductor hybrid architectures provide a promising strategy for broadband UV–Vis–NIR photodetection. Integrating Au, Ag, and mixed Au–Ag nanoparticles with ZnO NRs/PSi and PEDOT: PSS/n-PSi structures enhances light absorption and photodetector performance through plasmonic effects. In particular, the mixed Au–Ag nanoparticles demonstrated complementary optical responses and superior device performance compared with individual nanoparticles. The achieved improvements in responsivity, EQE, sensitivity, stability, and response speed highlight the potential of these hybrid structures for broadband spectroscopy, sensing, and next-generation optoelectronic applications.

Acknowledgement

The authors express sincere gratitude to the Ministry of Higher Education Malaysia for financial support through the Fundamental Research Grant Scheme (FRGS), Project Code: FRGS/1/2023/STG07/USM/02/1. We also thank the Institute of Nano Optoelectronics Research and Technology (INOR) at Universiti Sains Malaysia and the Nano-Optoelectronics Research and Technology Laboratory (NOR Lab) at the School of Physics, Universiti Sains Malaysia (USM).

References

[1] Alwadai, N., Haque, M.A., Mitra, S., Flemban, T., Pak, Y., Wu, T. and Roqan, I., 2017. High-performance ultraviolet-to-infrared broadband perovskite photodetectors achieved via inter-/intraband transitions. ACS applied materials & interfaces, 9(43), pp.37832-37838.

[2] Soomro, A.A., Mohammad, S.M., Afzal, N., Abdullah, M., Ramzan, M., Kumar, Y.N.S., Naseer, H. and Ahmad, M.A., 2026. Enhanced performance broadband UV-C to visible photodetectors utilizing plasmonic metal nanoparticle-decorated β-Ga2O3 nanorods on p-GaN/sapphire. Journal of Materials Science: Materials in Electronics, 37(21), p.1616.

[3] Abed, S.M., Mohammad, S.M., Sifawa, A.A., Hassan, Z., Abdullah, M. and Naser, H., 2025. Fabrication of self-powered and broadband photodetectors based on plasmonic nanoparticles-PEDOT: PSS composite/porous Si heterojunction. Journal of Materials Science: Materials in Electronics, 36(29), p.1858.

Quantum Transparency and Giant Spontaneous Emission in Near-Infrared Overtone Transitions via Two-Mode Squeezed Vacuums

Edmund Loh Wai Ming[1*]

[1]School of Physics, Universiti Sains Malaysia, 11800 USM, Penang, Malaysia

***Corresponding author:** edmund_waiming@usm.my

Abstract

Near-infrared (NIR) spectroscopy is inherently limited by the incredibly weak transition dipole moments of molecular vibrational overtones. While standard quantum-enhanced spectroscopy focuses on entangled-photon absorption, we investigate the steady-state dynamics of a Ξ-type three-level molecular system continuously coupled to a broadband two-mode squeezed vacuum (TMSV) reservoir. Through a rigorous first-principles derivation of the Lindblad master equation, we demonstrate that tuning the TMSV pump frequency to resonate with the NIR overtone transition completely suppresses linear absorption, yielding a non-classical analogue of electromagnetically induced transparency (EIT). Furthermore, the tailored quantum reservoir induces a macroscopic zeroth-order coherence that fuels a giant enhancement in both spontaneous NIR emission and third-order nonlinear susceptibility (χ^3). This paradigm shift opens new pathways for ultra-low-power nonlinear photonics and quantum-enhanced emission spectroscopy.

Keywords: *Near-Infrared Spectroscopy, Molecular Overtones, Two-Mode Squeezed Vacuum, Lindblad Master Equation, Electromagnetically Induced Transparency, Nonlinear Susceptibility.*

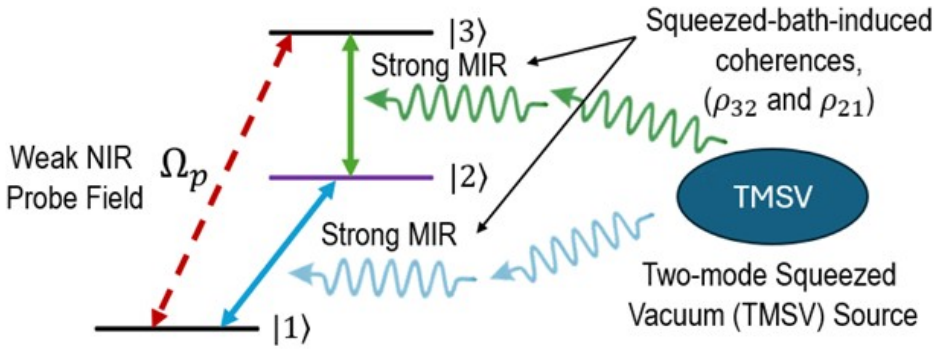

Figure 1. Energy-level scheme of the Ξ-type three-level molecular system coupled to a two-mode squeezed vacuum (TMSV) reservoir.

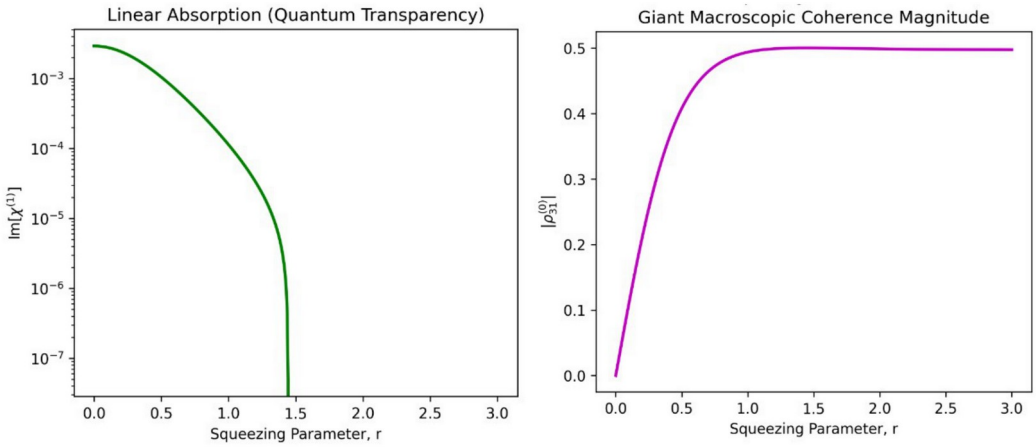

Figure 2. Linear absorption (quantum transparency) and giant macroscopic coherence magnitude as functions of the squeezing parameter r.

Introduction

The physical mechanism underlying NIR spectroscopy relies on the excitation of molecular vibrational overtones and combination bands whose transition dipole moments are orders of magnitude weaker than fundamental transitions in the mid-infrared (MIR) [1, 2]. To overcome these weak cross-sections, modern research has increasingly turned toward quantum-enhanced spectroscopy, particularly through the utilization of entangled photon pairs and squeezed light [3-5]. However, most theoretical and experimental efforts focus entirely on the transient absorption of discrete entangled photon pairs or specific Raman scattering geometries [6, 7]. The steady-state dynamics of a highly forbidden molecular overtone continuously bathed in a broadband non-classical reservoir remain largely unexplored. It is currently unknown whether the stationary macroscopic coherences induced by a phase-locked quantum bath can fundamentally alter the linear and nonlinear susceptibility of a weak NIR transition, potentially providing a new mechanism for steady-state signal enhancement [8, 9]. In this work, we present an exact analytical theory demonstrating that this configuration bypasses classical linear absorption entirely, instead yielding perfect quantum transparency and giant steady-state spontaneous emission.

Theoretical Framework: Open Quantum Systems and Master Equation Dynamics

The molecular bond is modelled as a three-level ladder (Ξ-type) open quantum system. The basis states are defined as: $|1\rangle$ representing the vibrational ground state, $|2\rangle$ representing the first excited vibrational state (fundamental, MIR region), and $|3\rangle$ representing the second excited vibrational state (first overtone, NIR region). We probe the highly forbidden $|1\rangle \rightarrow |3\rangle$ NIR transition with a weak classical field. Simultaneously, the cascaded $|1\rangle \rightarrow |2\rangle$ and $|2\rangle \rightarrow |3\rangle$ transitions are coupled directly to a broadband TMSV reservoir. To capture the microscopic dynamics of the molecule-bath interaction, we work within the framework of open quantum systems by solving the Redfield master equation. To extract the linear response and analyze the physical enhancements of the system, we implement standard perturbation theory, separating the OBEs into a zeroth-order background state (driven purely by the quantum bath, $\Omega p=0$) and a first-order response to the weak classical probe field.

Results and Discussion

When the exact cross-coupling rate and the correlation condition are substituted into the population inversion matrices, the intermediate state's population evaluates exactly to zero, i.e. $\rho_{22}^{0}=0$. This establishes the creation of a fundamentally decoupled dark state. As a result, the ground and overtone states approach an asymptotic 50/50 thermal split at high squeezing limits, breaking classical Boltzmann distribution rules. Also, by isolating the terms linear in Ωp, we derive the exact closed-form linear absorption cross-section. From the expression, it is found that as the squeezing parameter increases, the bath actively populates the overtone state, driving the population inversion $\rho_{11}^{0}-\rho_{33}^{0}$ toward zero. Simultaneously, the transverse decoherence rate Γ_{31} grows exponentially due to the

presence of thermal bath photons. The interaction proves that the TMSV induces a non-classical equivalent of Electromagnetically Induced Transparency (EIT). The medium becomes perfectly transparent to the classical NIR probe, shifting the absorption profile to near-zero amplitude. Accompanying this drop in absorption is a massive steepening of the real dispersion curve $\mathrm{Re}\chi^{1}$, enabling "slow light" applications and phase-shift spectroscopy without requiring a high-intensity coupling laser. Besides, exact algebraic derivation reveals the persistence of a massive, phase-locked zeroth-order coherence directly induced by the squeezed vacuum, $\rho_{31}{}^{0} = -\gamma \mathrm{sqMe}^{-i\Phi}/2\Gamma_{31}$. This macroscopic permanent dipole acts as a constant emission source without any coherent classical drive. It rapidly grows with increasing squeezing parameter, r and asymptotically approaches the maximum theoretical limit of 0.5 at high squeezing.

Conclusion

We have presented a rigorous, exact microscopic derivation of a Ξ-type molecular system interacting with a continuous-wave, two-mode squeezed vacuum. Contrary to early phenomenological predictions of linear NIR absorption enhancement, the Lindbladian treatment reveals that the medium becomes highly transparent to linear probing due to the phase-matched formation of an intermediate dark state. However, the exact generation of a phase-locked zeroth-order coherence $\rho_{31}{}^{0}$ bypasses traditional forbidden-transition limitations, providing a massive, tunable enhancement in spontaneous emission and third-order nonlinearity. This theoretical framework establishes that near-infrared overtone transitions can be leveraged for ultra-sensitive phase-shift spectroscopy, quantum-enhanced fluorescence, and low-power all-optical switching when properly integrated with highly structured quantum optical reservoirs.

Acknowledgement

This work was supported by the Universiti Sains Malaysia, Research University Individual (RUI) Grant Scheme (Grant Number: R502-KR-ARU001-0000001140-K134).

References

[1] H.-W. Wang, N. Chai, P. Wang, S. Hu, W. Dou, D. Umulis, L. V. Wang, M. Sturek, R. Lucht, and J.-X. Cheng, "Label-Free Bond-Selective Imaging by Listening to Vibrationally Excited Molecules," Physical Review Letters, vol. 106, no. 23, 2011, doi: https://doi.org/10.1103/physrevlett.106.238106.

[2] S. D. Fried and S. G. Boxer, "Measuring Electric Fields and Noncovalent Interactions Using the Vibrational Stark Effect," Accounts of Chemical Research, vol. 48, no. 4, pp. 998–1006, 2015, doi: https://doi.org/10.1021/ar500464j.

[3] D. Adamou, L. Hirsch, T. Shields, S. Yoon, A. C. Dada, J. M. R. Weaver, D. Faccio, M. Peccianti, L. Caspani, and M. Clerici, "Quantum-enhanced time-domain spectroscopy," Science Advances, vol. 11, no. 4, 2025, doi: https://doi.org/10.1126/sciadv.adt2187

[4] A. Eshun, O. Varnavski, J. P. Villabona-Monsalve, R. K. Burdick, and T. Goodson, "Entangled Photon Spectroscopy," Accounts of Chemical Research, vol. 55, no. 7, pp. 991–1003, 2022, doi: https://doi.org/10.1021/acs.accounts.1c00687

[5] R. de J. León-Montiel, J. Svozilík, J. P. Torres, and A. B. U'Ren, "Temperature-Controlled Entangled-Photon Absorption Spectroscopy," Physical Review Letters, vol. 123, no. 2, 2019, doi: https://doi.org/10.1103/physrevlett.123.023601

[6] M. G. Raymer and T. Landes, "Theory of two-photon absorption with broadband squeezed vacuum," Physical Review A, vol. 106, no. 1, 2022, doi: https://doi.org/10.1103/physreva.106.013717

[7] F. Schlawin, K. E. Dorfman, and S. Mukamel, "Entangled Two-Photon Absorption Spectroscopy," Accounts of Chemical Research, vol. 51, no. 9, pp. 2207–2214, 2018, doi: https://doi.org/10.1021/acs.accounts.8b00173

[8] K. E. Dorfman, F. Schlawin, and S. Mukamel, "Nonlinear optical signals and spectroscopy with quantum light," Reviews of Modern Physics, vol. 88, no. 4, 2016, doi: https://doi.org/10.1103/revmodphys.88.045008

[9] G. Guarnieri, M. Kolář, and R. Filip, "Steady-State Coherences by Composite System-Bath Interactions," Physical Review Letters, vol. 121, no. 7, 2018, doi: https://doi.org/10.1103/physrevlett.121.070401

Rapid and Non-Destructive Assessment of Fruit Quality Using UV-Vis-NIR Spectroscopy and Chemometric Analysis: A Mini Review

Muna E. Raypah[1], Ahmad Fairuz Omar[2], Mohd Faizal Jamlos[3,4*]

[1]Centre for Artificial Intelligence & Data Science, Universiti Malaysia Pahang Al-Sultan Abdullah, 26300, Gambang, Malaysia

[2]School of Physics, Universiti Sains Malaysia, 11800, Pulau Pinang, Malaysia

[3]Faculty of Electrical & Electronics Engineering Technology, Universiti Malaysia Pahang Al-Sultan Abdullah, 26600, Pekan, Malaysia

[4]Centre for Climate Transition & Disaster Risk, Universiti Malaysia Pahang Al-Sultan Abdullah, 26600, Pekan, Malaysia

***Corresponding author:** mohdfaizaljamlos@gmail.com

Introduction

Fruit ripeness, internal composition, physiological state, and postharvest deterioration must be quickly and accurately assessed to maintain fruit quality from harvest to consumption. Ultraviolet-visible-near-infrared (UV-Vis-NIR) spectroscopy has become a viable platform for quick, reagent-free, and non-destructive fruit quality evaluation, especially when combined with chemometric and machine-learning (ML) techniques. The spectroscopic foundation, chemometric procedure, main uses, and practical constraints of UV-Vis-NIR spectroscopy for fruit-quality evaluation are examined in this review. Figure 1 presents this review conceptual framework, outlining the progression from spectral acquisition and preprocessing to chemometric and machine-learning modelling, fruit-quality prediction, decision-making, and future developments in non-destructive assessment.

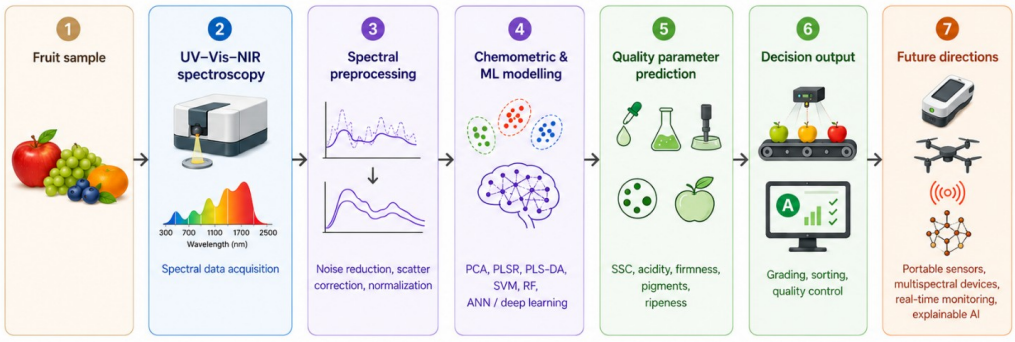

Figure 1. Schematic overview of UV-Vis-NIR spectroscopy for non-destructive fruit-quality assessment.

Spectroscopic Basis of Fruit-Quality Assessment

The UV region is mainly surface-sensitive because to its low penetration into intact biological tissues, and as a result, it is less frequently used independently for assessing the internal quality of whole fruits. However, UV absorption can reveal details about cuticular waxes, surface chromophores, phenolic components, and physiological or defect-related alterations. The visible region is especially sensitive to changes in anthocyanins, carotenoids, and chlorophylls that rely on maturity. As a result, it is useful for assessing peel color, maturity, pigment deterioration, bruising, and surface flaws. In contrast, large overtone and combination bands that mostly result from O-H, C-H, and N-H molecule vibrations can be found in the NIR area. Water, sugars, proteins, organic acids, carbohydrates, and other biological components are linked to these spectrum reactions. Light scattering from cellular structures, intercellular gaps, peel characteristics, tissue density, and moisture distribution have an impact on NIR spectra.

Spectral Preprocessing and Chemometric Modelling

Fruit spectra are complicated due to the wide and overlapping absorption bands that are impacted by both physical structure and chemical structure. For this reason, chemometric analysis is crucial to obtaining high-quality information. Spectral acquisition, reference measurement, spectral preprocessing, exploratory analysis, variable selection, model construction, and independent validation are typical steps in an analytical workflow. Smoothing, standard normal variate transformation, multiplicative scatter correction, detrending, derivatives, baseline correction, and normalization are common preprocessing techniques. Principal component analysis (PCA) is frequently utilized to display spectral variability, find outliers, and determine clustering by cultivar, maturity, storage, or treatment. While linear discriminant analysis (LDA), partial least-squares discriminant analysis (PLS-DA), support vector machines (SVM), random forests (RF), and artificial neural networks (ANN) are utilized for classification tasks like maturity grading, cultivar authentication, and defect detection. Partial least-squares regression (PLSR) is still frequently used to predict fruit-quality attributes.

Recent Applications in Fruit-Quality Evaluation

Portable Vis-NIR and hyperspectral methods predicted apricot soluble solids and dry matter more reliably than acidity [1]. Similar approaches enabled soluble-solids prediction in white strawberries and grape ripening assessment [2, 3]. NIR spectroscopy also distinguished natural from calcium-carbide banana ripening [4]. These investigations show the usefulness of spectral techniques for fruit-quality categorization and prediction.

Current Limitations and Future Research Priorities

Variability in fruit and instruments can limit model transferability between cultivars, seasons, and production sites and lower spectral repeatability. Additionally, performance may be overestimated if calibration and validation are separated randomly within the same batch. Future research should disclose acquisition, preprocessing, modelling, and validation techniques in detail, use independent validation datasets, and maintain repeated spectra from each fruit inside a single partition. Reliable orchard, storage, and sorting applications depend on reduced-wavelength sensors, interpretable ML, calibration transfer, and multi-season datasets.

Conclusion

Fruit quality can be quickly and non-destructively assessed using UV-Vis-NIR spectroscopy and chemometrics. Representative datasets, precise validation, and transferable models are necessary for reliable applications. Improvements in portable sensors could lower postharvest losses and enable automated grading.

Acknowledgment

The authors would like to acknowledge funding from the Malaysian Ministry of Higher Education under Industry Matching Programme with grant number RDU243808 & UIC240845 and Universiti Malaysia Pahang Al-Sultan Abdullah (UMPSA) Special Grant with grant number SPU260101.

References

[1] Amoriello, T., et al., Vis/NIR spectroscopy and Vis/NIR hyperspectral imaging for non-destructive monitoring of apricot fruit internal quality with machine learning. Foods, 2025. 14(2): p. 196.

[2] Seki, H., et al., Evaluating soluble solids in white strawberries: a comparative analysis of Vis-NIR and NIR spectroscopy. Foods 13: 2274. 2024.

[3] Elsherbiny, O., et al., Incorporation of visible/near-infrared spectroscopy and machine learning models for indirect assessment of grape ripening indicators. Scientific Reports, 2025. 15(1): p. 12345.

[4] Zaukuu, J.L.Z., et al., Combining NIR spectroscopy with chemometrics for discriminating naturally ripened banana and calcium carbide ripened banana. npj Science of Food, 2024. 8(1): p. 86.

Non-Destructive Prediction of SSC and pH in Harumanis Mango Using VIS–NIR Spectroscopy and Machine Learning

Anam Irshad[1], Sheikh Daniyal Shahid[2], Ahmad Fairuz Omar[1*]

[1]School of Physics, Universiti Sains Malaysia, 11800 USM, Penang, Malaysia

[2]School of Aerospace Engineering, Universiti Sains Malaysia, Engineering Campus, 14300 Nibong Tebal, Penang, Malaysia

***Corresponding author:** fairuz_omar@usm.my

Keywords: *Harumanis, Vis–NIR, PCA, Machine Learning, SSC, pH*

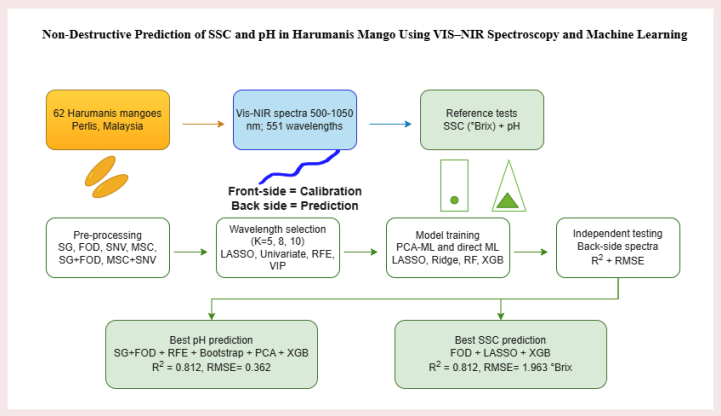

Abstract

Harumanis mango is a premium Malaysian fruit, and its market value depends strongly on internal quality attributes such as soluble solids content (SSC) and pH. These qualities are usually measured using destructive laboratory methods, which are time-consuming, damage the fruit, and are not practical for rapid grading. This study presents a non-destructive approach for predicting SSC and pH in Harumanis mango using visible–near infrared (VIS–NIR) spectroscopy combined with chemometric and machine-learning models.

A total of 62 Harumanis mango samples were collected from orchards in Perlis, Malaysia. Spectral data were acquired from both the front and back sides of each fruit within the wavelength range of 500–1050 nm. To make the prediction task more realistic, the front-side spectra were used for model calibration, while the back-side spectra were used only for external prediction. Reference SSC and pH values were measured using a digital refractometer and a handheld pH meter. Several spectral pre-processing methods were tested, including Savitzky–Golay smoothing, first-order derivative, standard normal variate, multiplicative scatter correction, and their combinations. Important wavelengths were selected using LASSO, recursive feature elimination, univariate selection, and variable importance in projection.

Two modelling pipelines were compared. The first used principal component analysis before regression, while the second applied machine-learning models directly to the selected wavelengths. Random Forest, XGBoost, Ridge, and LASSO regression models were evaluated with different augmentation strategies, including noise addition and bootstrap resampling. Model performance was assessed using the coefficient of determination and root mean square error.

The results show that VIS–NIR spectroscopy can predict both SSC and pH with useful accuracy using only a small number of selected wavelengths. For pH, the best external prediction was obtained using SG+FOD pre-processing, RFE feature selection, bootstrap augmentation, PCA, and XGBoost,

with R^2 = 0.812 and RMSE = 0.362 pH units. For SSC, the best result was achieved using FOD pre-processing, LASSO feature selection, and direct XGBoost modelling, with R^2 = 0.812 and RMSE = 1.963 °Brix. The most informative spectral regions were mainly found in the visible green band, the red-edge region, and the upper NIR range.

Overall, this study shows that VIS–NIR spectroscopy, supported by careful wavelength selection and machine learning, can provide a fast and non-destructive tool for Harumanis mango quality assessment. This approach can support better grading decisions, reduce fruit damage, and help move towards portable sensing systems for practical use in the mango industry.

Spectral discriminant analysis for classifying normal and cancerous prostate cells

Razemy Raffay[1], Mohd Hafiz Mail[2], Ahmad Fairuz Omar[1*]

[1]School of Physics, Universiti Sains Malaysia, 11800 USM, Penang, Malaysia.

[2]Malaysian Institute of Pharmaceuticals and Nutraceuticals, National Institutes of Biotechnology Malaysia, Halaman Bukit Gambir, 11700 Gelugor, Pulau Pinang, Malaysia.

***Corresponding author:** fairuz_omar@usm.my

Abstract

This study investigates the potential of short-wave near-infrared (SWNIR) spectroscopy combined with chemometric techniques for classifying normal and cancerous prostate cells. Absorbance spectra of RWPE-1 (normal), LNCaP, and DU145 (cancerous) prostate cell lines were acquired in the 808–1093 nm range and preprocessed using the Savitzky–Golay first derivative method. Principal Component Analysis (PCA) and Partial Least Squares Discriminant Analysis (PLS-DA) were used to identify discriminative spectral features. PCA successfully differentiated normal and cancerous cells and identified three potential spectral signatures at 814.77, 876.17, and 1089.53 nm. PLS-DA provided better discrimination and identified seven additional spectral signatures. These findings demonstrate that SWNIR spectroscopy combined with chemometric analysis can effectively classify prostate cells and identify potential spectral biomarkers for cancer detection.

Keywords: *Near-infrared spectroscopy, prostate cancer cells, spectral signatures, principal component analysis (PCA), partial least squares discriminant analysis (PLS-DA)*

Introduction

Spectral signatures provide valuable information for distinguishing normal and cancerous cells by reflecting differences in their biochemical composition. Cancer-related changes in proteins, lipids, nucleic acids, and cellular structure produce distinct spectral patterns that can be detected using spectroscopic techniques. Previous studies have demonstrated the effectiveness of chemometric methods such as PLS-DA, PCA, and SIMCA for cancer classification and the identification of significant spectral wavelengths. However, the application of chemometric techniques to distinguish normal RWPE-1 from cancerous LNCaP and DU145 prostate cells remains limited. Therefore, this study applies chemometric analysis to NIR spectral data to classify normal and cancerous prostate cells and identify potential spectral features for cancer detection [1]–[6].

Methodology

This study cultured normal prostate cells (RWPE-1) in K-SFM medium and cancerous prostate cells (LNCaP and DU145) in RPMI and MEM media, respectively, based on the recommended media from the American Type Culture Collection (ATCC). The cells were cultured until sufficient cell counts were obtained for the experiments. Absorbance measurements were performed using a QE65000 spectrometer with cell samples placed in cuvettes containing 4 mL of the respective culture medium. For each cell line, five cell concentrations were prepared: 0k, 200k, 400k, 600k, and 800k cells. The 0k sample served as the control and contained only the corresponding culture medium without cells. In total, 60 samples were prepared for absorbance measurements.

Results and Discussion

Figure 1 (A) shows that PCA can clearly differentiate normal prostate cells (RWPE-1) from cancerous cells (LNCaP and DU145) based on their PC1 scores. RWPE-1 cells are located on the negative side of PC1, while LNCaP and DU145 cells are located on the positive side, indicating distinct spectral patterns between normal and cancerous cells. Along PC2, LNCaP, RWPE-1, and DU145 are

positioned according to their cell sizes, with LNCaP being the smallest, RWPE-1 intermediate, and DU145 the largest. The culture media controls (K-SFM, RPMI, and MEM) are located near the origin, indicating that the different culture media do not interfere with the identification of the prostate cell types. The PCA correlation loadings in Figure 1 (B) identified 814.77 nm and 876.17 nm as potential spectral signatures for cancerous and normal prostate cells, respectively, while 1089.53 nm was associated with DU145 cells and cell size. Overall, PCA successfully identified three potential spectral signatures 814.77, 876.17, and 1089.53 nm for discriminating the three prostate cell types.

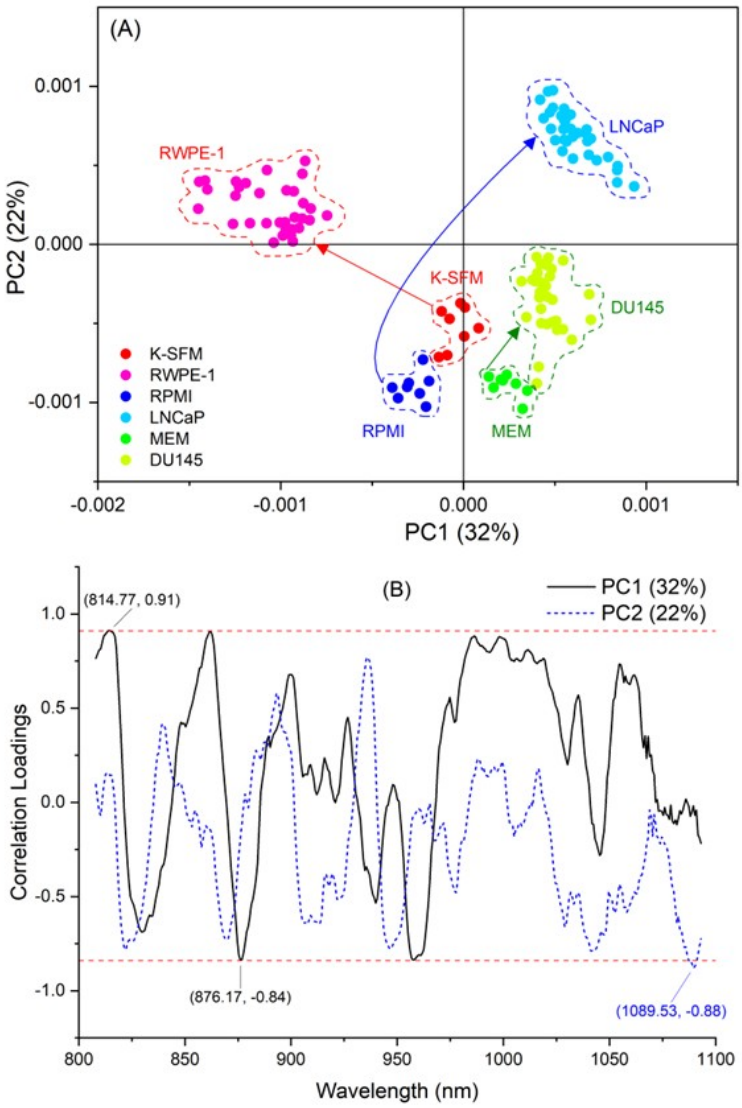

Figure 1 PCA Results (A) 2D Scores plot and (B) Correlation Loadings plot for PC1xPC2

PLS-DA was applied as a supervised method to identify additional spectral signatures for discriminating among RWPE-1, LNCaP, and DU145 prostate cells using first-derivative (FD) spectra in the SWNIR region. Unlike PCA, PLS-DA uses class labels and maximizes the covariance between the wavelengths (X) and prostate cell types (Y), resulting in improved class separation. The PLS-DA score plots as presented in Figure 2 showed clear separation between RWPE-1 and LNCaP, RWPE-1 and DU145, LNCaP and DU145, and normal and cancerous prostate cells. Regression coefficient analysis identified seven potential spectral signatures at 896.75, 906.28, 960.27, 961, 987.81, 991.42, and 1061.07 nm. The wavelengths 896.75 and 987.81 nm were associated with LNCaP cells, while 906.28 and 1061.07 nm were associated with DU145 cells. The wavelengths 960.27 and 961 nm were associated with RWPE-1 cells, while 991.42 nm was associated with cancerous prostate cells. Overall, PLS-DA successfully discriminated the three prostate cell types and identified additional potential spectral signatures for their classification.

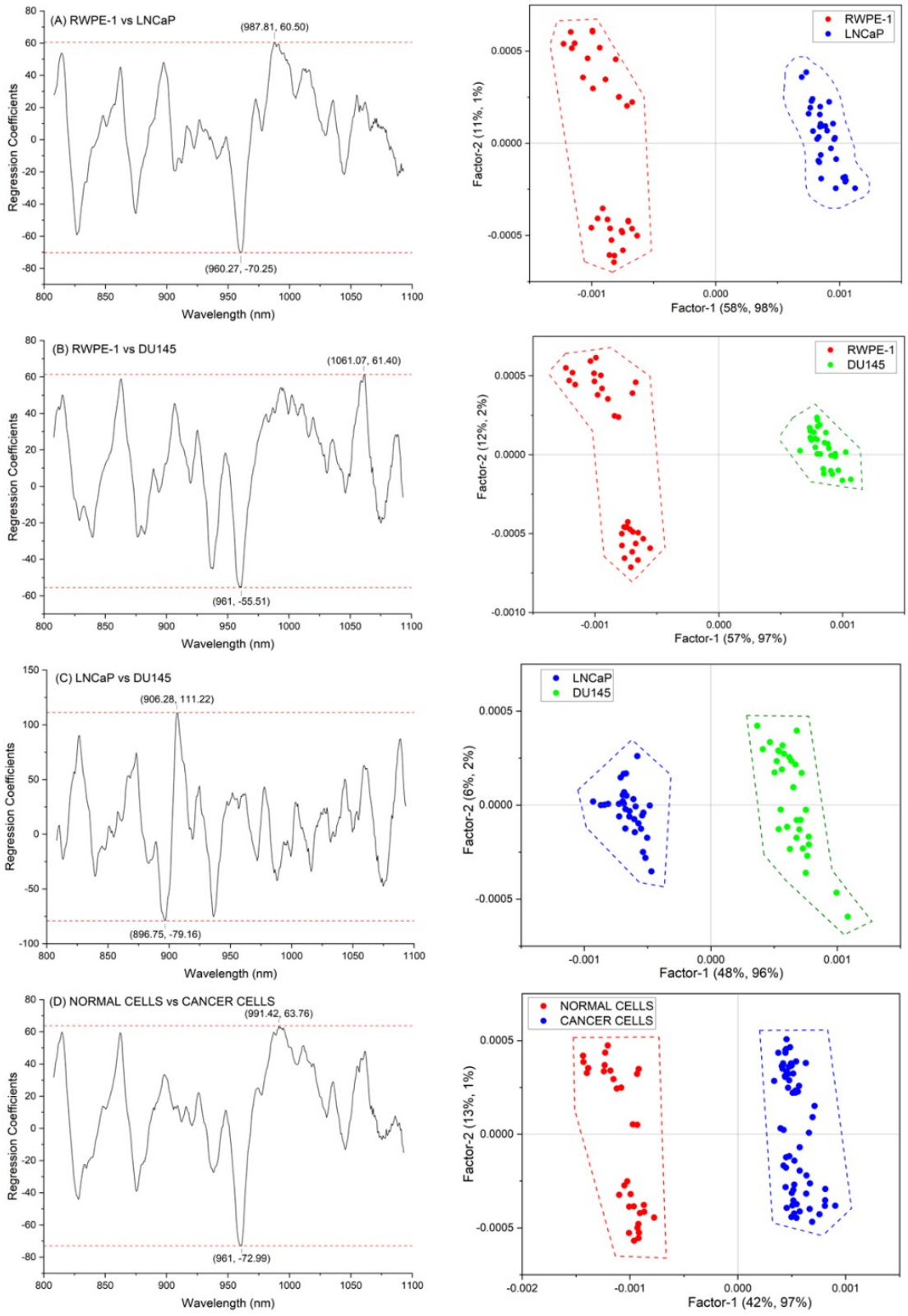

Figure 2 PLS-DA Results (A) RWPE-1 vs LNCaP, (B) RWPE-1 vs DU145 (C) LNCaP vs DU145 (D) Normal Prostate Cells vs Cancerous Prostate Cells

Conclusion

PCA and PLS-DA successfully identified a total of 10 potential spectral signatures for discriminating between normal and cancerous prostate cells. PCA identified three spectral signatures at 814.77, 876.17, and 1089.53 nm. PLS-DA identified seven additional spectral signatures at 896.75, 906.28, 960.27, 961, 987.81, 991.42, and 1061.07 nm. These spectral signatures show potential for distinguishing

among the three prostate cell types, namely RWPE-1, LNCaP, and DU145. The combined use of PCA and PLS-DA therefore provides complementary information for identifying spectral features associated with normal and cancerous prostate cells as summarized in Table 1.

Table 1. The summary of spectral signatures to discriminate the normal prostate cells and cancerous prostate cells

	Spectral signatures	Absorbance Intensity
LNCaP and DU145 (Cancerous Prostate Cells)	814.77 nm 991.42 nm	Cancerous Prostate: High intensity Normal Prostate: Low intensity
RWPE-1 (Normal Prostate Cells)	876.17 nm 960.27 nm 961 nm	RWPE-1: High intensity Non-RWPE-1: Low intensity
LNCaP (Cancerous Prostate Cells)	896.75 nm 987.81 nm	LNCaP: High intensity Non-LNCaP: Low intensity
DU145 (Cancerous Prostate Cells)	906.28 nm 1061.07 nm 1089.53 nm	DU145: High intensity Non-DU145: Low intensity

Acknowledgements

The authors gratefully acknowledge the financial support of this research by the Ministry of Higher Education Malaysia for Fundamental Research Grant Scheme (Grant No. FRGS/1/2020/STG07/USM/02/8).

References

[1] S. L. Jain, A. G. A. Thomas, G. Zhuo, and N. Mazumder, "Fourier Transform Infrared (FTIR) Spectroscopy of Biomolecules," Recent Adv. Infrared Spectrosc. Its Appl. Biotechnol., p. 101, 2025, doi: 10.5772/intechopen.1010234.

[2] R. Irshad and M. Husain, "Aberrant Lipid Metabolism in Cancer: Current Status and Emerging Therapeutic Perspectives.," Curr. Top. Med. Chem., vol. 23, no. 12, pp. 1090–1103, 2023, doi: 10.2174/1568026623666230522103321.

[3] U. Sharaha, D. Hania, I. Lapidot, A. Salman, and M. Huleihel, "Early Detection of Pre-Cancerous and Cancerous Cells Using Raman Spectroscopy-Based Machine Learning," Cells, vol. 12, 2023, doi: 10.3390/cells12141909.

[4] Q. Lu et al., "Rapid screening of esophageal squamous cell carcinoma by near-infrared spectroscopy combined with aquaphotomics," Talanta, vol. 285, no. August 2024, p. 127399, 2025, doi: 10.1016/j.talanta.2024.127399.

[5] A. Surkova, E. Boichenko, O. Bibikova, V. Artyushenko, J. Muncan, and R. Tsenkova, "Near-Infrared Spectroscopy and Aquaphotomics in Cancer Research: A Pilot Study," J. Chemom., pp. 1–10, 2024, doi: 10.1002/cem.3600.

[6] M. E. Raypah et al., "Integration of near-infrared spectroscopy and aquaphotomics for discrimination of cultured cancerous cells using phenol red," Chemom. Intell. Lab. Syst., vol. 227, no. March, 2022, doi: 10.1016/j.chemolab.2022.104611.

Optimizing Nutrient Efficiency in Harumanis Mango Seedlings: A Spectroscopic Approach to Mapping PGPB and NPK Interactions

Saidu Abdullahi[1], Aishatu Muhammad Gurama[1], Anam Irshad[2], Ahmad Fairuz Omar[2], Amir Hamzah Ghazali[1*]

[1]School of Biological Sciences, Universiti Sains Malaysia, 11800 USM, Penang, Malaysia

[2]School of Physics, Universiti Sains Malaysia, 11800 USM, Penang, Malaysia

***Corresponding author:** amirhg@usm.my

Abstract

The integration of plant growth-promoting bacteria (PGPB) with reduced mineral fertilizer is a sustainable strategy for enhancing plant production. A six-month greenhouse experiment assessed various combinations of NPK fertilizer and PGPB on Harumanis mango seedlings using near-infrared (NIR) spectroscopy and SPAD chlorophyll measurements. Distinct spectral responses were noted among treatments, particularly in the near-infrared (600–1000 nm). Linear discriminant analysis and support vector machine analysis demonstrated effective treatment separation and classification performance. The structural and photosynthetic capacity of Harumanis mango seedlings peaks cleanly at 75% NPK. Additionally, SPAD values increased, with the 75% NPK + PGPB treatment yielding the highest chlorophyll content after six months. Overall, NIR spectroscopy and SPAD measurements are effective non-destructive methods for monitoring physiological responses in mango seedlings under integrated nutrient management.

Keywords: *Harumanis mango, Plant growth-promoting bacteria (PGPB), Spectro-agronomic evaluation*

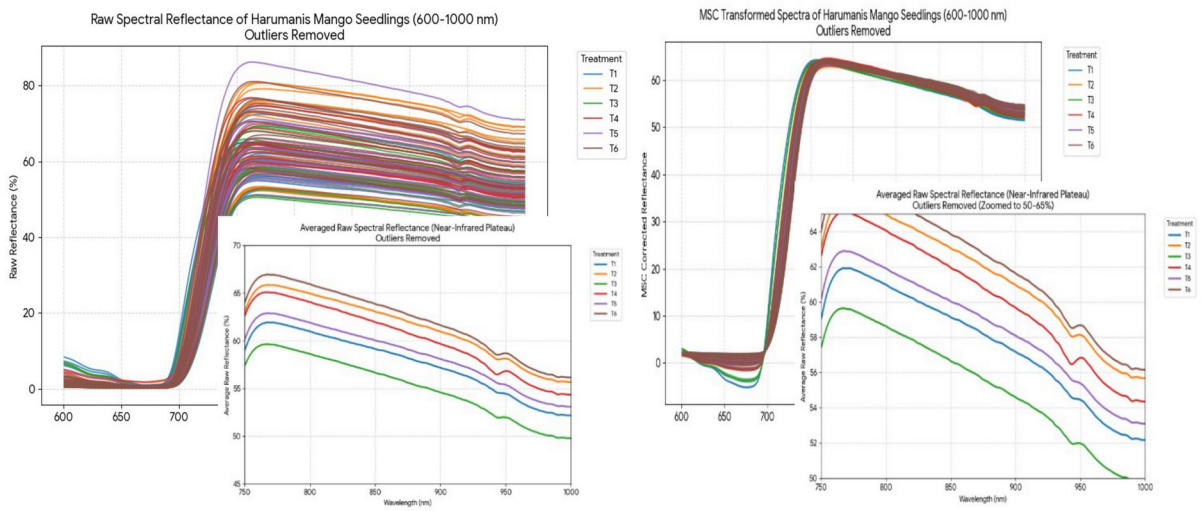

Figure 1. Spectral reflectance of Harumanis mango seedlings: (a) raw spectra, with (c) averaged raw reflectance (zoomed to the NIR plateau) inset; (b) MSC-transformed spectra, with (d) averaged MSC-corrected reflectance (zoomed to 50-65%) inset.

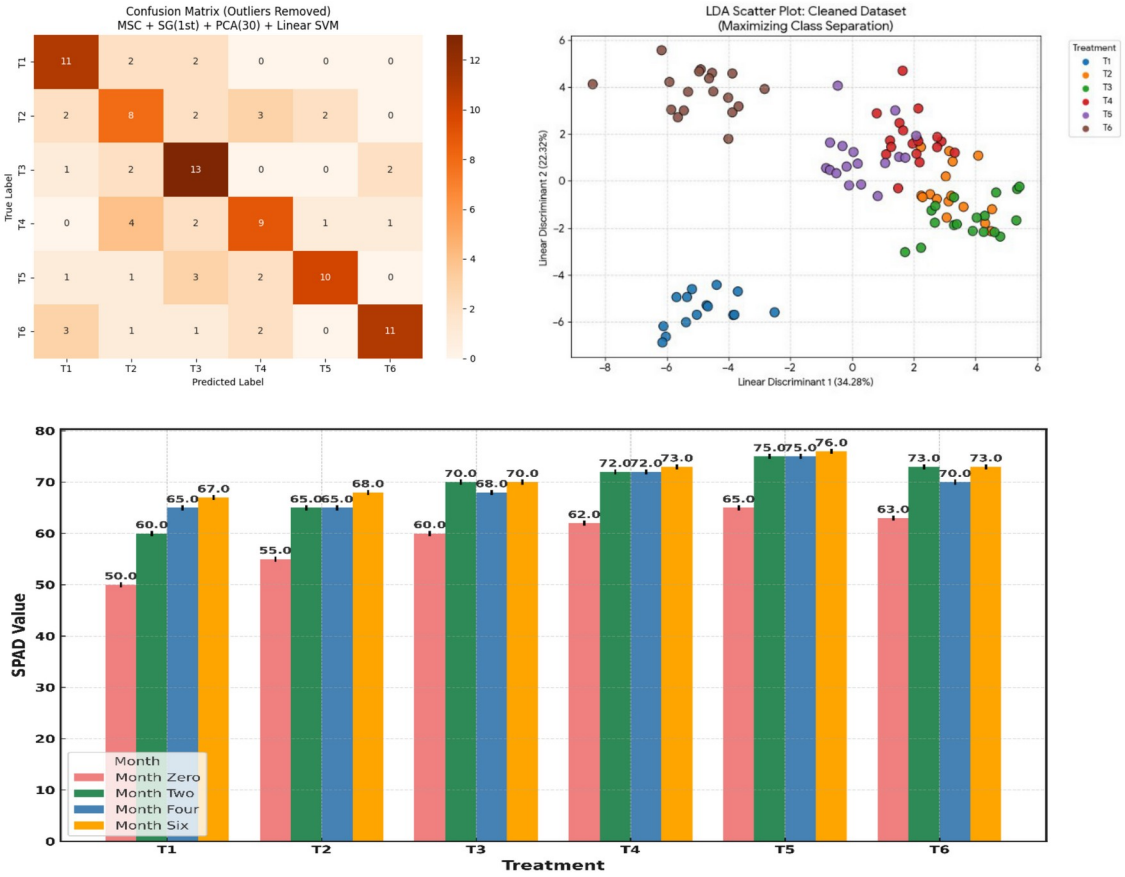

Figure 2. Classification and chlorophyll results: (a) confusion matrix (MSC + SG(1st) + PCA(30) + linear SVM); (b) LDA scatter plot; (c) SPAD chlorophyll values across treatments and time points.

Introduction

This study focuses on Harumanis mango, a premium cultivar that necessitates effective nutrient management to promote healthy growth while minimizing fertilizer usage. The research highlights the role of plant growth-promoting bacteria (PGPB) as environmentally friendly bioinoculants, which are instrumental in enhancing nutrient availability, stimulating root development, and improving nutrient-use efficiency [1]. The methodology employed non-destructive monitoring techniques, specifically near-infrared spectroscopy (NIRS) and SPAD chlorophyll measurements, to facilitate rapid assessment of the mango seedlings' physiological status without causing any damage to the plants [2]. The study aimed to evaluate the impact of PGPB in conjunction with varying levels of NPK fertilizer on Harumanis mango seedlings, utilizing both spectral reflectance and chlorophyll measurements to gather data on the plants' responses. This comprehensive approach underlines the potential for integrating biological methods with traditional fertilizer practices to optimize the growth and sustainability of Harumanis mango.

Methodology

A greenhouse experiment was conducted for six months using Harumanis mango seedlings under six treatments: T1: 0% NPK + 0% PGPB, T2: 0% NPK + PGPB, T3: 25% NPK + PGPB, T4: 50% NPK + PGPB, T5: 75% NPK + PGPB, and T6: 100% NPK + PGPB. Leaf spectral reflectance (600–1000 nm) was measured using a near-infrared spectrometer. Spectra were pre-processed using Multiplicative Scatter Correction (MSC), and outliers were removed before analysis. Treatment discrimination was evaluated using Principal Component Analysis (PCA), Linear Discriminant Analysis (LDA), and a linear Support Vector Machine (SVM). Leaf chlorophyll content was monitored periodically using a SPAD meter throughout the experiment.

Results and Discussion

Raw spectral reflectance demonstrated a distinct vegetation red-edge transition from 700 to 750 nm, followed by a stable NIR plateau from 750 to 1000 nm. Treatments displayed similar spectral patterns, but reflectance magnitude varied. T6 had the highest reflectance on the NIR plateau, followed by T2 and T4, while T3 had the lowest. These variations highlight the impact of nutrient management on canopy optical properties related to leaf structure and physiology [3]. MSC preprocessing minimized spectral variability and maintained treatment differences, enhancing the quality of subsequent multivariate analyses. The confusion matrix indicated strong classification performance across the six treatments, with correct predictions ranging from 8 to 13 per treatment. Misclassifications were primarily noted among intermediate fertilizer treatments due to their similar physiological responses. Additionally, LDA showed distinct clustering of the treatment groups with minimal overlap, affirming that NIR spectral signatures effectively differentiated nutrient management strategies. SPAD values increased from planting to six months across all treatments, indicating enhanced chlorophyll accumulation. The control treatment (T1) had the lowest values, while T5 (75% NPK + PGPB) recorded the highest SPAD value (76), marginally surpassing T6 (73). T5's superiority suggests that combining PGPB with 75% NPK can optimize nutrient availability for chlorophyll accumulation. Additionally, T2 showed better performance than the uninoculated control, highlighting PGPB's benefits even without mineral fertilizer. These results indicate improved nutrient-use efficiency due to bacterial inoculation, pending statistical validation.

Conclusion

Near-infrared spectroscopy and SPAD chlorophyll measurements successfully detected physiological variations in Harumanis mango seedlings treated with different NPK fertilizer and PGPB combinations. Distinct reflectance patterns enabled effective machine-learning classification, while SPAD readings indicated increased chlorophyll content, particularly with a 75% NPK and PGPB combination. This suggests improved physiological performance with reduced fertilizer rates. The study highlights the potential of combining PGPB with lower NPK and recognizes NIR spectroscopy as a quick, non-destructive assessment method, though results are preliminary.

Acknowledgement

The authors gratefully acknowledge the financial support provided by Universiti Sains Malaysia through the Research University Team (RUTeam) Grant Scheme (Grant No. 1001/PBIOLOGI/8580101).

References

[1] Etesami, H. (2024). The dual nature of plant growth-promoting bacteria: Benefits, risks, and pathways to sustainable deployment. Current Research in Microbial Sciences, 9, 100421.

[2] Huang, Q., Yang, M., Ouyang, L., Wang, Z., & Lin, J. (2024). Vis/NIR Spectroscopy and Chemometrics for Non-Destructive Estimation of Chlorophyll Content in Different Plant Leaves. Sensors, 25(6), 1673.

[3] Sullivan, F. B., Hastings, J. H., Ollinger, S. V., Ouimette, A., Richardson, A. D., & Palace, M. (2025). Parsing the Relative Contributions of Leaf and Canopy Traits in Airborne Spectrometer Measurements. Remote Sensing, 18(2), 355.

Infrared-Enhanced Convolutional Neural Networks for Oil Palm Fresh Fruit Bunch Ripeness Classification

Kuan-Huei Ng[1,2], Waldo Udos[1,2], Kok-Sing Lim[1,2,*]

[1]Photonics Research Centre, University of Malaya, Kuala Lumpur 50603, Malaysia

[2]Institute for Advanced Studies, University of Malaya, Kuala Lumpur 50603, Malaysia

***Corresponding author:** kslim@um.edu.my

Keywords: *Oil palm ripeness, IR, CNN, Infrared imaging, Multispectral imaging*

Abstract

Oil palm fresh fruit bunch (FFB) ripeness classification is essential for maximizing oil extraction rates and quality, but conventional manual grading is subjective. While automated RGB-based systems are common, they are often limited by shadows and insufficient color data from dark unripe fruitlets. This study proposes a novel four-channel image representation combining the standard color imaging with infrared (IR) imaging to enhance convolutional neural network (CNN)-based ripeness classification.

Using a common CNN architecture to isolate the effects of input format, 2 models were compared: RGB, RGB + IR. The dataset consisted of 229 paired images captured using a dual-camera setup, with the IR sensitive camera utilizing a long pass (cut-on wavelength: 700 nm) filter to exploit the near-infrared region.

Results showed that the RGB + IR model improved performance by 4%. Class activation heat maps confirmed that the with IR image, the CNN to focus more effectively on biologically relevant fruitlet regions. These findings demonstrate that integrating lightness-separated color components with near-infrared reflectance provides a more robust references set for automated oil palm ripeness classification.

Introduction

Oil palm fresh fruit bunch (FFB) ripeness grading is essential for optimizing oil extraction rate and quality. However, conventional RGB-based convolutional neural networks (CNNs) struggle under inconsistent illumination, shadows, and dark fruitlets [1–3]. To address these limitations without altering the underlying network architecture, this study evaluates four image input representations, including RGB and combined RGB + IR for FFB ripeness classification using a standardized CNN model. While standard RGB imagery captures key color characteristics for ripeness, the near-infrared (NIR) region (700–900 nm) exhibits higher reflectance and greater consistency across lighting conditions [4], serving as a stable spatial reference. Consequently, the proposed four-channel RGB + IR representation merges complementary color and spectral information to provide a more robust feature set for CNN-based classification.

Methodology

This study evaluated the effect of 2 image input representations, RGB and RGB + infrared (IR) on oil palm fresh fruit bunch (FFB) ripeness classification using a single, unified convolutional neural network (CNN) architecture to isolate the impact of data representation. Paired visible and near-infrared (700–800 nm) images of 229 FFB samples across three ripeness stages (ripe, underripe, and unripe) were captured using a parallel dual-camera setup positioned at a fixed 3 m distance under afternoon sunlight. The models shared a baseline CNN structure (Fig 1) consisting of convolutional layers with batch normalization and max-pooling for feature extraction, followed by dense layers with a 0.5 dropout rate and cross-entropy loss optimization. Using a stratified 80:20 train-test holdout split

evaluated over 10 independent random runs, the network was trained with the Adam optimizer and early stopping monitored on validation loss.

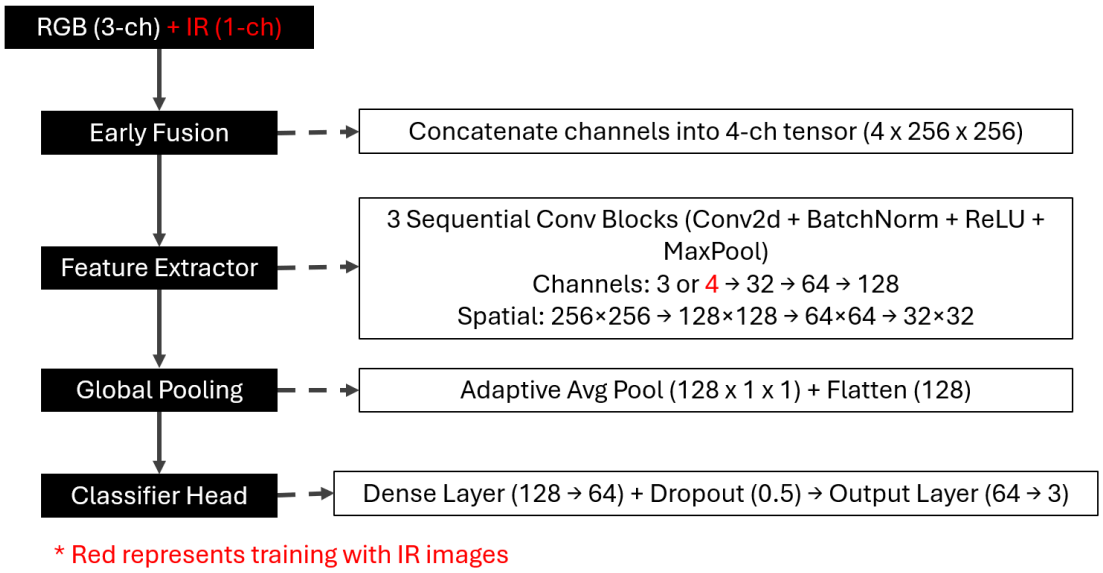

Fig 1. CNN Architecture Diagram (ch = channel).

Results and Discussion

Across 10 independent runs, combining RGB + IR model achieved a weighted average Precision, Recall, and F1-Score of 0.81 ± 0.04, 0.77 ± 0.03, and 0.77 ± 0.04, respectively. In comparison, the RGB-only model achieved 0.77 ± 0.03, 0.77 ± 0.05, and 0.75 ± 0.04. While the multimodal (RGB + IR) model outperformed the RGB-only model in Precision by 4%, no statistically significant improvements were observed for Recall or F1-Score. However, Class Activation Mapping (CAM) (Fig 2) revealed that the RGB + IR model consistently focuses on fruit bunches, whereas the attention of the RGB-only model remains scattered across background elements.

Unripe	Underripe	Ripe
RGB model		
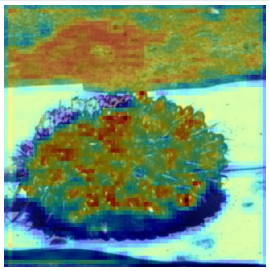	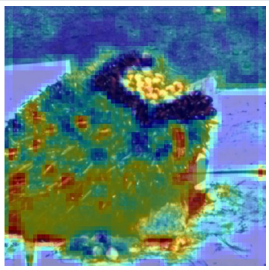	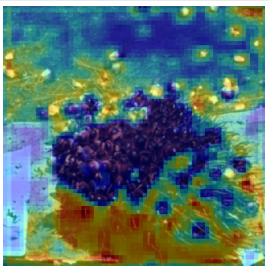
RGB+IR model		
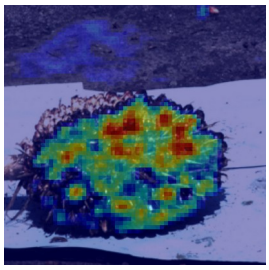	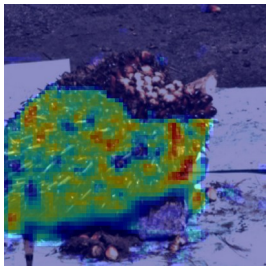	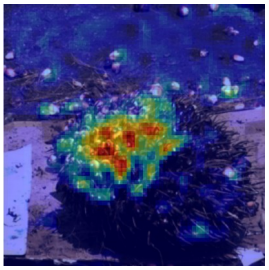

Fig 2. Example of Class activation heat maps of different ripeness class of FFB.

Conclusion

Combining RGB and IR imagery yields a notable 4% gain in Precision over RGB-only models. Crucially, Class Activation Mapping demonstrates that multimodal fusion prevents attention drift, forcing the network to focus on target fruit bunches rather than scattered background noise.

Acknowledgement (Optional)

The authors gratefully acknowledge the financial support provided by Ministry of Higher Education, Malaysia (PRC-2026B).

References

[1] Alfatni, M.S.M.; Shariff, A.R.M.; Shafri, H.Z.M.; Saaed, O.M.B.; Eshanta, O.M. Oil Palm Fruit Bunch Grading System Using Red, Green and Blue Digital Number. J. Appl. Sci. 2008, 8, 1444-1452. https://doi.org/10.3923/jas.2008.1444.1452.

[2] Lai, J.W.; Ramli, H.R.; Ismail, L.I.; Wan Hasan, W.Z. Oil Palm Fresh Fruit Bunch Ripeness Detection Methods: A Systematic Review. Agriculture 2023, 13, 156.

[3] Mendoza, F.; Dejmek, P.; Aguilera, J.M. Calibrated Color Measurements of Agricultural Foods Using Image Analysis. Postharvest Biol. Technol. 2006, 41, 285-295.

[4] Lim, K.-S.; Ahmad Nazri, B.; Rusik, W.R.; Abdul Hamid, A.A.H.; Ooi, C.-W.; Udos, W.; Aris, M.S.; Mohd Yusof, M.Z.; Kulaveerasingam, H.; Chong, W.-Y.; Ismail, M.F.; Ahmad, H. Laser Remote Sensor for Oil Palm Fruit Ripeness Assessment. Proc. SPIE 2024, 12879, 128790I. https://doi.org/10.1117/12.3014258.

OTDR-Based Refractive Index Sensing Using Bare and D-Shaped Fibers

Farra Izzany Tarmizi[1], Wan Maryam Wan Ahmad Kamil[1], Afiq Arif Aminuddin Jafry[1*]

[1]School of Physics, Universiti Sains Malaysia, 11800 USM, Penang, Malaysia

***Corresponding author:** afiqarif@usm.my

Abstract

This research demonstrates the strong potential of optical fiber sensors for monitoring the refractive index (RI) of liquid analytes. While earlier studies primarily emphasized close-range detection, this work advances the field by exploring remote RI measurement through the use of bare fiber (BF) and D-shaped fiber (DSF) probes. The sensing setup adopts a straightforward configuration, consisting of a 2 km fiber cable connected to an optical time-domain reflectometer (OTDR). This setup simplifies operation by using only one end of the fiber, eliminating the need for dual-end source and detector systems. By reducing system complexity, the proposed design not only enhances practicality but also enables RI monitoring in high-risk environments such as chemical processing facilities and polluted ground. The experimental results show that the BF and DSF probes achieved maximum sensitivities of 73.653 dB/RIU and 6.1507 dB/RIU, respectively.

Keywords: *Refractive index sensor, D-shaped fiber, OTDR*

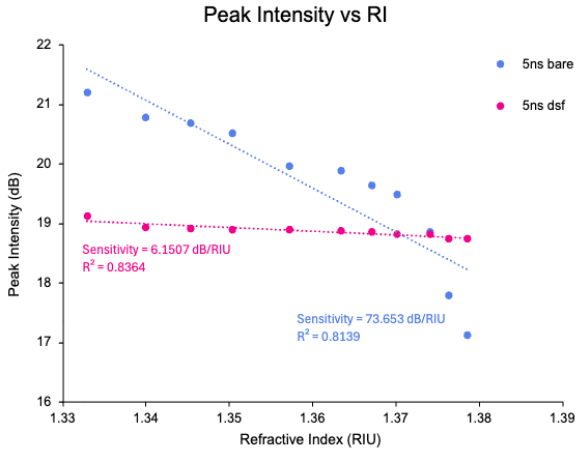

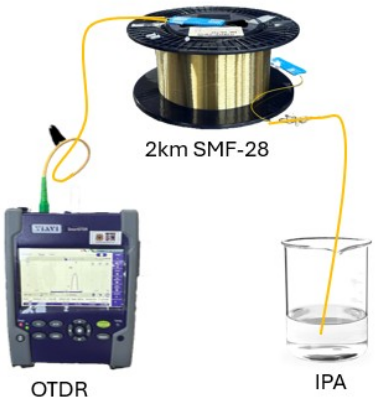

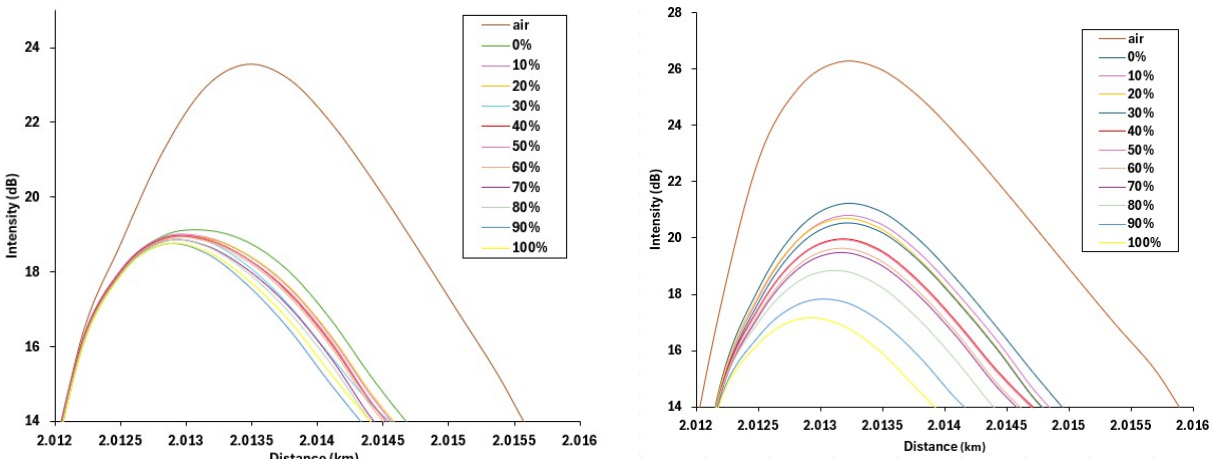

1. Introduction

Refractive index (RI) sensing with optical time-domain reflectometry (OTDR) using SMF-28 (single-mode fiber) has been widely explored due to the fiber's low attenuation and compatibility with conventional optical communication bands around 1310 nm and 1550 nm [1]. SMF-28 functions as a stable sensing medium, and polishing the fiber structure can enhance the evanescent field coupling, allowing stronger interaction with surrounding analytes [2]. Few studies have demonstrated that RI sensing using OTDR with SMF-28 enables precise detection of RI changes in organic liquids, achieving resolutions close to 10^{-4}. This setup is ideal for chemical, biomedical, and environmental applications, particularly where long-distance monitoring and resistance to interference are important [3-4]. In this study, an OTDR-based sensing approach was introduced using a cleaved bare fiber (BF) and D-shaped fiber (DSF) for RI detection of isopropyl alcohol (IPA) solution.

2. Methodology

This study introduces a rapid and efficient polishing technique for SMF-28 fiber, whereby fabrication time can be reduced to under 1 minute through the use of diamond bit instead of sandpaper. A 4 mm diamond polishing bit was used to polish the fiber. An insertion loss of 4 dB marked the end of the polishing process. A 2 km of SMF-28 fiber spool was connected to a Viavi Smart OTDR for RI sensing. The initial probe consisted of a bare fiber that was cleaved at 90°, enabling the reflected light from the OTDR to be directed back into the detection system. The OTDR was configured with fixed parameters at 32 cm resolution, 5 km fiber range, 5 ns acquisition time, and 1550 nm laser source. These parameters were kept constant throughout the experiment to ensure consistency. The probe was first tested with air and subsequently with IPA solutions ranging from 0 to 100% concentration. Next, a DSF probe with 4 dB insertion loss was used. To facilitate the RI detection, the central region of the DSF was cut, enabling the OTDR to observe the peak related to the polished DSF region.

3. Results and Discussion

For the BF probe, the peak intensity decreases as the refractive index increases from 1.33 to 1.39, yielding a sensitivity of 73.653 dB/RIU with a R^2 value of 0.8139. In contrast, the DSF probe exhibits a relatively stable response across the same RI range, with a sensitivity of 6.1507 dB/RIU and R^2 value of 0.8364. These results highlight the sensitivity of the BF probe, while the DSF probe demonstrates a consistent but lower responsiveness. The BF probe obtained an intensity of 26.242 dB in air, then decreased to 21.19 dB when immersed in 0% IPA. As the IPA concentration increases, the peak shifts to lower intensity, having a peak of 17.118 dB in 100% IPA. Correspondingly, the DSF probe obtained an

intensity of 23.553 dB in air, then decreased to 19.116 dB when immersed in 0% IPA. DSF probe obtained an intensity of 18.737 dB in 100% IPA.

4. Conclusion

This study demonstrates two RI sensing probes based on SMF-28 fiber for the detection of IPA solutions. With a maximum sensitivity of 73.653 dB/RIU, the BF probe demonstrates a better responsiveness to RI changes, compared to DSF probe that achieved maximum sensitivity of 6.1507 dB/RIU. The BF probe excels in sensitivity but is less stable, while the DSF probe offers robustness and consistency. Future work should investigate further the DSF probe, as its mechanical stability and durability makes it a promising candidate for real-world application despite lower sensitivity compared to BF.

References

[1] Buerck, J., Roth, S., Kraemer, K., & Mathieu, H. (2003). OTDR fiber-optical chemical sensor system for detection and location of hydrocarbon leakage. Journal of Hazardous Materials, 102(1), 13–28. https://doi.org/10.1016/s0304-3894(03)00199-7

[2] Niu, H., Li, Y., Zhang, Y., Yan, Z., Kuang, J., & An, G. (2024). A High-Precision D-Shaped Fiber Polishing Method and its Sensing Characteristics of Different Polishing Depths. Plasmonics, 20(1), 11–19. https://doi.org/10.1007/s11468-024-02244-1

[3] Rihan, A. N. M., Saharudin, S., Hisham, M. H., Raheem, M. M. K., & Zan, M. S. D. (2025). Assessing the Interplay between Probe Power and Pulse Width in Enhancing Performance of Phase-OTDR Fiber Sensor. Instruments and Experimental Techniques, 68(3), 414–426. https://doi.org/10.1134/s0020441225700502

[4] Yuan, J., Zhao, C., Ye, M., Kang, J., Zhang, Z., & Jin, S. (2013). A Fresnel reflection-based optical fiber sensor system for remote refractive index measurement using an OTDR. Photonic Sensors, 4(1), 48–52. https://doi.org/10.1007/s13320-013-0131-6

X-ray Shielding Performance of Lead-Free Liquid Silicone Rubber Composites Reinforced with Bi_2O_3 and WO_3

Nur Miza Osman[1], Nurul Zahirah Noor Azman[1], Ramzun Maizan Ramli[1*]

[1]School of Physics, Universiti Sains Malaysia, 11800 USM, Penang, Malaysia

***Corresponding author:** ramzun@usm.my

Abstract

Growing concerns about lead toxicity have created demand for safer radiation shielding materials in medical settings. This study evaluated liquid silicone rubber (LSR) composites filled with Bi_2O_3, WO_3, and a Bi_2O_3-WO_3 microparticles at 10, 30, and 50 wt.%, tested at 60 and 100 kVp diagnostic X-ray energies. Shielding performance was assessed using radiation absorption ratio (RAR), linear attenuation coefficient (μ), mass attenuation coefficient (μ/ρ), and half-value layer (HVL). Unfilled LSR showed poor attenuation (RAR of 49.31% and 20.45% at 60 and 100 kVp), while all filled composites reached 98-100% RAR by 30-50 wt.%. Notably, the mixed Bi_2O_3-WO_3 composite achieved the highest RAR and μ/ρ among all samples at only 10 wt.% loading, outperforming either single-filler composite at the same filler content. These findings support LSR/high-Z oxide composites, particularly mixed-filler formulations, as effective, lightweight, lead-free shielding materials for diagnostic radiology applications.

Keywords: *Liquid silicone rubber, Linear attenuation coefficient, Mass attenuation coefficient, Radiation shielding, Microparticles*

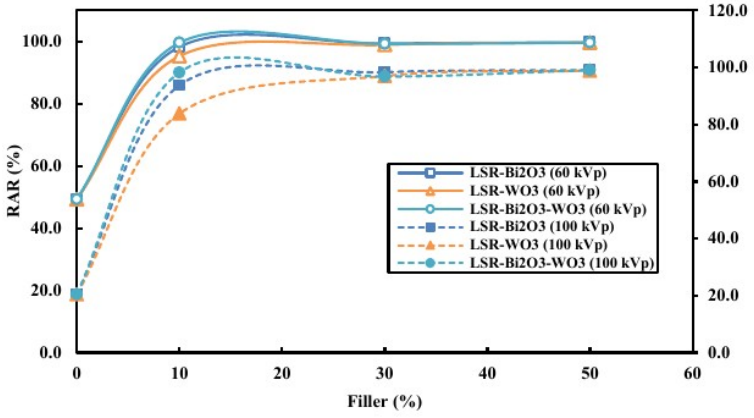

Figure 1. RAR (%) of all fabricated samples at 60 and 100 kVp.

Figure 1. RAR (%) of all fabricated samples at 60 and 100 kVp.

1. Introduction

Growing concerns about lead toxicity have created demand for safer radiation shielding materials in medical settings. Therefore, this study serves as the basic evaluation of the radiation attenuation of heavy metal oxides microparticles (HMOs-MPs) when mixed with polymer material, specifically liquid silicone rubber (LSR). LSR is known for its flexibility, lightweight, inexpensive, high-thermal stability, easy to fabricate, and non-toxic [1], [2]. Moreover, materials with high-density and high atomic number (Z) are preferrable for use as radiation shielding [3], like lead and concrete [4]. Although lead has a high-Z, high density, economical, and easy processability, it is also toxic [5], [6], [7], causes environmental pollution, and absorbs extremely low levels of neutrons. Besides, lead is also heavy to be transported and stored [8]. Given there are substitutes for lead, hence it is crucial to eliminate lead from the global economy by 2035 to protect human health and environment [9]. Therefore, the development

of lead-free, polymer-based radiation shielding materials containing high-density HMO-MPs represents a promising strategy for achieving safe, effective, and environmentally sustainable radiation protection.

2. Methodology

Liquid silicone rubber (LSR; Silocast 588 RTV) was used as the polymer matrix, while bismuth oxide (Bi_2O_3) and tungsten oxide (WO_3) microparticles (Sigma-Aldrich, USA) served as the radiation-shielding fillers due to their high density and photon attenuation capability. 10 LSR composites with varying filler compositions of 10, 30, and 50 wt.% were fabricated by mixing the fillers with the LSR matrix, followed by the addition of 3 wt.% hardener. The mixtures were cast into 0.5 cm-thick, 3.3 cm-diameter moulds, degassed using a dental vibrator, and cured at room temperature for 24 h. The morphology and elemental composition of the raw materials were characterized using field-emission scanning electron microscopy (FESEM) coupled with energy-dispersive X-ray spectroscopy (EDX). Radiation attenuation performance was evaluated using a diagnostic X-ray system operated at 60 and 100 kVp, with a fixed 10 mAs, and a source-to-surface distance of 100 cm. The incident and transmitted X-ray intensities were measured using a RaySafe X2 detector, and the shielding performance was assessed in terms of radiation absorption ratio (RAR; %), linear attenuation coefficient (μ; cm-1), mass attenuation coefficient (μ/ρ; cm2/g), and half-value layer (HVL; cm).

3. Results and Discussion

Across all three composite series, incorporating a high-Z filler into LSR produced a sharp improvement in shielding performance over the unfilled matrix (RAR of 49.31% and 20.45% at 60 and 100 kVp, respectively), with RAR rising to 98-100% by 30-50 wt.% loading regardless of filler type. The mixed Bi_2O_3-WO_3 composite outperformed both single-filler series at the lowest loading (10 wt.%), reaching RAR of 99.62% (60 kVp) and 98.25% (100 kVp) compared to that of individual Bi2O3 and WO3 fillers, and correspondingly showed the highest μ/ρ among all samples (5.85 and 4.24 cm^2/g at 60 and 100 kVp), suggesting a compositional advantage from combining two high-Z oxides rather than a purely density-driven effect. These results indicate that shielding gains are largely realized at moderate filler loading, and that filler combination not just filler quantity can meaningfully improve attenuation efficiency per unit mass.

4. Conclusion

LSR composites filled with Bi_2O_3, WO_3, and their combination all showed substantial improvement in X-ray attenuation over unfilled LSR, with performance saturating near 30-50 wt.% regardless of filler type. The mixed-filler composite achieved the best shielding efficiency at the lowest filler loading tested, indicating that combining two high-Z fillers can improve attenuation per unit mass more effectively than a single filler alone. These results suggest that mixed high-Z oxide loading in LSR is a promising, lightweight, lead-free approach for diagnostic radiology shielding.

References

[1] M. T. Alresheedi et al., "Assessment of Silicone Rubber/Lead Oxide Composites Enriched with Bi2O3, WO3, BaO, and SnO2 Nanoparticles for Radiation Shielding Applications," Polymers (Basel)., vol. 15, no. 9, May 2023, doi: 10.3390/polym15092160.

[2] W. Abdullah, R. M. Ramli, T. H. Khazaalah, N. Z. N. Azman, T. M. Nawafleh, and F. Salem, "Enhancing X-ray radiation protection with novel liquid silicone rubber composites: A promising alternative to lead aprons," Nuclear Engineering and Technology, vol. 56, no. 9, pp. 3608–3615, Sep. 2024, doi: 10.1016/j.net.2024.04.012.

[3] C. E. Okafor, U. C. Okonkwo, and I. P. Okokpujie, "Trends in reinforced composite design for ionizing radiation shielding applications: a review," Jul. 01, 2021, Springer. doi: 10.1007/s10853-021-06037-3.

[4] N. M. Osman, S. Mohamad Tajudin, A. Hanim Aminordin Sabri, A. Faddilah Mohd Noor, and M. Zahri Abdul Aziz, "Evaluation of scattering effects for radiation shielding or filter materials by using Monte Carlo simulation," IOP Conf. Ser. Mater. Sci. Eng., vol. 1231, no. 1, p. 012007, Feb. 2022, doi: 10.1088/1757-899x/1231/1/012007.

[5] K. V. Sathish et al., "X-ray/gamma radiation shielding properties of Aluminium-Barium-Zinc Oxide nanoparticles synthesized via low temperature solution combustion method," Nuclear Engineering and Technology, vol. 55, no. 5, pp. 1519–1526, May 2023, doi: 10.1016/j.net.2023.02.001.

[6] W. Abdullah, R. M. Ramli, T. H. Khazaalah, N. Z. N. Azman, T. M. Nawafleh, and F. Salem, "Enhancing X-ray radiation protection with novel liquid silicone rubber composites: A promising alternative to lead aprons," Nuclear Engineering and Technology, vol. 56, no. 9, pp. 3608–3615, Sep. 2024, doi: 10.1016/j.net.2024.04.012.

[7] B. Buyuk, "Cs-137 Gamma Ray Attenuation Properties of Flexible Silicone Rubber Materials," European Journal of Science and Technology, pp. 28–35, Mar. 2019, doi: 10.31590/ejosat.501475.

[8] M. I. Sayyed, H. O. Tekin, O. Kilicoglu, O. Agar, and M. H. M. Zaid, "Shielding features of concrete types containing sepiolite mineral: Comprehensive study on experimental, XCOM and MCNPX results," Results Phys., vol. 11, pp. 40–45, Dec. 2018, doi: 10.1016/j.rinp.2018.08.029.

[9] S. P. Luby et al., "Removing lead from the global economy," 2024. [Online]. Available: www.thelancet.com/

Chemometric-Assisted Raman Spectroscopy for Geographical and Varietal Discrimination of Asian Rice

Amir Murtadha Mohamad Yussof[1*], Fazida Hanim Hashim[1]

[1]Department of Electrical, Electronic and Systems Engineering, Faculty of Engineering and Built Environment, Universiti Kebangsaan Malaysia (UKM), 43600 UKM Bangi, Selangor, Malaysia

***Corresponding author:** Amir Murtadha Mohamad Yussof — P154145@siswa.ukm.edu.my, fazida@ukm.edu.my

Abstract

This study establishes a rapid chemometric framework to authenticate premium Asian rice cultivars and geographical origins using dispersive Raman spectroscopy on crushed grains. Using spectral data across multiple commercial provenances and variety classes, the research successfully differentiated grain origins and types using a combined input of principal components and specific spectral features in supervised LDA models, achieving high classification accuracy for reliable provenance and varietal verification.

Keywords: *Authentication, Chemometrics, PCA-LDA, Raman Spectroscopy, Crushed-grain, Rice*

Introduction

Rice (Oryza sativa L.) is a highly valued global staple [1]. The economic prominence of premium cultivars, such as Basmati, makes the supply chain vulnerable to fraudulent dilution with cheaper, mixed-origin grains [2]. Traditional molecular and physicochemical authentication assays are often destructive, labor-intensive, and impractical for routine bulk screening [3]. Raman spectroscopy has emerged as a state-of-the-art alternative, capable of mapping structural carbohydrate modes such as pyranose ring skeletal modes (~480 cm^{-1}) and amorphous aliphatic CH2 bending (~1380 cm^{-1}) without complex sample preparation [4]. However, micro-heterogeneity in biological samples can obscure subtle spectral variations [5]. This study aims to develop an optimized chemometric pipeline combining 785 nm Raman spectroscopy with PCA-LDA modeling to accurately discriminate commercial Asian rice classes based on both their geographical provenances and varietal biochemical fingerprints.

Methodology

Four commercial rice cultivars (Pakistan Basmati, India Basmati, Thailand Jasmine, and Malaysia local white) were selected for this pilot study (n = 3 per sample, N=12). Grains were mechanically pulverized into a homogeneous powder using a stone mortar inside a replaceable parchment barrier for 1 to 2 minutes to expose the internal starch matrix while preventing cross-contamination. The resulting powder was stored in airtight polyethylene bags at room temperature to equilibrate moisture content and minimize water-band interference. Raman spectra were then acquired using a DXR Raman Microscope equipped with a 784 nm near-infrared laser (785 nm filter), a 400 lines/mm grating, a slit aperture, and a 21.0 mW laser power. Measurements were recorded with an exposure time of 0.50 seconds and 3 co-additions at multiple spatial locations to account for micro-heterogeneity. Signal preprocessing was executed in Orange Data Mining, involving spectral truncation (350–1750 cm^{-1}), Rubberband baseline estimation to subtract fluorescence, a Savitzky-Golay smoothing filter (second-order polynomial, 11-point window) to reduce noise, and L2-norm Vector Normalization to correct for powder-packing variations. For univariate evaluation, One-Way ANOVA was conducted in IBM SPSS using structural peak intensities (such as integrated peaks around ~480, ~840, and ~1380 cm^{-1}) to assess crystallinity variations. Furthermore, Principal Component Analysis (PCA) was performed in Orange Data Mining to extract the leading three orthogonal components (PC1, PC2, and PC3) capturing 77.2% of cumulative variance. Finally, supervised Linear Discriminant Analysis (LDA) models configured for geographical provenance and consolidated commercial varieties were executed

utilizing a combined input matrix incorporating the principal components (PC1, PC2, and PC3) alongside specific spectral variables, integrated peak intensities, and ratiometric data and evaluated using Leave-One-Out Cross-Validation (LOOCV).

Results and Discussion

Preprocessed Raman spectra revealed distinct starch macromolecular vibrational modes across all cultivars. Unsupervised PCA successfully condensed the high-dimensional data, capturing a cumulative explained variance of 77.2%. Univariate quantitative evaluation of the structural crystallinity biomarker (I480/I1380) yielded mean values ranging from 0.5904 to 0.8115. One-Way ANOVA indicated non-significant pairwise differences ($p>0.05$), highlighting the limitation of relying on isolated univariate band ratios for heterogeneous powder samples and justifying multivariate modeling. To overcome univariate overlaps, the supervised PCA-LDA classification models utilized the three retained PCs. The models successfully mapped the distinct multidimensional signatures, achieving a 100.0% overall original training accuracy with distinct spatial group centroids and perfect class-specific separation for both the four regional geographical provenances and the three consolidated commercial variety classes (Basmati, Jasmine, and Local White). Applying rigorous LOOCV on the compact pilot dataset (n=3 to 6 per group) yielded cross-validated variations consistent with compact sample constraints. Spectroscopically, this fold-collapse is attributed to the inherent structural homology of the Oryza sativa L. starch matrices, combined with micro-structural surface variations from commercial milling and polishing. However, the 100.0% original training accuracy confirms that unique, class-specific chemical signatures are genuinely present within the spectra, demonstrating baseline separability.

Geographical Discrimination Plot

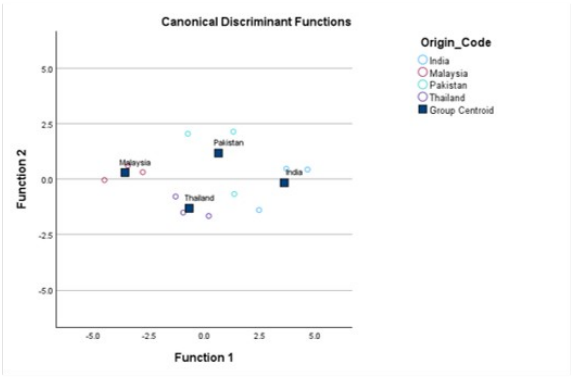

Varietal Discrimination Plot

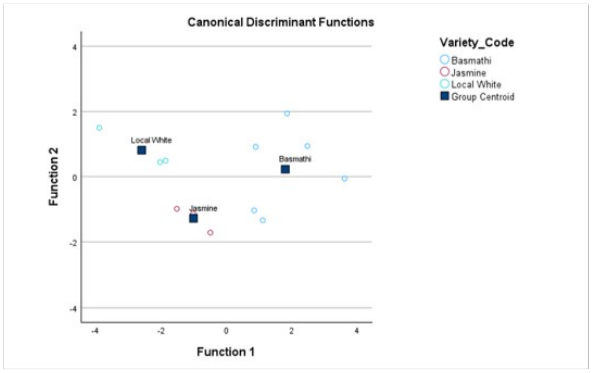

Geographical Confusion Matrix

			Predicted Group Membership				
		Origin_Code	India	Malaysia	Pakistan	Thailand	Total
Original	Count	India	3	0	0	0	3
		Malaysia	0	3	0	0	3
		Pakistan	0	0	3	0	3
		Thailand	0	0	0	3	3
	%	India	100.0	.0	.0	.0	100.0
		Malaysia	.0	100.0	.0	.0	100.0
		Pakistan	.0	.0	100.0	.0	100.0
		Thailand	.0	.0	.0	100.0	100.0

Varietal Confusion Matrix

			Predicted Group Membership			
		Variety_Code	Basmathi	Jasmine	Local White	Total
Original	Count	Basmathi	6	0	0	6
		Jasmine	0	3	0	3
		Local White	0	0	3	3
	%	Basmathi	100.0	.0	.0	100.0
		Jasmine	.0	100.0	.0	100.0
		Local White	.0	.0	100.0	100.0

Conclusion

This exploratory pilot study successfully demonstrates the feasibility of utilizing 785 nm Raman spectroscopy, paired with parchment-protected pulverization, for the rapid authentication of commercial Asian rice cultivars. By compressing spectral variance via PCA (77.2% retention), the supervised PCA-LDA models achieved 100.0% original training accuracy for both geographical provenance and varietal class differentiation, effectively overcoming the limitations of univariate crystallinity assessments. These findings highlight substantial practical utility for rapid authenticity screening. Future work will focus on expanding the biological dataset to larger commercial batches and blind adulteration series to overcome cross-validation sensitivities and establish robust out-of-sample predictive generalization.

Acknowledgement

The authors gratefully acknowledge the financial and technical support provided by Geran Universiti Penyelidikan (GUP-2025-041) and UKM-YSD Chair for Sustainability, Faculty of Engineering and Built Environment, Universiti Kebangsaan Malaysia (UKM) which facilitated the successful completion of this research.

References

[1] U. Uawisetwathana and N. Karoonuthaisiri, "Metabolomics for rice quality and traceability: feasibility and future aspects," Current Opinion in Food Science, vol. 28, pp. 58–66, 2019, doi: https://doi.org/10.1016/j.cofs.2019.08.008.

[2] M. Pérez-Rodríguez, M. Villarreal-Marines, A. Mendoza, J. A. Gomes Neto, and E. C. Ferreira, "Adulteration Level Prediction and Screening in Bulk Rice Using Laser-Induced Breakdown Spectroscopy Coupled with Nonlinear Modeling," ACS Food Science & Technology, vol. 5, no. 11, pp. 4372–4383, 2025, doi: https://doi.org/10.1021/acsfoodscitech.5c00869.

[3] Z. Liu, J. Li, Z. Bi, Q. Shen, K. Zhao, and J. Lou, "RFDNet: A Feature-Decouple Dual-Stream Network for Rice Traceability Using Handheld Low-Intensity Raman Spectroscopy," Preprint / Under Review, pp. 1–25, 2025.

[4] J. Guo, S. Jiang, B. Lu, W. Zhang, Y. Zhang, X. Hu, W. Yang, H. Feng, and L. Xu, "Exploring the potential of microscopic hyperspectral, Raman, and LIBS for nondestructive quality assessment of diverse rice samples," Plant Methods, vol. 21, no. 1, p. 25, 2025, doi: https://doi.org/10.1186/s13007-025-01345-0.

[5] M. Sha, D. Zhang, Z. Zhang, J. Wei, Y. Chen, M. Wang, and J. Liu, "Improving Raman spectroscopic identification of rice varieties by feature extraction," Journal of Raman Spectroscopy, vol. 51, no. 5, pp. 702–710, 2020, doi: https://doi.org/10.1002/jrs.5828.

Partners, Sponsors and Exhibitors

With thanks to the organizations whose support made MNIRSM 2026 possible.

Main Sponsor

OPTOSKY PHOTONICS INC.

Optosky Photonics Inc.

Main Sponsor, MNIRSM 2026

China

Sponsor Profile

SPONSOR PROFILE

Optosky Photonics Inc. is the Main Sponsor of MNIRSM 2026, generously providing the Conference Dinner at Pen Mutiara and lending laboratory equipment for the Day 2 demonstration session. Headquartered in China, Optosky is a National Key "Specialized and Sophisticated" Little Giant Enterprise operating five national high-tech enterprises and six R&D centers, and holds more than 100 invention patents and over 300 intellectual property rights. The company has led the formulation of 25 national standards in spectroscopy, including China's national standard for Raman spectrometers and the industry standard for visible and near-infrared field spectrometers.

Equipment Support

EQUIPMENT PROVIDED

For the Day 2 laboratory tour and equipment demonstration, Optosky Photonics Inc. lent instruments spanning its full product range. Fiber Spectrometers: ATP8130, ATP8000, ATP8200 and ATP8600 Series (deep-cooling short-wave and near-infrared spectrometers). NIR Spectrometers: IR2000Pro full-spectrum analyzer, IR2300 Grain Analyzer, IR2500 Fourier Transform NIR Spectrometer and ATP8900 Portable Fourier Infrared Spectrometer. Hyperspectral Imagers: ATH9010 UAV-mounted hyperspectral imaging system, ATHL9010 Series (hyperspectral + LiDAR integrated system), ATH1010R short-wave infrared hyperspectral imager and ATH2000 Series handheld high-resolution hyperspectral imager. Field Spectroradiometers: ATP9110 ultra-wide-band hyperspectral field spectrometer, ATP9100 handheld field spectrometer, IR2200 handheld near-infrared field spectrum analyzer and ATP9101W ultra-compact wide-spectrum field spectrometer.

Representative equipment supplied by Optosky Photonics Inc.

ATP8130 — SWIR Fiber Optic Spectrometer

IR2000Pro — Full-Spectrum NIR Analyzer

ATH9010 — UAV-Mounted Hyperspectral Imaging System

ATP9110 — Ultra-Wide Band Hyperspectral Field Spectrometer

Supporting Organization

PENANG CONVENTION & EXHIBITION BUREAU (PCEB)

Penang Convention & Exhibition Bureau

Supporting Organization, MNIRSM 2026

Penang, Malaysia

About PCEB

SUPPORTING ORGANIZATION

Penang Convention & Exhibition Bureau (PCEB) is the official body established by the Penang state government to promote Penang as a destination for meetings, incentives, conferences and exhibitions (MICE), and to support organizers in bringing events of this kind to the state. MNIRSM 2026 gratefully acknowledges PCEB's support in helping bring this inaugural meeting to Penang.

Partner

BRUKER MALAYSIA SDN. BHD.

Bruker Malaysia Sdn. Bhd.

Partner, MNIRSM 2026

Malaysia

About Bruker Malaysia

PARTNER PROFILE

Bruker Malaysia Sdn. Bhd. is a Partner of MNIRSM 2026, leading the Workshop on FTIR — "FTIR Application in Chemistry and Academic" — on Day 2 (15 September 2026), 14:00-15:00, in the Conference Room. Bruker is a global leader in scientific instrumentation, supplying FTIR, Raman and related analytical spectroscopy systems to research and industry worldwide. MNIRSM 2026 gratefully acknowledges Bruker's support in sharing this workshop with delegates.

Partner

SHIMADZU MALAYSIA SDN. BHD.

Shimadzu Malaysia Sdn. Bhd.

Partner, MNIRSM 2026

Malaysia

About Shimadzu Malaysia

PARTNER PROFILE

Shimadzu Malaysia Sdn. Bhd. is a Partner of MNIRSM 2026, leading the Workshop on UV-Vis-NIR — "UV-Vis-NIR Spectroscopy: Enabling Innovation in Science and Photonics Research" — on Day 2 (15 September 2026), 15:00-16:00, in the Conference Room. Shimadzu is a global manufacturer of analytical and measuring instruments, including UV-Vis, NIR and mass spectrometry systems used widely across science and industry. MNIRSM 2026 gratefully acknowledges Shimadzu's support in sharing this workshop with delegates.

Partner

CARL ZEISS AG

Carl Zeiss AG

Partner, MNIRSM 2026

Germany

About ZEISS

PARTNER PROFILE

Carl Zeiss AG (ZEISS) is a Partner of MNIRSM 2026, recognized on the conference's official partner listing. ZEISS is a global manufacturer of optical and optoelectronic instruments, with a product range spanning microscopy, spectroscopy and imaging systems, medical technology, semiconductor manufacturing equipment and industrial metrology, and a heritage spanning more than 175 years. MNIRSM 2026 gratefully acknowledges ZEISS's partnership in supporting this inaugural meeting.

Thank You

MNIRSM 2026 gratefully acknowledges everyone who made this inaugural meeting possible.

MAIN SPONSOR

OPTOSKY Spectroscopy Solutions

PARTNERS

OSM Optical Society of Malaysia

Asian NIR Consortium

SHIMADZU Excellence in Science

BRUKER

ZEISS

SUPPORTED BY

PENANG 2030

PG

penang convention & exhibition bureau

PENANG Inspiring Meetings

ORGANIZED BY

USM UNIVERSITI SAINS MALAYSIA

APEX

SCHOOL OF PHYSICS UNIVERSITI SAINS MALAYSIA

mnirsm.usmphysics.org